University of Alberta

Steam Assisted Gravity Drainage (SAGD): Influence of Geomechanical Processes on Absolute Permeability

By

Kais Ben Abdallah

A thesis submitted to the Faculty of Graduate Studies and Research

In partial fulfillment of the requirements for the degree of

Master of Science

in

Petroleum Engineering

Department of Civil and Environmental Engineering

Fall 2013

Edmonton, Alberta

Abstract

Alberta is recognized by its vast oil sands reserves. The applications of established thermal processes, such as SAGD, are commonly required to achieve economic hydrocarbon recovery. Steam injection causes pore pressure and temperature changes that influence the reservoir geomechanical properties with a related impact on flow properties such as absolute permeability.

Drained triaxial compression tests were conducted to investigate the impact of SAGD on the petrophysical properties of unconsolidated sands at low stress conditions. The testing program included stress-strain and permeability tests run under two main stress paths: isotropic compression and triaxial compression. Isotropic compression produced small magnitude changes in absolute permeability while triaxial compression test resulted in a substantial increase of permeability. In general, lower permeability gain was reported at higher level of effective confining pressure. An empirical correlation linking absolute permeability to effective confining stress and volumetric strain change was developed for use in reservoir geomechanical simulations.

Acknowledgement

I would like to thank my supervisor Dr. R. J. Chalaturnyk as well as co-supervisor Dr. J. Leung for their guidance and support towards the achievement of this research work.

In addition, I want to show my deepest respect to my father Amor and my mother Naima as well as my sisters; Hajer, Houda, Faten, and Loubna who have always encouraged me to achieve my goals and objectives.

I express my greatest gratitude to my friend Mohammed Hamoud for his precious illustrations and encouragement to accomplish my Masters.

Finally, I wish to acknowledge and show appreciation to the geomechanics laboratory group members; Steve, Gilbert, Rishi, Saurav, and Hope for their technical assistance.

Table of Contents

List of Figures

List of Tables

1 Introduction

By virtue of its significant reserves, heavy oil/bitumen reserves have gradually climbed from a marginal to a dominant hydrocarbon resource to supply North American energy demands.

According to International Energy Agency (IEA) studies, there are six trillion barrels in place of heavy oil, bitumen and extra-heavy oil worldwide. Among them, two and half trillion barrels of heavy oil are located in the Western Canada deposits. This important volume of crude places the Canadian proven reserves as the second most important oil deposit in the world just behind those of Saudi Arabia (Figure 1.1). However, due to the geological constraints and specific properties of the crude, high viscosity and density (low API gravity), only three hundred billion out of two and half trillion barrels of Canadian bitumen/heavy oil reserves have been proven to be recoverable with today's technology and economic circumstances (Khan 2009).

The largest portion of Canadian hydrocarbon reserves, approximately of three hundred billion barrels, occurs in the province of Alberta. The Albertan heavy oil reserves are found in the Athabasca, Peace River and Cold Lake regions. The Athabasca oil sand deposits are the largest Cretaceous-aged oil sand in Canada and probably the largest single accumulated deposit in the world. Located around the city of Fort McMurray, this huge reserve covers an area of 46,000 square kilometers that contains approximately 176 billion barrels of proven hydrocarbon reserve consisting of 174 billion barrels of heavy viscous bitumen and 1.6 billion barrels of crude oil (Government of Alberta 2008). Most of the heavy oil deposits, including the Athabasca deposit, exist in unconsolidated shallow sandstone formations wherein the porosity is typically higher than 30% and the absolute permeability usually ranges between 500 md and 15,000 md (Khan 2009).

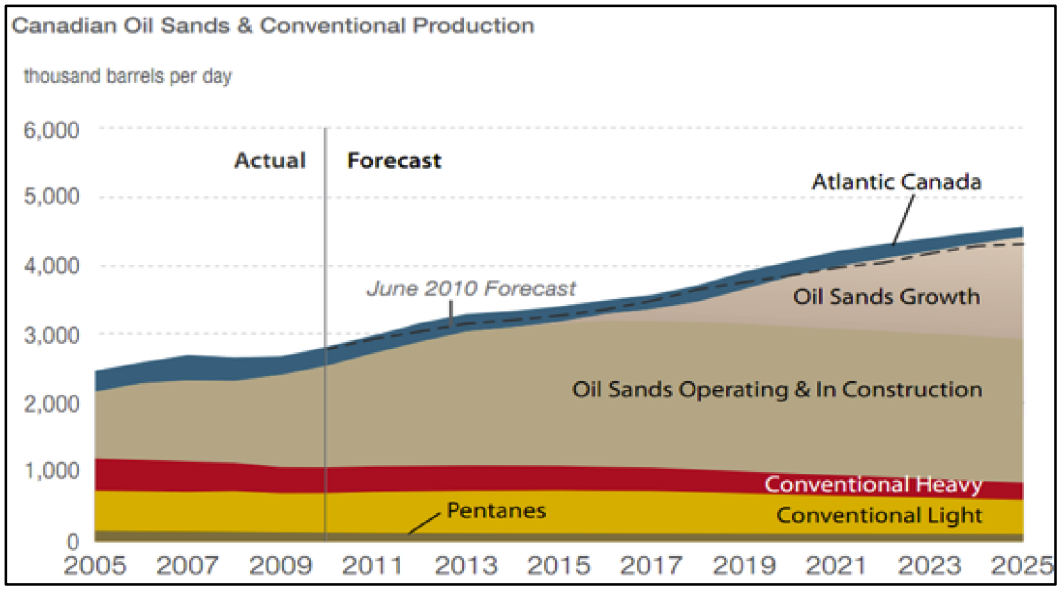

Figure 1.1 Canadian oil sands and conventional production (CAPP, 2012).

Although an economically significant volume of heavy oil can be and is being produced using surface mining techniques, the vast majority of the Albertan deposits are buried too deeply to be exploited by conventional open-pit mining methods. The applications of established thermal processes (e.g. SAGD and CSS) are commonly required to achieve economic hydrocarbon recovery from oil sand reservoirs. Nevertheless, the high viscosity and density of the oil make these processes far more expensive and technological demanding than the conventional recovery techniques.

Similar to other thermal process, Steam Assisted Gravity Drainage (SAGD) improves the oil mobility by steam flooding the oil sand formation. The steam raises the bitumen temperature thus reducing the oil viscosity, making the recovery of heavy oil technically feasible. An important part of SAGD success is attributed to the improvement of petrophysical properties associated to the steam stimulation. Actually, steam injection imparts important perturbations in the initial stresses state of oil reservoir by increasing its pore pressure and temperature. In turn, theses alterations induce variations in the geomechanical

properties of the heavy oil bearing formation and in particular its absolute permeability (i.e. pore volume, effective stress, volumetric deformation, porosity etc.). Accordingly, the associated increases in permeability and water transmissibility accelerate the steam chamber growth, promoting further increase in the oil producibility of the reservoir. Quantifying the absolute permeability enhancement caused by the SAGD's geomechanical effects was the primary focus in this research.

1.1 Oil Sand: Definition and Characteristics

The crude bitumen contained in the Canadian oil sand is usually defined as a highly viscous form of petroleum that has low or no mobility to flow without being heated or diluted with lighter hydrocarbons. From a geological perspective, Albertan bitumen/heavy oils are immature oils that originated in the Cretaceous aged shale (source rock) formations and flowed up-dip, due to tectonics forces, to upper-Cretaceous traps. Over time, the migrated light crude was gradually transformed by washing water and bacterial action into highly viscous bitumen with an average viscosity exceeding 10,000 Centipoises (Meyer 1990). Biodegradation, water washing and sulphate reducing bacterial action were the main factors behind the specific nature of this oil.

Natural bitumen and extra-heavy oil differ in the degree by which they have been degraded from the original conventional oils by bacteria and erosion (Figure 1.2). The most generally accepted definition of bitumen sand is that provided by the UNITAR, which is defining bitumen sand as sand containing naturally occurring bitumen that has a gas free viscosity at reservoir condition higher than 10,000 centipoises. While according to the World Energy Council (WEC), extra-heavy oil is described as a hydrocarbon that has a gravity of less than 10° API and a reservoir viscosity of no more than 10,000 centipoises. According to UNITAR definition, the most important bitumen and extra-heavy oil deposits in the world are located in Alberta and the former Soviet Union.

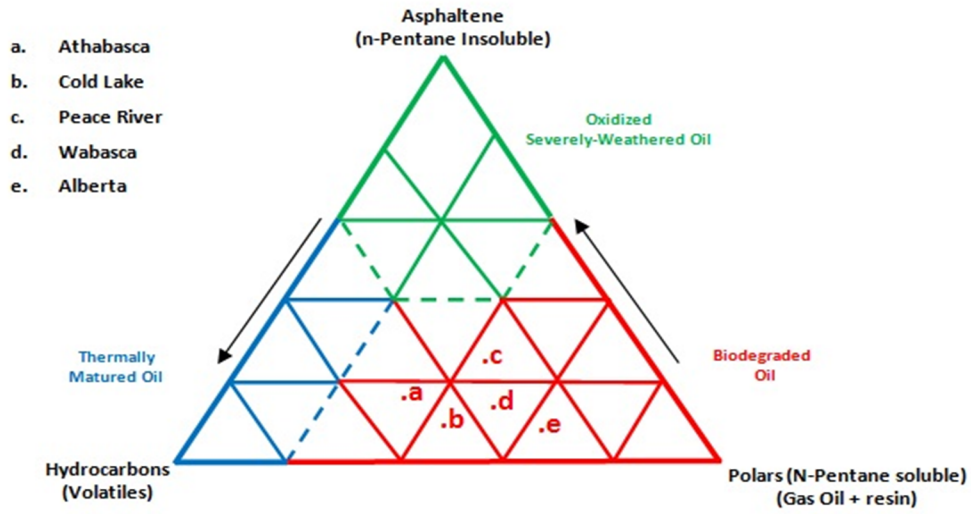

Figure 1.2 Definition of heavy oil sands by ternary classification (Redford, 2011).

1.2 Steam Assisted Gravity Drainage (SAGD)

1.2.1 Steam Assisted Gravity Drainage (SAGD): Recovery Technique Description

The Steam Assisted Gravity Drainage (SAGD) concept was originally conceived 30 years ago by Dr. Roger Butler, an engineer working for the Imperial Oil Company. SAGD was initially field tested with success in 1975 at the Underground Test Facility (UTF) near the Fort McMurray, Alberta (Butler 1991). Since then, this revolutionary technique has been successful in reforming the heavy oil economics in Canada, by achieving a considerable improvement in the oil recovery factors. This encouraging amount of recovery has boosted heavy oil exploration in all heavy oil/bitumen deposits in Alberta.

The SAGD process consists of drilling two parallel horizontal oil wells in the formation, with one about 4 to 6 meters above the other. The upper well injects steam, possibly mixed with solvents, and the lower one collects the heated bitumen that flows out of the formation, along with any water from the condensation of injected steam. The basis of the process is that the injected

steam forms a "steam chamber" that grows vertically and horizontally in the formation. The heat from the steam reduces the viscosity of the heavy oil or bitumen, which allows it to flow, by gravity, into the lower wellbore (Figure 1.3 and 1.4). The steam and gases rise because of their low density compared to the heavy oil or bitumen, ensuring that steam is not produced at the lower production well. The gases released, which include methane, carbon dioxide, and usually some hydrogen sulfide, tend to rise in the steam chamber, filling the void space left by the oil and, to a certain extent, forming an insulating heat blanket above the steam. Driven by gravity, oil and water flow by a counter-current into the lower well bore (i.e. gravity driven drainage) and subsequently recovered to the surface through pumps (Khan 2009).

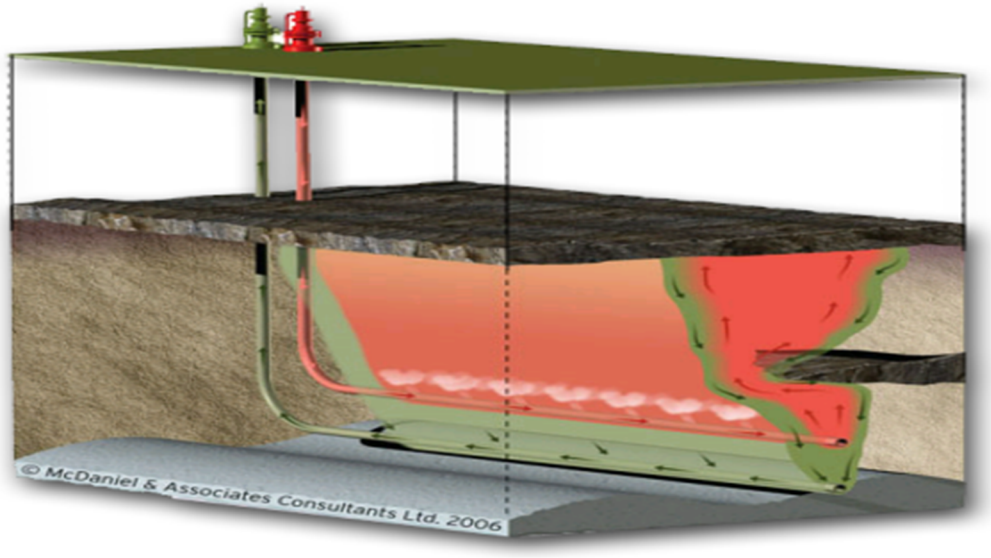

Figure 1.3 Schematic view of SAGD process (McDaniel and Associates Ltd., 2006)

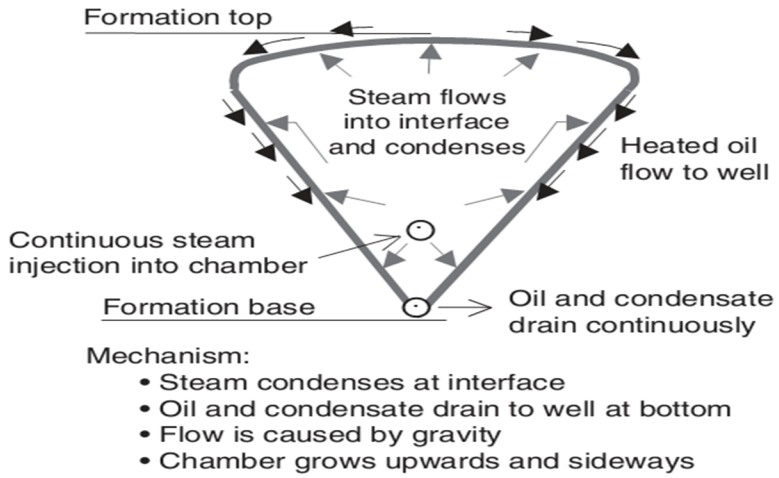

Figure 1.4 Idealized two horizontal well concept for SAGD (Redford, 2011).

The injection of steam into a heavy oil or oil sand/bitumen reservoir often creates problems due to extremely unfavorable mobility ratio. Hence, prior to the start of the SAGD process, preheating and subsequent blow-down periods are necessary. During the pre-heating period, high-pressure steam is circulated down both the injection and production wells thus heating the bitumen by conduction in the reservoir. As the bitumen's temperature is increased, its viscosity decreases. Once thermal communication is established between the two wells, the bitumen becomes mobile within the vicinity of the wells. The conventional SAGD process follows the blow-down period where both injection and production wells are operated at constant pressure. Steam trap production is usually used as an operational control to reduce or prevent steam withdrawal from the reservoir (Qing Chen 2009). Steam trap production is achieved by managing oil production rates such that an oil level is maintained just above the production well to prevent the influx of steam.

Although the use of SAGD for recovering bitumen in the Athabasca and similar oil sands is showing positive results, limitations as listed below render it problematic. SAGD performs poorly in reservoirs having underlying water with a

near infinite areal extent due to the heat losses that occur in this situation. On site investigations related to SAGD performance in the presence of water yielded the following conclusions:

- Oil recovery in the SAGD process is hindered when water sand is present;
- A given reduction of the oil recovery is inversely proportional to the thickness and the areal coverage of the bottom water layer;
- The presence of a bottom water layer has less impact on recovery than the case where an overlying water layer is present;
- Water coning is avoided by operating and imposing the flowing bottom-hole pressure (FBHP) slightly higher than aquifer pressure.

Despite previous limitations, SAGD can still be an effective recovery technique when the injection pressure is closely controlled and the co-injection of hydrocarbon solvents and non-condensable gases is involved. Solvents can be co-injected with steam as an expanding solvent to improve recovery rates and sweeping efficiency (i.e. overall displacement efficiency). Co-injection of hydrocarbon solvents with steam is being tested and is showing promising results. The underlying theory is for steam to condense contributing latent heat to the formation, followed by the condensation and diffusion of the liquid solvent into the bitumen. Such decreases of viscosity would induce a substantial increase in the production rate and therefore enhance the overall recovery. Table 1.1 represents few SAGD projects that have been experimented with co-injection of hydrocarbon solvent.

Table 1.1 Summary of oil production and Steam Oil Ratio (SOR) results for three major co-injection operations (Redford, 2011).

Pilot Projects	Production Improvement (%)	Steam Oil Ratio Improvement (%)
Christina Lake	80	62
Senlac	70	40
Cold Lake	30	32

1.2.2 Steam Assisted Gravity Drainage (SAGD): Recovery Technique Stages

The SAGD process generally consists of three consecutive stages: Start-Up, Conventional SAGD, and Blow-down. General description of these stages is explained as below:

- Start-Up stage (~ 12 months): Commonly called preheat and rising steam stage, this SAGD phase involves continuous circulation of steam into both production and injection wells toward achieving an adequate hot communication between them, as shown in Figure 1.5. During this stage, the SAGD steam chamber is continuously rising up and expanding toward the formation top, allowing an adequate and appropriate heat transmission within an important portion of the reservoir (i.e. building a heat bridge from the bottom up to the top of the bitumen bearing formation). The continuous injection of stream, at an appropriate pressure, helps in maintaining a consistent temperature along horizontal wells to ensure uniform heating while building up the reservoir pressure to accelerate the bitumen lifting later on, during the conventional SAGD stage.
- Conventional SAGD stage (~ 12 to 36 months): This stage involves steam injection into upper well and producing drained oil and steam condensate from lower well. It is recommended that the injection pressure is slightly higher than the basal water zone pressure thus reducing heating losses.
- Blow-down stage (~ 3 to 6 years): This stage involves the co-injection of gas (e.g. methane) with steam to produce the remaining fluids from the previous stage of SAGD process. Natural gas was co-injected with the steam to maintain reservoir pressure, reduces heat losses and improves oil production. The co-injection of methane with steam in SAGD has been demonstrated to consistently improve the SOR

(~1.5) by inducing an additional rise of steam chamber growth during co-injection period. The production enhancement of some SAGD wells could be explained by the improved drainage of accumulated fluid within and above the steam chamber.

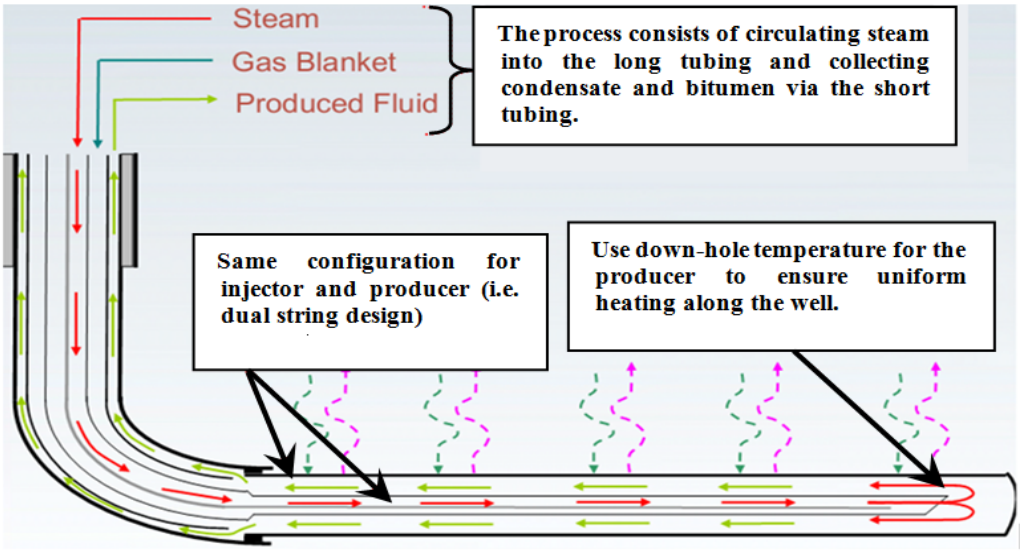

Figure 1.5 Stream circulation process during Start-Up stage (Mathieu Rae et al., 2011)

In any of previous SAGD stages, the reservoir undergoes important stresses that can potential lead to changes in its geomechanical properties. As previously mentioned, most of SAGD operations exist in an unconsolidated formation in which stress-strain phenomena take place. During SAGD, rock properties such as porosity and absolute permeability are sensitive to either increasing or decreasing effective stress as a result of changes in temperature or pore pressure of the soil. Within these circumstances dealing with geomechanics concepts becomes requirements to assimilate the reservoir response to steam stimulation and so predict its geomechanical behavior during the recovery phase. Only by including the interaction of SAGD and geomechanics can we achieve a more complete understanding of geotechnical mechanisms involved during oil recovery using this robust thermal process.

1.3 Geomechanics Aspect of the Steam Assisted Gravity Drainage (SAGD)

Geomechanics are not traditionally taken into account in the simulation of thermal recovery of heavy oil. Lab permeability measurements taken from in situ cores are usually used as input for absolute permeability of the reservoir during simulation and are commonly assumed to remain constant during the steam stimulation process (SAGD). The previous assumption was repetitively revoked by many previous experimental researches and field evidence that proved an important dependency of absolute permeability on the alteration of state of stresses within the reservoir. Actually, field observations and lab tests both suggest that an important expansion within the area surrounding the steam chamber would occur as a result of the thermal effect associated to the injection of steam into the oil bearing formation. Such expansion will impart a proportional increase in the porosity of the reservoir, and thus enhancing its absolute permeability (Dusseault 1979). A comparable soil behavior was also reported to result from the rise in the pore pressure of the reservoir upon steam injection (Chalaturnyk 1996).

Understanding the effect and consequence of the reservoir behavior during the SAGD process requires knowledge of geomechanical processes, which are fundamentals to understand stress-strain phenomena taking place in porous media. A common method to illustrate geomechanical processes is to plot the "stress path" that zones within the reservoir will follow during the SAGD process. The stress path concept is an important geomechanics methodology to identify the fundamental mechanisms involved during a certain stage of the reservoir life. It also allows the complex impacts of SAGD process to be segregated into different simple stress paths that could be easily simulated in laboratory environment. For instance in his study regarding SAGD effect on the geomechanics properties of sandy reservoirs, Chalaturnyk (1996) reported that the stress state governing the reservoir during SAGD could be effectively

presented by two main stress paths. The first path was the increasing of mean effective stress due to the thermal expansion occurring within and in front of the steam chamber during steam advancement in the reservoir (Figure 1.6). And the second path was suggested by Chalaturnyk (1996) to be the decreasing of mean effective stress resulted from the increase in pore pressure that take place upon steam injection (Figure 1.7).

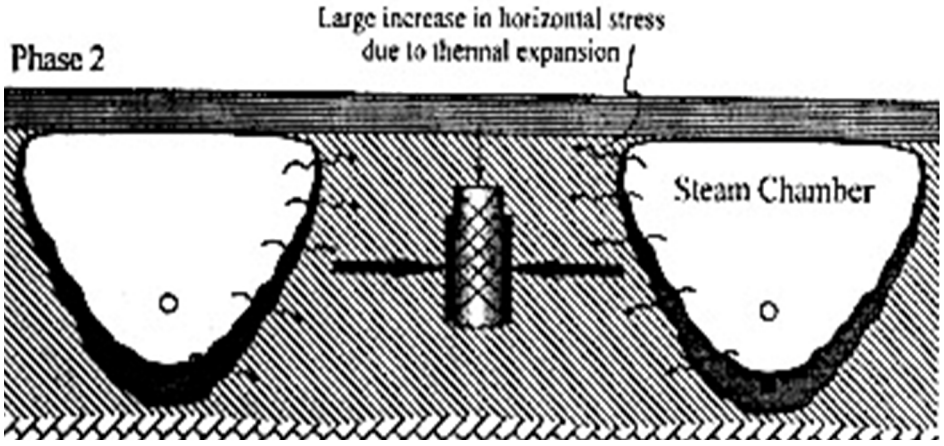

Figure 1.6 SAGD's first stress path: Increase in horizontal stress due to thermal expansion (Chalaturnyk, 1996)

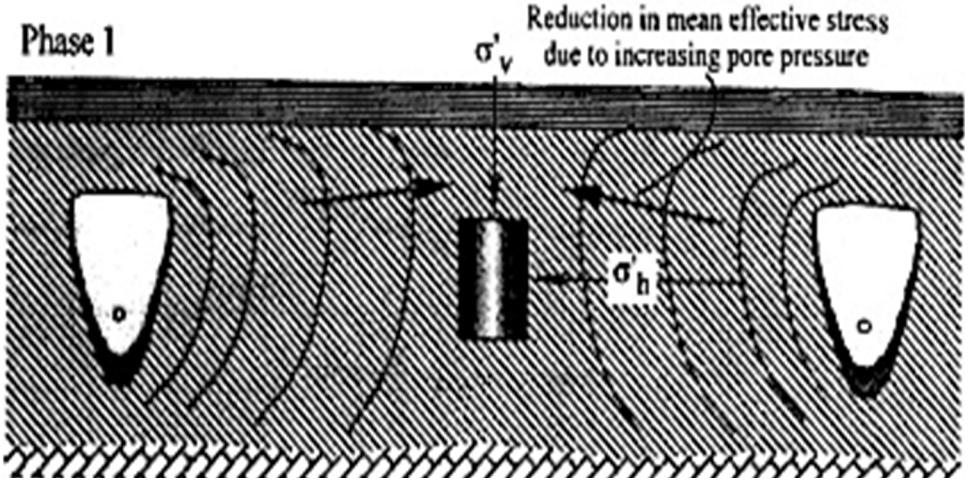

Figure 1.7 SAGD's second stress path: Decreasing of mean effective stress due to pore pressure increase (Chalaturnyk, 1996)

Touhidi (1998) inferred that at in situ conditions, the actual stress path followed by the reservoir would be actually lying between the isotropic unloading stress and the increasing of mean stress paths. A combination between previous paths (path 1 and 2 as presented in Figure 1.8) was represented by Yaich (2008) through his radial extension test. Yaich (2008) believed that the radial extension test is more appropriate to simulate the actual stress path tracked by reservoir during the SAGD process.

For the purpose of comparison, previous stress paths (increasing of mean stress, decreasing of mean stress, and radial extension path) were presented on the "p'-q" diagrams plotted in Figure 1.8, where (p') and (q) are the effective mean stress and the differential stress, respectively, as defined by following equations (Equations 1.1 and 1.2):

$$p' = \left(\frac{\sigma'_1+\sigma'_2+\sigma'_3}{3}\right), \text{ and} \quad \text{(1. 1)}$$

$$q = (\sigma'_1 - \sigma'_3), \quad \text{(1. 2)}$$

where (σ'_1), (σ'_2), and (σ'_3) refer to the three principal effective stresses applied on the soil for a given loading conditions.

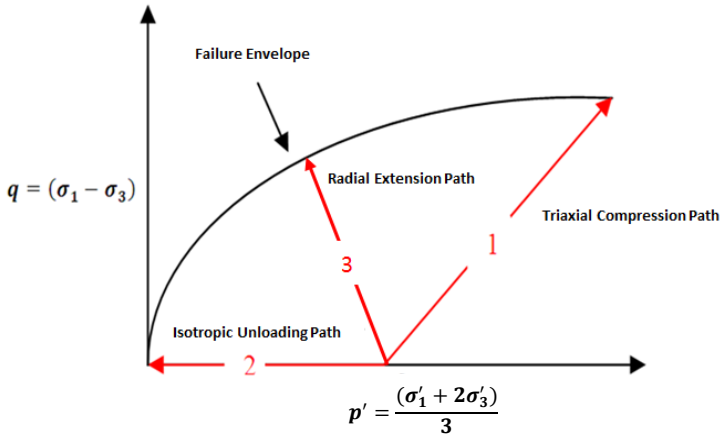

Figure 1.8 Schematic Illustration of stress paths followed by reservoir during SAGD

In a triaxial compression test, (σ'_1) is commonly assigned for the most compressive principal stress, which is typically the axial stress while (σ'_3) and (σ'_2) are respectively standing for the intermediate and least stresses supplied by confining fluid. The intermediate stress (σ'_3) and the least stress (σ'_2) are usually equal for a standard triaxial experiment (i.e. $\sigma_3 = \sigma_2$). Consequently, Equation 1.1 can be rewritten as:

$$p' = \left(\frac{\sigma'_1 + 2\sigma'_3}{3}\right) \quad \text{..... (1. 3)}$$

From an experimental perspective, the first component of SAGD stress paths (increasing of mean effective stress) can be represented by a conventional triaxial compression test in the way that with the increase of the axial stress, the differential stress goes up and so the sample undergoes an important shearing that would induce a significant expansion in the sample volume. Such volume gain believed to be representative of the expansion occurring at the reservoir level as result of temperature increase during the steam stimulation of oil sands. On the other hand, the second component (decreasing of mean effective stress) is usually simulated by an isotropic unloading test wherein pore pressure are held constant and only the confining cell pressure is gradually decreased. The radial extension path was dictated that after an initial axial loading, the confining pressure is decreased while maintaining both pore pressure and axial stress constant.

SAGD imposes elevated pressures and temperatures on the reservoir. These elevated pressures and temperatures alter the rock stresses sufficiently to potentially cause shear failure within and beyond the steam chamber (Collins et al. 2002). The Mohr-Coulomb failure criterion is a common used method to diagnose shear failure condition for soil where the shear stress required for failure, (τ), is defined in terms of the effective stress and the material properties. The Mohr–Coulomb failure criterion is typically demonstrated in form of linear

envelope obtained from a plot of the shear strength of a soil versus the applied normal stress (Figure 1.9). The previous relationship between shear strength and applied normal stress is usually expressed as:

$$|\tau| = \sigma_n' \mu + c', \quad \text{..... (1. 4)}$$

where (σ_n') is the normal effective stress applied to the shear plane, (μ) is the coefficient of internal friction (μ = tan ϕ', where ϕ'=angle of internal friction), and finally (*c'*) is the cohesion coefficient of the material. For cohesionless soils such uncemented sands, the coefficient (c') is usually zero.

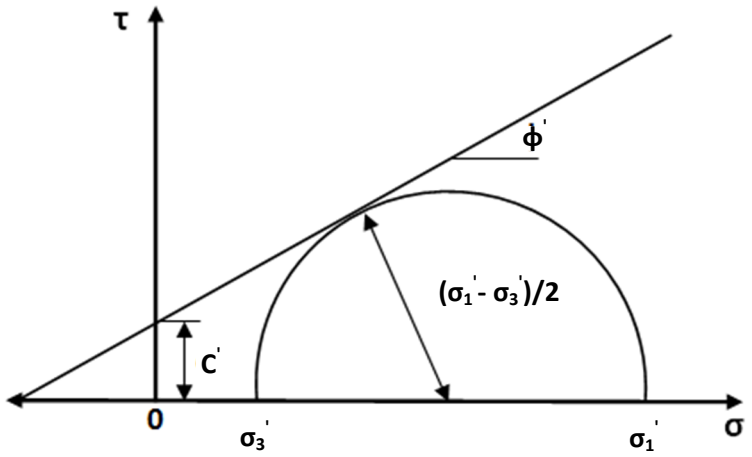

Figure 1.9 Mohr-Coulomb diagram

Recent research (Desrues and Vigianni 2004) has attributed the failure of the unconsolidated sands to the pervasive development of the shear bands upon shearing of the soil. Shear bands represent a common type of localized brittle deformation that occurs in unconsolidated sandstones during shearing. Increasing mean stress on sand samples causes it to compact intially and after a certain increase of shearing stress, soil starts demonstrating an important increase in porosity in localized zones of its grains structure known as shear or deformation bands. As the differential stress continues to increase, the localized zones start agglomerating to form narrow bands with high porosity. When the

ultimate shear strength of the soil is exceeded, the development of large shear bands becomes pervasive and a total collapse of the soil takes place. Soil collapse is usually associated with the development of a major failure plane across the formation that would vary in nature (discrete or not) depending on the type of the soil being tested.

The stresses in the rock will determine the configuration and directionality of the shear band growth; these are largely a function of the confining loading and the intrinsic properties of the soil mainly in initial porosity, density, and grain sorting. Experimental data from Desrues (2004) suggested that soils with high initial porosity generally show a higher sensitivity to shear bands development, which makes them more susceptible to failure in shear comparing to soils with low porosities. In addition, Desrues (2004) observed that the width of shear bands showed a trend toward decreasing with increasing confining stress and intial density of the soil. In general, Desrues (2004) results reported a strong relationship between shear bands configuration and the absolute permability enhancement observed during the dilative shearing of the soil.

1.3.1 Terzaghi Principle and Drained Triaxial Compression Test

Comparable to other geomechanics methodology, the stress path concept also rests on Terzaghi (1943) effective stress principle. Terzaghi (1943) mentioned that the response of the soil to any kind of external loads relies more on the effective confining stress (σ') rather than the total stress applied. The total stress will actually sustain both the sand matrix and the pore fluid. The pore pressure that is also acting on the grain matrix, but in adverse way to the total stress, would compensate an important portion of the total stress applied and thus grains would sustain only the resultant constraint (σ'). Terzaghi (1943) was the first scientist who introduced the effective stress term to refer to the force acting solely on the matrix grain of the soil. He stated that the effective stress ($\sigma^{'}$) could be obtained by deducting the pore pressure from the total stress (σ)

acting on the soil (i.e. Terzaghi concept: $\sigma' = \sigma - P_P$). Thus any typical soil deformation would be mutually linked to the magnitude of effective stress and not to the total acting stress, as seen in Figure 1.10.

As previously stated, simulation of the SAGD geomechanical impacts is usually achieved through a drained triaxial compression tests. The drained test is a standard compression test, in which the specimen is first isotropically consolidated and then is subjected to shearing by rising axial stress at a constant rate and under full drainage conditions.

In a compression test, the volume variation caused by shearing is usually evaluated through the volumetric strain parameter (ε_v), which is defined as the ratio of the change in volume of the sample to the deformation to its original volume. For purpose of analysis, the following graphical presentation of three-dimensional stresses (Figure 1.11) was developed to illustrate the stress-strain relationship that may take place in the soil during a specific loading.

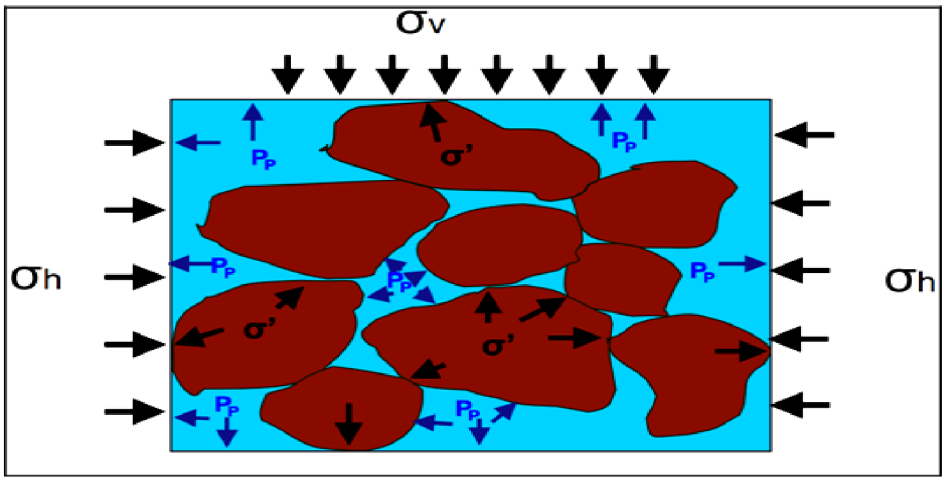

P_p: Pore pressure
σ': Effective stress acting on grain
σ_h: Horizontal stress
σ_v: Vertical stress

Figure 1.10 In-situ stresses at the pore scale (modified from Yaich, 2008)

Under all-around compression conditions, the resulting volumetric strain would be the sum of the linear strains in three mutually perpendicular directions, x, y, and z. Thus volumetric strain (ε_v) could be calculated through following equation (Equation 1.5):

$$\varepsilon_v = \varepsilon_{xx} + \varepsilon_{yy} + \varepsilon_{zz}, \quad \text{..... (1. 5)}$$

where (ε_{xx}) is the normal strain in the x-direction, (ε_{yy}) is the normal strain in the y-direction, and (ε_{zz}) is the normal strain in the z-direction.

The relationship between volumetric strain and axial strain is usually given by the following equation derived from Hooke's law for elastic material:

$$\varepsilon_v = \frac{(1-2\,\nu)}{E}\ (\sigma_{xx} + \sigma_{yy} + \sigma_{zz}), \quad \text{..... (1. 6)}$$

where (E) is Young's modulus, (v) is Poisson's ratio, (σ_{zz}) is axial stress, (σ_{xx}) is maximum horizontal stress, and (σ_{yy}) is minimum horizontal stress.

In a typical triaxial testing program, both maximum and minimum horizontal stresses are usually equal to confining pressure ($\sigma_{confining}$), so the previous Equation 1.6 can be rewritten as:

$$\varepsilon_v = \frac{(1-2\,\nu)}{E}\ (\sigma_{axial} + 2\sigma_{confining}), \quad \text{..... (1. 7)}$$

In terms of effective stresses, Equation 1.7 can be reformulated as:

$$\varepsilon_v = \frac{(1-2\,\nu)}{E}\ (\sigma'_{axial} + 2\sigma'_{confining}), \quad \text{..... (1. 8)}$$

where (σ'_{axial}) is effective axial strain, and ($\sigma'_{confining}$) is effective confining stress.

In the laboratory, it is more convenient to monitor the volumetric strain of the sample by means of volume change device that measures the quantity of water expelled from sample during loading. Details about the measuring equipment

will be discussed in next chapter. It is worth mentioning that for porous soil, Young's modulus (E) and Poisson's ratio (v) are strongly sensitive to effective confining pressure applied. Experimental evidences suggest that both parameters ((E) and (v)) are not actually constant but increase with increasing overburden pressure (Table 1.2).

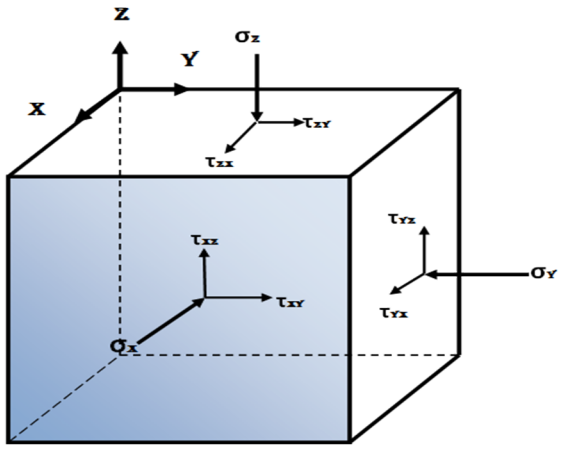

Figure 1.11 Graphical representation of three dimension stresses

Table 1.2 In-Situ Rock Elastic Constants (Tiab and Donaldson, 2004)

P_c (MPa)	T (°C)	E (GPa)	ν
Vertical Tests for C_o=248 MPa			
0	23.9	15.9	0.14
6.9	23.9	35.9	0.24
13.8	23.9	43.4	0.23
27.6	23.9	44.8	0.30
34.5	23.9	47.6	0.31
34.5	87.8	44.1	0.30

All samples have been cored along vertical direction.
P_c: confining pressure
C_o: ultimate compressive strength.

1.3.2 Sensitivity of SAGD Impacts to Geological Configuration of the Reservoir

A full understanding of the reservoir geology is an essential key to assessing the geomechanical processes during the SAGD process. The geological configuration

will determine the directionality of the steam chamber growth and thus orientation and magnitude of the rock thermal expansion. These are largely functions of the overburden depth and underlying tectonic regime.

Geological studies in the Western Canadian Sedimentary Basin (WCSB) have shown that most of the Canadian heavy oil shallow reservoirs have been subjected to tectonic stress loading. Such specific configuration is mainly attributed to tectonic interaction between the North American and Pacific plates taking place nearby the western Cordillera (i.e. the Pacific plate is overriding the North American plate which is causing all reservoir formations to dip towards the western Cordillera (Figure 1.12). This implies that the maximum horizontal stress, (S_{Hmax}), is the most compressive principal stress within the shallow part of the Albertan oil sand deposits ($S_{Hmax} > S_{hmin} > S_V$). Upon steam injection, the thermal-induced volumetric increase will typically rise the differential stress ($\sigma_1 - \sigma_3 = \sigma_{horizontal} - \sigma_{vertical}$) and so escalate the mean stress in the oil sand formation. This increase in the mean stress will impart a proportional growth in the shear stress acting on the sand, and consequently, a dilative shearing will take place in the reservoir of concern. For shallow deposits, the horizontal expansion of the sand is significantly constrained by rock formations surrounding the reservoir. Therefore, during thermal dilation the sand can expand freely in the vertical direction while the horizontal movement is significantly constrained. This conditions lead to the development of shear stresses within the reservoir.

The increase of pore pressure, due to steam injecting during SAGD process, will also convey the same effect on the horizontal stress that would proportionally increase with the rise of pore pressure. This increase in the horizontal stress could be determined through Blanton and Olson (1999) equation:

$$\frac{\partial (\sigma_{hmax})}{\partial (P_p)} = \frac{1-2v}{1-v} \alpha_p, \quad \text{..... (1. 9)}$$

where (σ_{hmax}) is the maximum horizontal stress, (P_p) is the pore pressure, (v) is Poisson's ratio, and (α_p) is the Biot's pore-elastic constant defined in following equation:

$$\alpha_p = 1 - \frac{C_{matrix}}{C_{bulk}}, \quad \text{..... (1. 10)}$$

where (C_{matrix}) is the grain matrix compressibility and (C_{bulk}) is the bulk compressibility.

In unconsolidated sands, Biot's factor (α_p) is commonly close to 1. For stiff rocks, where bulk matrix is only moderately compressible, the Biot's factor (α_p) will be typically less than 1.

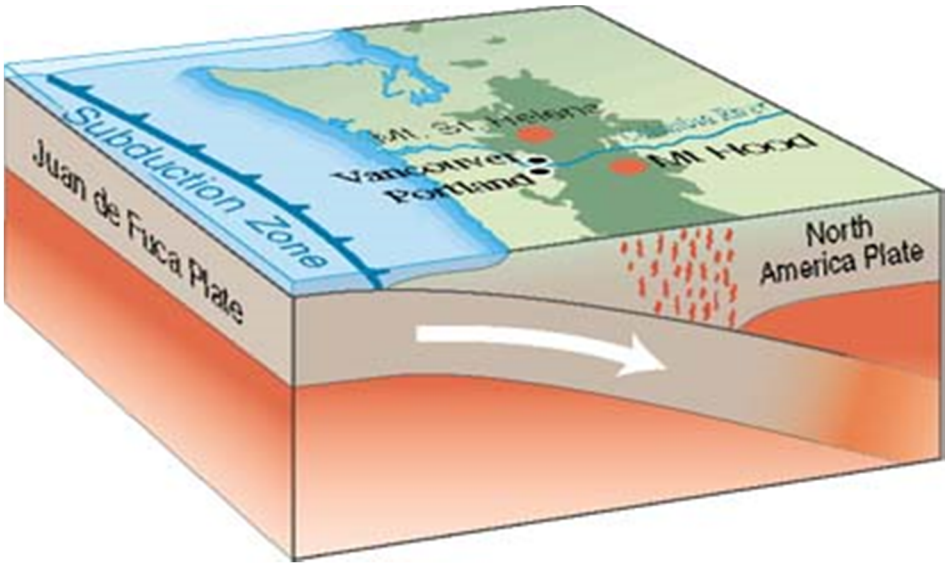

Figure 1.12 Graphical representation of tectonic interaction between the North American and Pacific plates (United States Geological Survey, 2012)

1.4 Literature Review: SAGD Stress Paths and Associated Permeability Variations in Prior Studies

Within the reservoir, the SAGD induced-shearing process is mainly occurring in the area surrounding the injection well and typically within the steam chamber zone. The increase of the thermal gradient combined with decrease of effective stress caused from pore pressure rise would result in soil deformation throughout the reservoir. Such deformations will consequently convey an important variation in petro-physical properties of the formation, which can vary in space and in magnitude depending on the soil properties (i.e. density, initial porosity, grain morphology, thermal conductivity of the soil, etc.) and SAGD operation parameters (i.e. steam injection pressure and temperature, wells locations and dimensions, injected fluid properties, etc.). Appraising such impact on the absolute permeability of the soil, from quantitative and qualitative perspectives, has been the subject of several prior studies in literature.

During his experimental investigations, Scott et al. (1994) simulated the impact of SAGD process on the reservoir by examining the effect of temperature and shear stress changes on the absolute permeability of the sand. Scott's tests were conducted on samples cored from Cold Lake oil deposit located in the north of Alberta. Results from shearing tests showed an improvement of permeability of 10% at effective confining pressure of 1 MPa. There was however, a substantial decrease of 32% in the absolute permeability when samples were sheared at a higher effective pressure of 7 MPa. This permeability reduction was attributed to the grain scale crushing that occurs due to tensile failure of grains. In addition, Scott (1994) reported that an isotropic unloading of effective confining pressure would also lead to important increase in absolute permeability, almost 16% gain, when samples are isotropically unloaded at low range of effective confining pressure.

In the same regard, Oldakowski (1994) studied the impact of different stress paths, such as isotropic unloading and increasing mean stress paths, on sand samples with uniformly distributed porosity and permeability. Oldakowski's samples were cored from wells drilled at the Underground Test Facility site near Fort McMurray. Test specimens were 38.1 mm in diameter and had a length: diameter ratio of 1. Specimens were then consolidated at an isotropic confining stress of 7 MPa prior to starting the experimental test. Most of Oldakowski compression triaxial tests were conducted at relatively low effective confining stress level of 480 kPa to 3000 kPa. Oldakowski's results showed an increase of permeability, varying from 25% to 65%, at effective confining pressure lower than 1000 kPa. A significant increase in permeability was also noted for the isotropic unloading path to reach a maximum enhancement of 70% during an eventual decrease in the effective confining stress of 4400 kPa to 340 kPa. It is important to note that the highest permeability change was associated with samples that had a low initial permeability. This observation was valid for both triaxial compression and isotropic unloading tests.

Touhidi-Baghini (1998) also initiated a similar experimental testing program on intact and reconstituted samples extracted from an outcrop of the McMurray Formation located in the north of Alberta, Canada. The initial permeability of the samples ranged between 1 to 3 Darcy while their average initial porosities were around 33.9% for the samples cored vertically (vertical cores), 33.7% for samples cored horizontally (horizontal cores), and 34.3% for reconstituted samples, see Figure 1.13. Most of the triaxial experiments were conducted under drained condition at low effective stress ranging between 250 kPa and 1100 kPa. Touhidi (1998) replicated the SAGD effect on soil reservoirs through two predominant stress paths. The first stress path was the isotropic unloading and it was experimentally conducted by increasing the pore pressure under initial anisotropic stress (effective mean stress decreases due to steam injection). The second stress path was the increasing of mean stress and was achieved through

undrained compression triaxial tests (thermal expansion resulted from SAGD). Nevertheless, Touhidi inferred that at in-situ conditions the actual stress path followed by the reservoir would be between the isotropic unloading stress and the increasing of mean stress paths. The total four stress paths suggested by Touhidi (1998) are presented in Figure 1.14. Touhidi (1998) experimental results showed a maximum permeability increase by a factor of 6% at 10% volumetric strain for vertical cores, and a lower permeability enhancement was recorded for horizontal cores with a total gain of 50% at 4% volumetric strain. The highest increase in permeability was reported for the reconstituted sample with a 70% of permeability enhancement at 7% volumetric strain. The permeability results of Touhidi (1998) depicted the same trend: an initial permeability decrease followed by an axial permeability increase observed immediately before failure of the sample. These results were attributed to initial compaction and porosity decrease at low strain levels and onset of dilatancy (gain in porosity) before failure.

Dusseault (1977) performed tests on Athabasca oil sand samples cored from wells boreholes located nearby North of Fort McMurray. The specimens were initially trimmed to 76 mm of diameter with a height to diameter ratio of 20.9 before being stored in chilled insulated boxes to preserve its in-situ properties. Samples were then consolidated under 1000 kPa prior to sustaining an effective confining pressure of 400 kPa during the experimental course. These samples showed a higher shearing strength than Touhidi-Baghini cores but smaller volumetric strains during shearing in comparison to Touhidi (1998) and Oldakowski (1994) works. Touhidi associated the higher strength displayed by Dusseault's samples to the important disturbance of specimens during coring and testing. Results of previous experimental studies (Dusseault 1977, Oldakowski 1994, Touhidi 1998) are shown in Figure 1.15.

Dusseault (1977) loaded samples under triaxial conditions at confining stress of 0.4-2 MPa wherein permeability measurements were run in the vertical direction, parallel to the maximum stress direction. Similarly to Touhidi (1998) and Scott (1994), Dusseault (1977) reported a strong correlation between permeability variation and volumetric strain changes during shearing. Dusseault (1977) stressed that at a high range of confining stress, above 1 MPa, a permeability enhancement could not occur even with a higher increase of deviatoric stress which corresponds to a higher degree of shearing dilation. This observation was confirmed by Yaich (2008) in his experimental study investigating absolute permeability variation during shearing and its sensitivity to grain morphology of the soil. Yaich (2008) noted that at a high range of confining stress, there was no permeability enhancement despite the high rate of sample dilation showed at the end of the test. Indeed, Yaich (2008) conducted a series of confined compression tests under both increasing and decreasing of mean stress conditions (i.e. triaxial compression and radial extension tests). In general, core samples with fine grain showed a more pronounced increase of permeability during dilation in comparison to coarse grained samples. The maximum permeability improvement of 42% was reported at 10% axial strain during the radial extension tests for fine grained samples. Under the same loading conditions, however; coarse grained samples depicted a permeability decrease of 10 % by the 10% axial strain. All radial extension tests were initiated at an isotropic compression stress (i.e. effective axial stress) of 1378 kPa. On the other hand, a lower permeability enhancement was reported during Yaich's (2008) compression tests conducted at an effective confining stress of 345 kPa; only 12% and 8% of absolute permeability increase was respectively observed for fine grained and coarse grained samples by the 10% axial strain. The results showed a trend toward permeability reduction with increasing confining stress. Raising the confining stress to 1378 kPa has suppressed permeability enhancement of 12% achieved for the 345 kPa effective confining pressure case. This occurred despite

the important gain of volumetric strain achieved at the end of 1378 kPa tests. In general, results from Yaich (2008) experimental study showed an important data scattering depending on the loading conditions (stress path followed) and the geomechanical and morphologic properties of the soil.

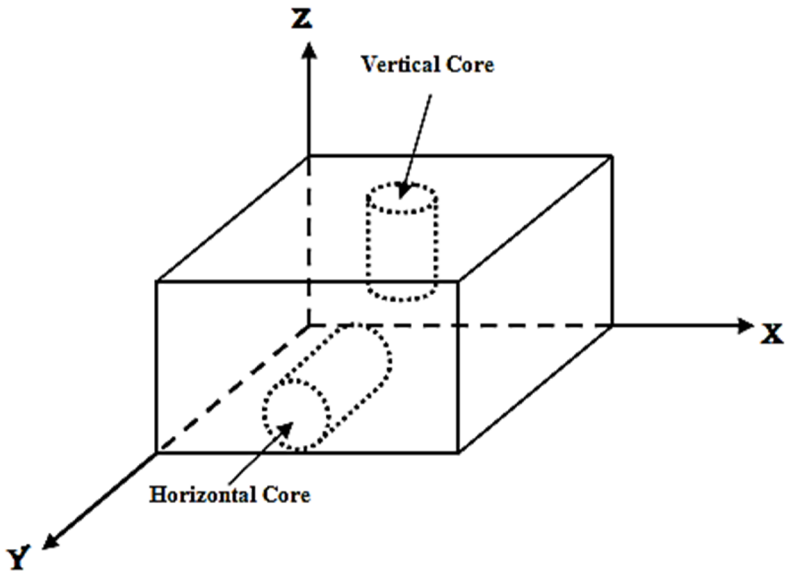

Figure 1.13 Schematic of vertical and horizontal core specimens (Touhidi, 1998)

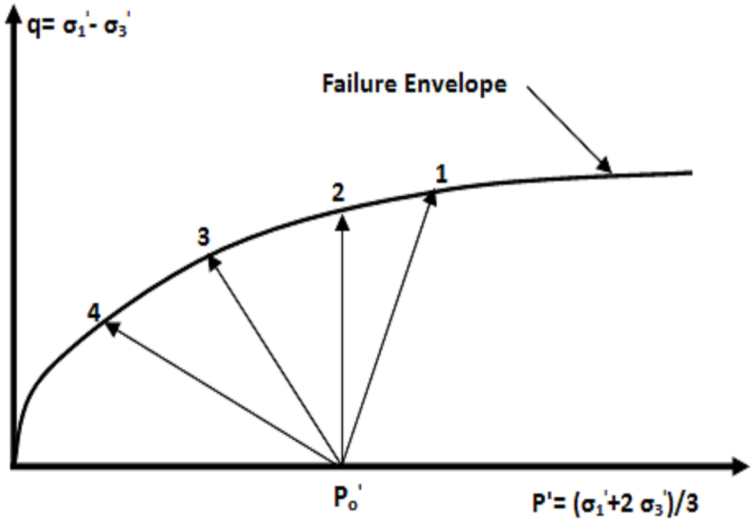

Figure 1.14 Schematic illustration of stress paths investigated by Touhidi (1998)

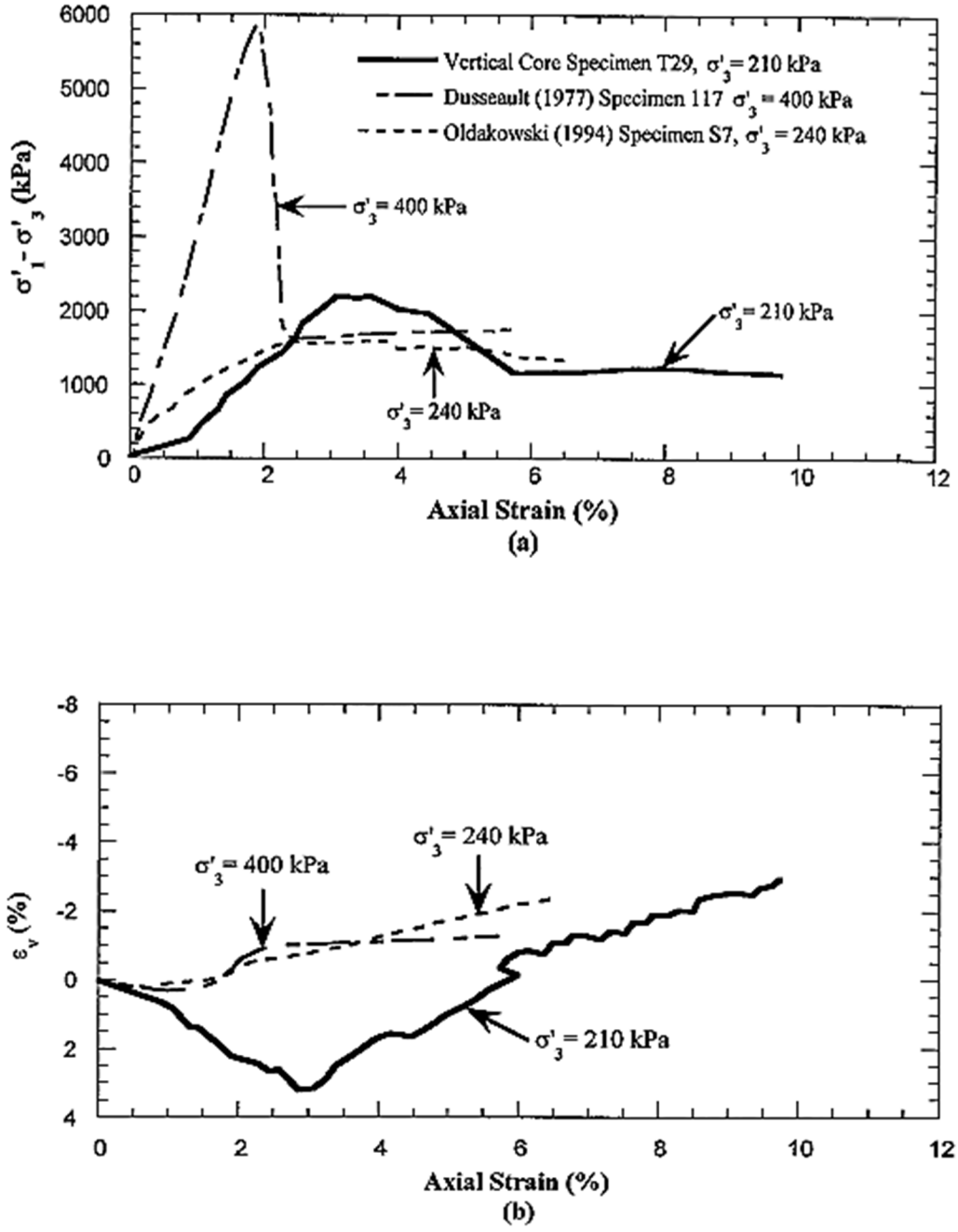

Figure 1.15 Previous studies results (retrieved from Touhidi-Baghini, 1998)

1.5 Research Objective

The current study is intended to cast an additional light on the geomechanics effect of SAGD process on the intrinsic properties of the oil-bearing formation, and particularly acquiring a better understanding on the evolution of absolute permeability during oil recovery stage. As discussed in the previous section, it is important to capture the dependence of absolute permeability on the stress state alteration in numerical reservoir simulation. However, typical data inferred from the experimental studies often exhibit significant scattering depending on constraints governing the stress state applied on the soil and its initial properties. A generalized model that provides an accurate estimation of the permeability evolution was and remains the aim of most studies dedicated to investigating the influence of thermal recovery.

In this study, an experimental approach was adopted to evaluate the variation of absolute permeability at different levels of strain and confining stress on granular dense reconstituted cores. Eventually, an empirical model, which includes absolute permeability and volumetric strain, was initiated accordingly to generate a mathematical correlation that integrates important factors such as initial porosity and effective confining stress. The empirical model can provide a reasonable prediction of the absolute permeability behavior at any given volumetric strain and/or confining stress level.

1.6 Research Methodology

During the course of this study, a laboratory test program was completed where a series of triaxial tests were performed, for various stress paths (increasing and decreasing mean stress paths) to adequately replicate the stress state conditions associated with the SAGD process. Previous stress path were simulated in laboratory through both compression and isotropic unloading triaxial tests. All tests were conducted at low confining stress, between 50 kPa and 800 kPa, on unconsolidated artificial sand samples with uniformly distributed porosity and permeability respectively ranging from 33% to 35% and 1.4 to 1.5 Darcy. In general, specimens used in current study are considered representative of Athabasca oil sand except for grain morphology (i.e. for morphology comparison between Athabasca and current study sands, refer to Chapter 3.1). The stress-strain and permeability tests were run at different axial strain levels, results were also discussed, and various correlations were subsequently interpreted.

1.7 Organization of Thesis

Chapter 1 presents the actual circumstance involved and provoking the interest toward the current subject of our study, showcases the important relation between geomechanics properties of soil and its absolute permeability evolution during thermal recovery of the hydrocarbons, explains the thermal recovery process and involved stages, as well reviews pertinent experimental results of previous similar studies, and finally breaks down the chronological order of the thesis chapters.

Chapter 2 explains the experimental procedures and testing approach followed in this research to investigate the effect of geomechanical processes on the absolute permeability evolution as well to qualify the intrinsic properties of the sample. These properties are mainly specific gravity, initial porosity, initial permeability, and grain morphology.

Chapter 3 discusses the experimental results yielded from different tests supported by an extensive theoretical explanation of the soil behavior during shearing.

Chapter 4 summarizes the results of this study and proposes recommendations for future research.

2 Chapter 2 Experimental Apparatus and Testing Procedures

2.1 Experimental Setup

The experimental testing apparatus composed of a typical triaxial cell, an electric motor, frame (Fracmo model P 335, H.P 10 lb. INS, 24 R.P.M, L.W.O D 1635, Serial No. 6), a vacuum pump, an external electric volume change measuring device, a pressure board to control and monitor back/cell pressures, load transducer, axial displacement transducer, and an ISCO-260D syringe pump to conduct permeability test. A Dolphin data acquisition program recorded the signals received from different logging systems (data dolphin high-resolution data logger, Model 400, SN 1750). Both cell and pore pressures were supplied by two different pressurized water reservoirs attached to pressure control and monitor board. The different testing programs are conducted by various combinations and hookups between the triaxial cell, the control systems (Figure 2.7), and pressure/volume measuring devices. Figure 2.1 illustrates the configuration of the testing system.

2.1.1 Triaxial Cell

The triaxial cell (Figures 2.2 and 2.3) consisted of a rigid outer cylinder that is mounted on the apparatus frame, and a piston assembly (axial loading ram) to apply a constant axial stress on the top of specimen by means of a loading cap. The base and the top of the cell were made of aluminum while the outer cylinder was made of reinforced acrylic to accommodate a maximum confining pressure of 1100 kPa. Four 2-way valves were installed in the metallic base of the cell to control the water flow to the different pressure lines.

The sample was held between two pedestals (top and bottom) having the same cross-sectional area as the specimen cylinder and a height of 50.8 mm. Both pedestals were equipped with ports (grooved holes) to permit flow of pore fluids to the sample while the top pedestal was connected to the piston by means of

loading cap, see Figure 2.4. The test specimen of 50.8 mm diameter and 50.8 mm height was encased with latex membrane and properly sealed with O-rings placed onto the upper and lower pedestals (Figure 2.1). Two highly permeable porous stones of 50.8 mm diameter were placed on the top and bottom of the specimen to assure a uniform water flow distribution and as well inhibit any susceptible fines migration (Figure 2.5).

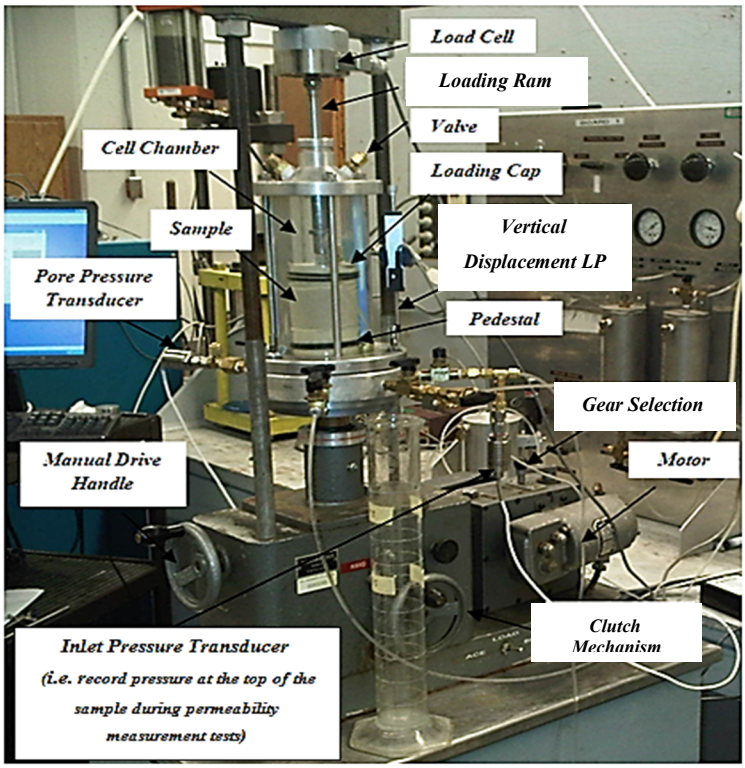

Figure 2.1 Snap shot of the testing system setup

2.1.2 Load Frame and Logging Systems

The load frame is a Wykeham Farrance model equipped with a gear loading system supplying an axial load capacity of 9 KN at a constant displacement pace of 0.06 mm/min. A linear voltage displacement transducer (LVDT) was used to monitor axial displacement during shearing process.

The volume change of the specimen, and thus the volumetric strain, were determined by an external electric volume change measurement device

connected to pore-pressure fluid line (Figures 2.6 and 2.7). A load transducer and pressure transducer were installed to respectively record the axial load and the pore pressure. A second transducer was used to determine the differential pressure across the specimen during permeability measurement tests. Signals generated by different transducers were gathered and recorded by Dolphin data logger device.

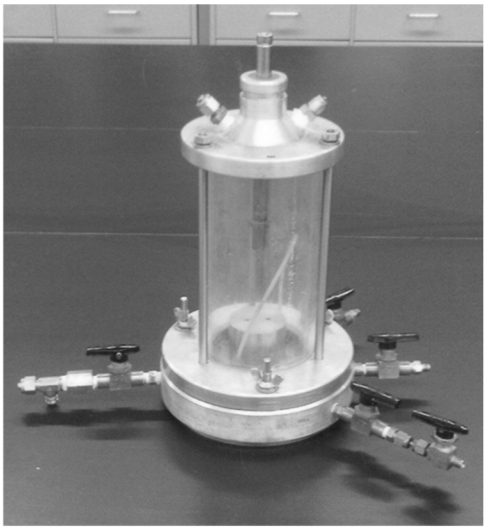

Figure 2.2 Snap shot of Triaxial chamber used in current study

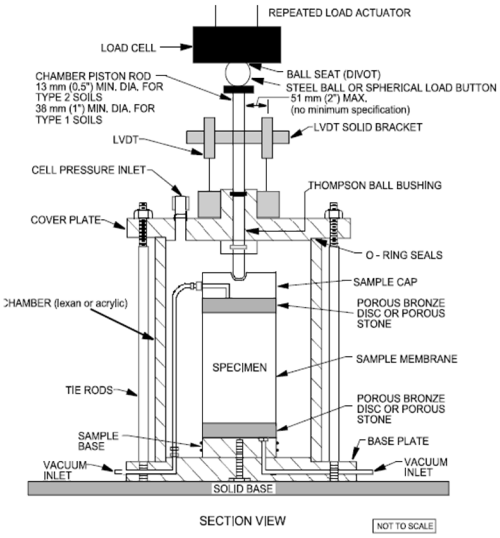

Figure 2.3 Typical triaxial chamber with external LVDTs and load cell (Federal Highway Administration, 2007)

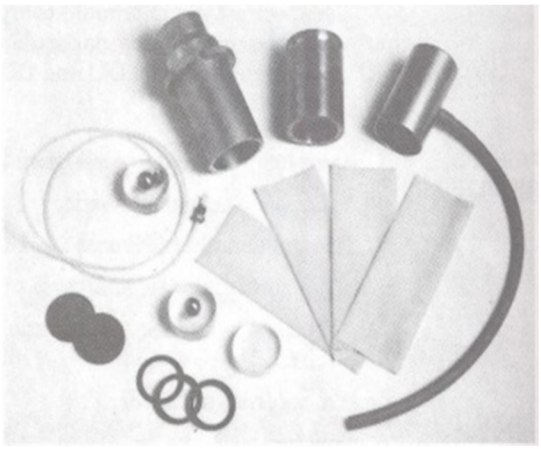

Figure 2.4 Snap shot of triaxial accessories

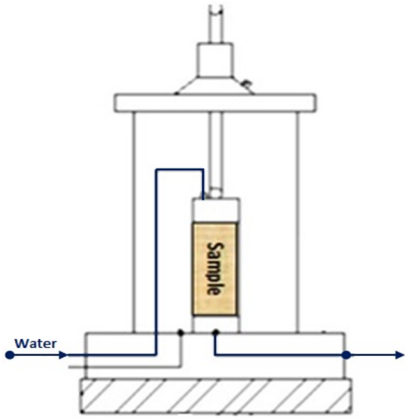

Figure 2.5 Schematic view of flow line

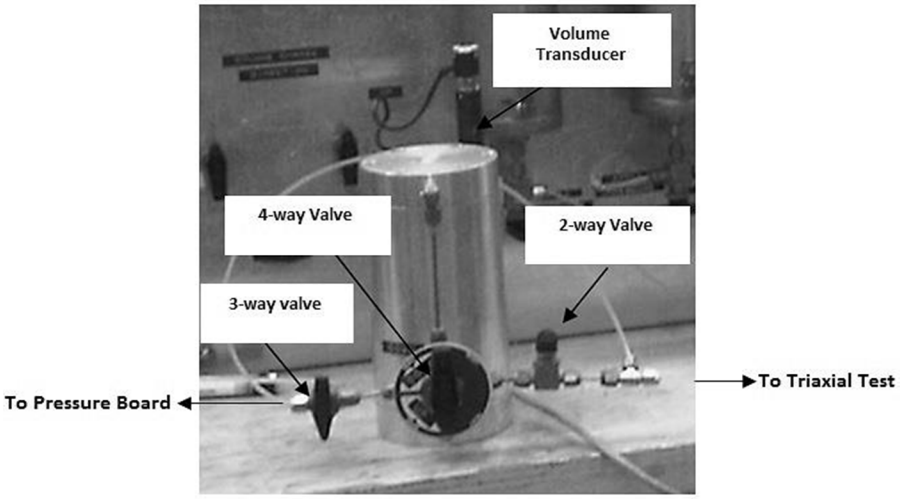

Figure 2.6 Snap shot of the volume change measuring device used in the current testing program

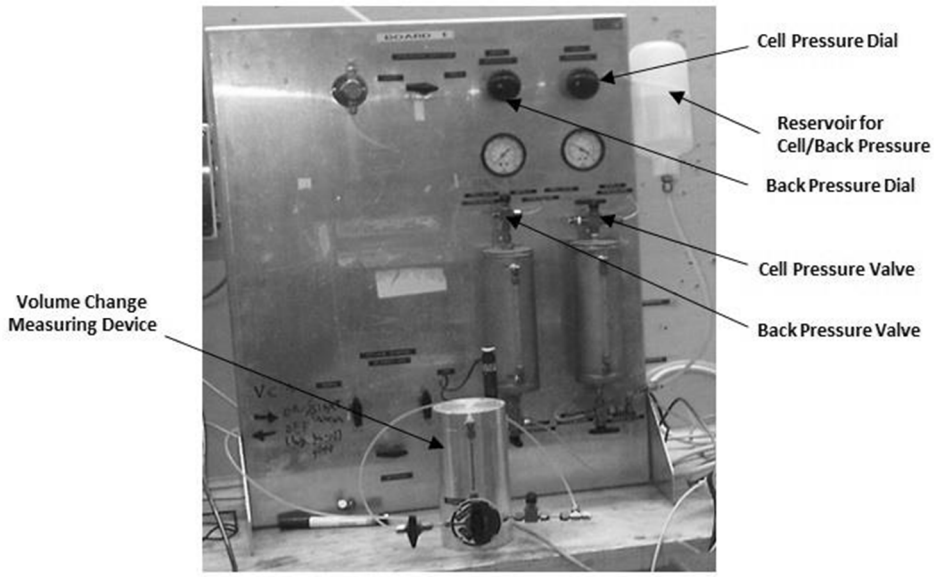

Figure 2.7 Snap shot of pressure board components used in the current testing program

2.2 Soil Particle Density

Similarly to other heterogeneous porous materials, sandy soils are typically composed of three natural phases: the solid phase consisting of the particles matrix, liquid phase mainly water and/or oil, and finally the gaseous phase (air or gas). According to the previous three phase concepts, three types of average density can be defined:

i. Soil density of solids or soil particle density (ρ_s): It is defined as the ratio of the solid phase mass to the volume of the solid phase of the soil. Soil particles density is usually expressed as follow:

$$\rho_S = \frac{M_S}{V_S}, \quad \text{..... (2. 1)}$$

where M_s is the solid phase mass and V_s is the volume of solid phase of the soil. In most sandy soils, the soil particle is ranging from 2.6 to 2.7 g/cm^3 and it is close to the density of the quartz, the main mineral component of sand. In general, the presence of high percentage of solid

organic materials in the sandy soil would decrease its soil particle density (ρ_s).

ii. Dry density of the soil (ρ_d)**:** It is defined as the ratio of the dried soil mass to its total volume including both solid and pore volume. Dry density may be written as follow:

$$\rho_d = \frac{M_s}{V_t} = \frac{M_s}{V_s+V_l+V_g}, \quad (2.2)$$

where M_s is the solid phase mass, V_s is the volume of solid phase of the soil, V_L is the volume of liquid phase of the soil, and Vg is the volume of gaseous phase of the soil. The bulk density of the soil is linked to the soil particle density according to the following relation:

$$\rho_d = (1-\emptyset)\rho_s, \quad (2.3)$$

where $(\emptyset)$ is the soil prosity.

iii. Total, bulk or wet density of the soil (ρ_t): It is defined as the ratio of the total mass of the soil, including both solid and liquid, to its total volume. Total density of the soil is expressed as follow:

$$\rho_t = \frac{M_s+M_l}{V_t} = \frac{M_s+M_l}{V_s+V_l+V_g}, \quad (2.4)$$

where M_s is the solid phase mass, M_L is the liquid phase mass, V_s is the volume of solid phase of the soil, V_L is the volume of liquid phase of the soil, and Vg is the volume of gaseous phase of the soil. The total density of the soil is strongly dependent on the liquid saturation of the soil (S_{Water} or S_{Oil})

Specific gravity, designated as (G_s), is another geotechnical term used to define soil density as ratio of sand solid density to density of distilled water determined at standard conditions (atmospheric pressure and 25^o C). Specific gravity (G_s) is expressed as follows:

$$G_s = \frac{\rho_s}{\rho_{water}}, \quad (2.5)$$

The specific gravity refers only to the solid phase of the three-phase soil system. It does not include the gas and liquid phases present in the pore space. Previous density ratios ($\rho_s, \rho_d,$ and ρ_t) could be easily determined through the experimental procedures described in Appendix A.

Table 2.1 shows the main results obtained from the specific gravity experiments on the sand used in this experimental program.

Table 2.1 Specific gravity of sand used in the current study.

Sand sample	Temperature (C^o)	α (temperature correction)	G_s
1	21	0.9998	2.69
2	21	0.9998	2.72
3	21	0.9998	2.71
		Average of G_s	2.71

2.3 Grain Size Distribution

The distribution of different grain sizes affects the engineering properties of the soil and thus intrinsic characteristics of the reservoir. Sieve analysis is commonly used to determine grain size distribution from coarser to finer grains, within the soil. For our testing program, sieve analysis was conducted in accordance with ASTM D 422-Standard Test Method for Particle-Size Analysis of Soils. Appendix B describes the test procedure for the sieve analysis.

2.3.1 Test Equipment

The test equipment consists of a set of sieves, balance, mechanical sieve shaker, timing device, and cleaning brush (see Figure Appendix B. 2).

2.4 Sand Sample Relative Density

The geotechnical properties of the sand vary considerably depending on the degree of packing of the grains. The packing density of the soil is usually

quantified through the relative density parameter designated by (D_r), which may be described as follow:

$$D_r = \left(\frac{e_{max}-e}{e_{max}-e_{min}}\right) \text{x}100\% \text{ , ...} \quad (2.\ 6)$$

where (e_{max}) is the void ratio at the loosest possible state of the soil, (e_{min}) the void ratio of the soil at its densest possible state and is usually measured after exposing the soil to an important compaction process, and (e) is the current void ratio of the sand sample.

Based on relative density (D_r), the packing density of grains can be described qualitatively by Figure 2.8. For our testing program, relative density was determined in accordance with the following standards:

i. ASTM D4254 - Standard Test Methods for Minimum Index Density and Unit Weight of Soils and Calculation of Relative Density.
ii. ASTM D4253 - Standard Test Methods for Maximum Index Density and Unit Weight of Soils and Calculation of Relative Density.

Appendix C describes the procedure for the Relative Density Test.

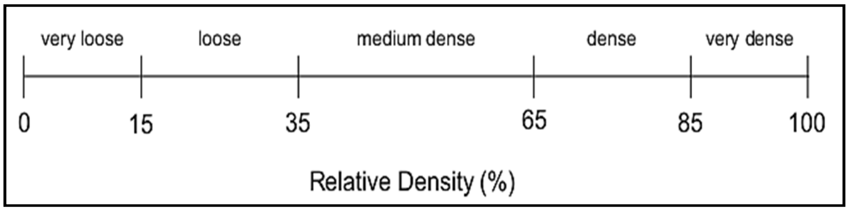

Figure 2.8 Relative density range and soil classification (Sivakugan, 2000)

2.5 Sample Preparation Program

Preparation of samples was conducted in accordance with the "Manual of Artificial Oil Sand Sample Preparation, 2001", a preparation guide that was developed and tested by the geotechnical Group of the University of Alberta.

This technique yielded cylindrical samples with identical dimensions of 50.8 mm diameter and 50.8 mm height. The sample preparation procedure shares an important similarity with the wet vibration technique. Wet vibration was commonly emphasized by previous studies (Hamoud 2012, Khan 2009, and Touhidi 1998) as a method with high repeatability and porosity uniformity in the samples.

The technique deployed in the current testing program consisted of three successive stages: sand preparation, sand densification, and finally sample freezing. The three stages are considered adequate to prepare samples with highly uniformity while avoiding any air bubble development within the sample fabrics. A detailed procedure of the sample preparation was described in the following sections.

2.5.1 Preparation Program, Procedures and Equipment

Figure 2.9 illustrates equipment required for sample preparation: Sand, Split mold, O-rings, bottom pedestal, latex membrane, top plate, top cap, cool blanket, vibration table, vacuum, three porous stones: two of 63.5 mm diameter and one of 50.8 mm as diameter, water, and dry nitrogen ice.

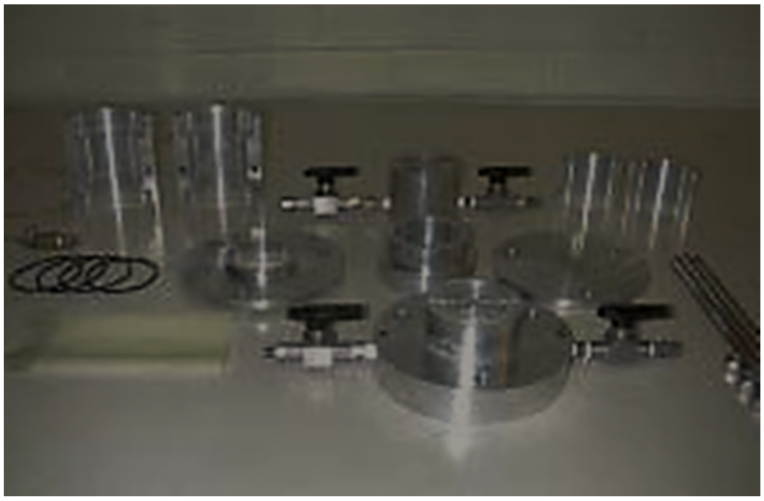

Figure 2.9 Sample preparation equipment

2.5.1.1 Preparation Program Procedure

The following sections describe the sample preparation procedure:

1. First stage: Sand preparation:
   i. Take suitable amount of specimen sand, record its weight, and pour it in beaker;
   ii. Place the beaker onto a hot plate and boil sand and water for 30 minutes to saturate and remove air from the sand;
   iii. Add water to the sand until the beaker is half-full;
   iv. Place the beaker onto a hot plate and boil sand and water for 30 minutes to saturate and remove air from the sand;
   v. Place three porous stones (two of 63.5 mm diameter and one of 50.8 mm diameter) in boiling water for 20 minutes;
   vi. Inspect the latex membrane for obvious product failures (leaks, tiny holes, etc.), Figure 2.10;
   vii. Prepare dry ice in cooler and freezing box for next preparation stage.

2. Second stage: Sand Densification:
   i. Place the latex membrane onto the bottom pedestal, seal it with two O-rings, and put it on the vibrating table, Figure 2.11;
   ii. Turn on saturation valves to allow water to flow into the bottom of the membrane to a depth of 5 mm and then close the valves, Figure 2.12;
   iii. Place a 63.5 mm porous stone on the bottom pedestal. Insure that it is air-free between the porous stone and bottom pedestal;
   iv. Assemble the split mold and place it on the bottom pedestal, Figure 2.13;
   v. Fold the top part of the membrane down over the mold and seal it with two O-rings;
   vi. Attach the vacuum outlet to the suction tube from the split and apply a vacuum at 80 kPa absolute pressure, Figure 2.14;

vii. Carefully pour with a scoop the saturated sand slowly into the membrane and set the vibrating table at a low speed, Figure 2.15;

viii. Place a saturated 50.8 mm diameter porous stone on the top of the sand specimen, then put the surcharge weight and maintain it vertically. The combined porous stone and surcharge set would apply a 14 kPa confining stress to the sample. Insure always-keeping 2 to 3 mm of water on the top of the sample, Figures 2.16 and 2.17;

ix. Set the vibrating table at the fifth speed to settle down the surcharge to a desired level. This latter will come down to a desired level to produce a saturated sample, Figure 2.18;

x. Unfold the membrane, and then remove the surcharge, porous stone and finally the top section of the split mold, Figure 2.19;

xi. Fold again the top part of the membrane down over the mold and place a saturated 63.5 mm porous stone on the sample;

xii. Fill up the mold with water;

xiii. Place the top cap onto the porous stone and let the water drain from the drainage valves, and then close the valves;

xiv. Unfold the membrane onto the top cap and seal it with O-rings;

xv. Place the top plate over the top cap then fasten it into correct position to prevent any uplift action during freezing, Figure 2.20.

3. Third Stage: Sample Freezing:

i. Close the bottom valves, open the top ones, and place the whole set-up into a freezing box with dry ice for approximately 30 minutes, Figure 2.21;

ii. Open apart the split mold and remove the O-rings, and then place a cool blanket around the frozen sand sample to prevent disaggregation caused by ice melting, Figure 2.22;

iii. Heat-up the top and bottom pedestals to take them out of the split mold;

iv. Warm-up carefully the porous stones with hot air to ease their detachment from both sides of the sand sample;

v. Remove the cool blanket and latex membrane, and keep the frozen sample in dry ice, and then place it in freezer, Figure 2.23.

Figure 2.10 Latex membrane inspection

Figure 2.11 Put on the latex membrane

Figure 2.12 Saturating the bottom pedestal

Figure 2.13 Put on the split mold

Figure 2.14 Vacuum pump connections

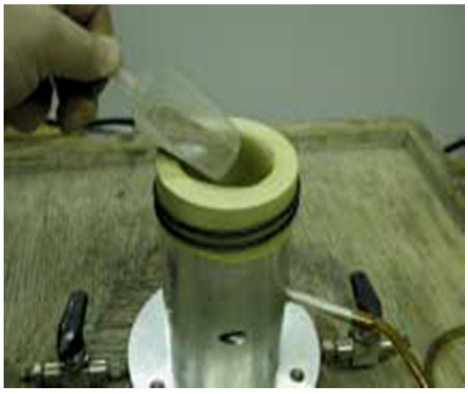

Figure 2.15 Scoop sand into the mold

Figure 2.16 Prepare for sand densification

Figure 2.17 Sample densification

Figure 2.18 End of densification

Figure 2.19 Put on the latex membrane

Figure 2.20 Put the top plate over the top cap

Figure 2.21 Freeze the sample

Figure 2.22 Remove the bottom pedestal and top cap

Figure 2.23 Synthetic sand sample

2.6 Triaxial Testing Program Overview

2.6.1 Triaxial Test Overview

In this study, a series of confined compressive tests were conducted, under both increasing and decreasing mean stress conditions. The increasing mean stress path was simulated through a conventional triaxial compression tests that were carried out in accordance with the consolidated drained (CD) testing procedure. In any of the compression tests, the sample was first placed between two platens, before being isolated from confining cell fluids by a latex membrane,

and then subjected to an effective confining pressure that is maintained constant during the axial loading. The axial load (σ_1) was gradually increased until eventually reaching the sample failure. This procedure was systematically repeated for the three effective confining stresses used in this study: 50 kPa, 200 kPa, and 600 kPa. The required effective confining level (σ'_3) was established by simultaneously adjusting cell pressure (σ_3) and pore pressure (P_p) applied on the sample. In the triaxial compression test the net axial stress, also called deviatoric stress, is determined by deducting the cell pressure (σ_3) from the axial load (σ_1) (i.e. deviatoric stress = (σ_1-σ_3)). The deviatoric stress is the main cause of the axial and radial strain occurring within the specimen during the compression tests. In the end of the axial compression test, a plot of deviatoric stress versus axial strain and volumetric strain versus axial strain were generated in order to evaluate strength and behavior of the sample when being sheared under different levels of effective confining pressure.

The decreasing mean stress condition was replicated through a triaxial isotropic unloading test, where the effective confining stress was gradually decreased while maintaining the zero axial strain conditions (no axial stress was applied on the specimen). For the isotropic unloading test the cell pressure (σ_3) would be the major principal test applied on the specimen. However during the triaxial compression test, the major principal stress would be the summation of the applied axial load (σ_1) and the cell pressure (σ_3).

For both testing programs (isotropic unloading and axial compression experiments) the geometrical dimensions of the specimens before and during the test should be recorded as well inspected for pertinent characteristics. The applied load as well as the specimen deformation (axial and/or radial deformations) should be logged and analyzed to assess sample sensitivity to loading conditions (i.e. stress paths followed and confining level applied).

2.6.2 Triaxial Test Procedure

2.6.2.1 Triaxial Cell Set-up

The main steps of setting up the triaxial cell for consolidated drained (CD) triaxial test are summarized below:

i. Record numbers, technical specifications, and calibrations of all the instruments used in the experiments (load cell, pore pressure, transducers, etc.);
ii. Saturate the ports on the sample pedestal;
iii. Put grease on pedestal and loading cap;
iv. Place wet filter paper on a 50.8 mm pre-saturated porous stone, and then slide the stone with the filter paper on top onto the pedestal;
v. Place the sample on top of the filter and the porous stone;
vi. Place first wet paper, and then the 50.8 mm porous stone on top of the sample;
vii. Carefully place the 50.8 mm latex membrane around sample using the membrane stretcher;
viii. Put loading cap on top of the porous stone with the fittings aligned with the backpressure tube;
ix. Fasten the membrane by placing two sets of O-rings, one set (2 O-rings) around the pedestal and second set around the loading cap;
x. Saturate the backpressure line;
xi. Put carefully the cell over the assembly while keeping the loading ram rise from the sample to avoid any applying load on it;
xii. Fill cell with cool fluid (glycol and water) in order to maintain the initial shape of the sample;
xiii. Hook up pore pressure transducer;
xiv. Calibrate and set the electric volume change device so that the transducer is positioned in the middle of the range;

xv. De-air the backpressure and cell pressure lines by bleeding some water out prior to hooking lines to the cell;
xvi. Connect cell pressure and back pressure lines;
xvii. Keep valves closed;
xviii. Lower loading ram to bring it into contact with sample;
xix. Attach a LVDT (external measurement system) onto the loading to monitor the axial displacement;
xx. Once the triaxial cell is properly mounted, start applying the desired confining pressure by adjusting the back and pore pressure.

2.6.2.2 Samples Saturation Stage

In the aim of bringing the sample to reservoir fluid conditions, the following saturation process was employed:

i. Saturate all lines (pore, back/cell, and ISCO pump line). The ISCO pump line will be used to perform the permeability test (refer to Figure 2.26 for the schematic view of the experimental set up);
ii. Apply 400 kPa of confining stress;
iii. Apply vacuum pump, and then use the ISCO pump to flush sample with water in a successive upward and backward flow to remove imprisoned air typically found between the sample and the porous stones;
iv. Gradually increase cell pressure and back pressure to 410 kPa and 400 kPa, respectively, and hold the system for a period of two days to achieve the back saturation for the specimen;
v. Perform B test (Head, 1986) by following procedure described below.

2.6.2.3 Sample Saturation Appraisal: B-Test

To achieve the saturation assessment, the following procedure was performed:

i. Close volume change and back pressure valves while keeping pore pressure and cell pressure valves open;

ii. Take initial pore pressure and back/cell pressure readings;

iii. Apply 60 kPa of cell pressure;

iv. Allow several minutes for equalization and read pore pressure;

v. Calculate incremental pore pressure increase and then determine the saturation characteristic parameter, (B) (i.e. $B = \frac{\Delta PorePressure}{\Delta CellPressure}$);

vi. Continue applying 60 kPa increments and calculating the parameter (B) for each increment until reaching a total cell pressure of 360 kPa;

vii. If (B) is much less than "1", raise cell pressure to a total of 410 kPa, and then apply a back pressure of 400 kPa and keep sample overnight to saturate. Afterward, apply another increment, and then check again parameter (B). Stop the B-Test when B value becomes constant with increasing and decreasing cell pressure, which provides confirmation that the specimen has reached full saturation. Figure 2.24 provides a typical example of B test results.

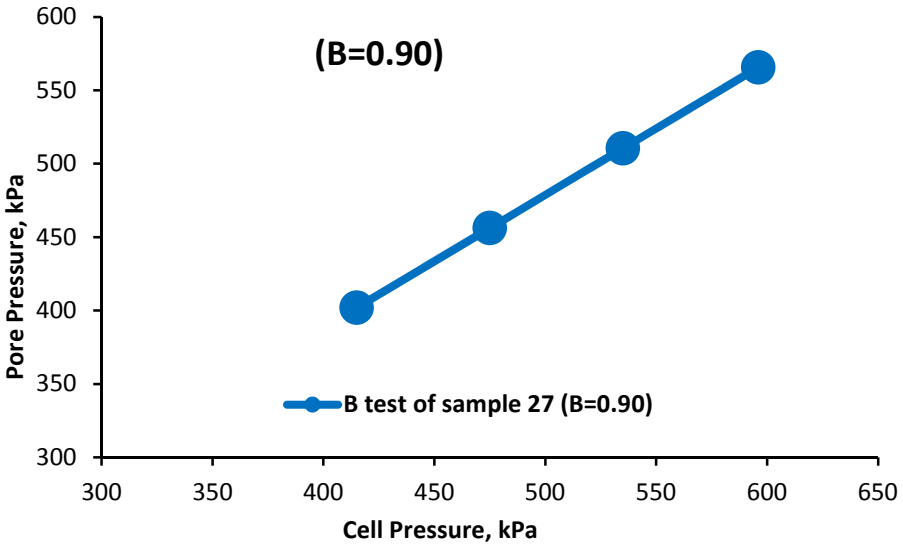

Figure 2.24 B Tests typical curve results

2.6.2.4 Isotropic Consolidation Stage

Isotropic consolidation was employed to establish the initial reservoir stress conditions within the specimen. To minimize the effect of freeze and mounting disturbance for these uncemented sand specimens, a seating load was needed to preserve the initial properties (i.e. porosity and dimensions) of core sample.

i. Start loading at 50 kPa effective confining pressure (σ_3');
ii. Incrementally increase cell pressure and back pressure respectively to establish the effective confining pressure (σ_3') required for the experiment (50, 200, or 600 kPa);
iii. Move the ram down to make contact with the specimen.

2.6.3 Measuring the Initial Absolute Permeability of Sample

The absolute permeability (commonly symbolized as k or k_w) is an intrinsic property of the porous medium and is a measure of the capacity of a porous material to allow fluids to pass through it. It is important to measure the intrinsic (initial) absolute permeability for each sample at the initial stress conditions established after consolidation stage.

The absolute permeability tests were performed using the following procedure:

i. Upward flow is initiated through the specimen at a constant flow rate until a constant differential pressure is achieved;
ii. Calculate the absolute permeability to water (k_w) using Darcy's law; and
iii. Check the value of (k_w) by repeatability of tests (i.e. absolute permeability measurement was repeated three times).

This procedure was systematically repeated for the three effective confining stresses: 50 kPa, 200 kPa, and 600 kPa. The absolute permeability is strongly sensitive to effective stress applied.

2.7 Experimental Testing Program

2.7.1 Triaxial Compression Test

In the triaxial compression test, axial stress was increased at constant rate until failure was reached within the sample. This represented the stress change that would take place as a result of the thermal expansion of the reservoir (the stress path pursued during compression test was shown in Figure 1.8). All triaxial compression tests were conducted under drained conditions, which means no excess or additional pore pressures developed during shearing. This was achieved by keeping the backpressure (pore pressure) valve open during shearing. It is important to mention that prior to shearing, the required effective confining stress (50, 200, or 600 kPa) should be preset by adjusting the cell pressure and pore pressure to the required level.

During the experiment, axial loading was repetitively stopped at different preselected values of axial strain to perform absolute permeability test. These various axial strain levels were completed by using separate, nearly identical, specimens. The shearing process was typically stopped at 15% axial strain for 50 kPa and 200 kPa confining effective stresses. For the 600 kPa test, the absolute permeability enhancement was not achieved by the 15% of axial strain, so shearing was continued up to 18% of axial strain to observe the absolute permeability improvement.

Absolute permeability tests were performed under steady state conditions and for five selected axial strain states (0%, 2%, 5%, 10%, and 15%) covering the full range of deformation behavior of the sample (i.e. elastic, plastic, yielding, post-yielding). Each of these strain locations is noted as red circles in Figure 2.25. During permeability measurements, the steady state condition was deemed to be reached when the pressure drop across the sample had stabilized. Subsequently, Darcy's law was employed to calculate the absolute permeability.

Once the test had achieved the final level of axial strain, the triaxial cell was disassembled and made ready for the next test specimen. The new sample was brought to the subsequent axial strain level before conducting the permeability measurement test again. The permeability measurement procedure was repeated for the different axial strain level of the experiment and typically for each effective confining stress range (50, 200, and 600 kPa). This recommended routine minimized the possible hysteresis impact on the accuracy of the permeability measurements.

Summary of procedure followed during triaxial compression tests is described below:

i. Start shearing with a steady increase in the axial stress at low axial strain rate of 0.06 mm/min;
ii. At every percentage of axial strain, for example at 2% of axial strain, stop the ram, allow loads to stabilize, carry out the absolute permeability test using the steady state method, stop permeability tests, disassemble cell, put in new specimen and start shearing up to 5% of axial strain, stop the ram, perform absolute permeability test again at 5% axial strain, and then stop permeability test, etc.;
iii. Record pressure drop, water flow rates, at regular times;
iv. Before going to the next strain level, a new core sample has to be loaded into cell chamber;
v. Repeat the above steps with each of subsequent strain level (10% and 15%, etc.) until the end of shearing process;
vi. Once the desired final axial strain level is reached for a certain level of effective confining pressure, a new core sample has to be loaded and the subsequent effective confining pressure (200 or 600 kPa) should be preset by adjusting the cell pressure and pore pressure to the required level;

vii. Repeat the previous experimental procedures starting from step (i).

The testing setup used for absolute permeability measurement test is schematically illustrated in Figure 2.26.

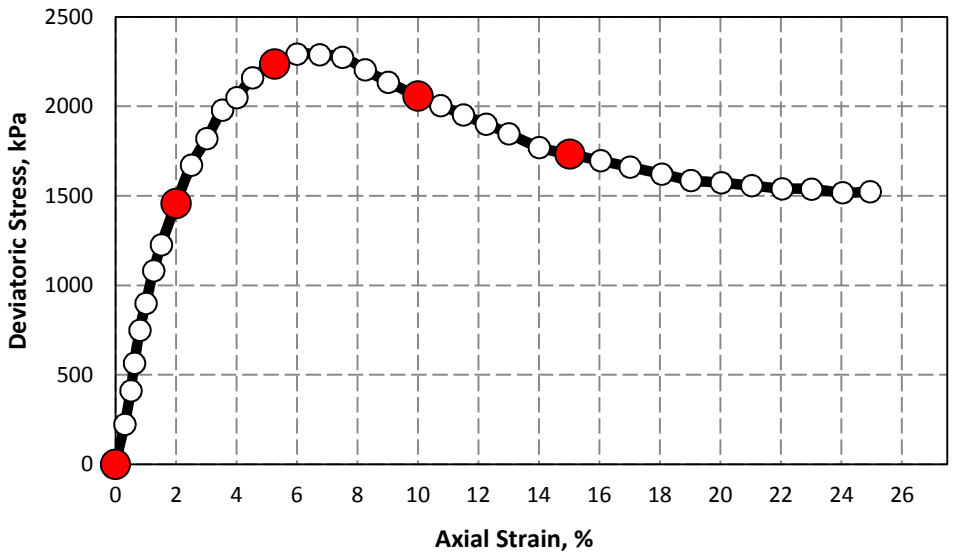

Figure 2.25 Graphical representation of five selected strain states

2.7.2 Absolute Permeability Test Procedures and Equipment

The 260-D ISCO syringe pumps, with a total capacity of 260 ml, were used to maintain a constant water flow rate, Q, through the sand specimen before and during shearing (deformation) of the sample. The pressure drop, (ΔP), across the sample was simultaneously recorded by two differential pressure transducers, manufactured by Omegadyne, connected to the top and bottom of the sample. The first transducer was placed at the inlet valve while the second one was located after the outlet of pore pressure valve (refer to Figure 2.26 for transducer locations). Before recording the pressure drop (ΔP) across the specimen, the system was allowed to stabilize so a steady reading of differential pressure could be performed. The pressure drop in the experimental setup (pressure losses associated to different lines, hooks and valves, etc.) was also accounted for during the absolute permeability calculation. Subsequently, the

net differential pressure between the top and bottom of the sample, (ΔP_{net}= $\Delta P_{across\text{-}sample}$ - $\Delta P_{apparatus}$), was implemented as input in the Darcy law equation described in Equation 2.7. It is worth to mentioning that the differential pressure, ΔP_{net}, generated across the sample during the permeability measurement tests has a minor impact on the effective confining pressure applied on the sample (i.e. The pressure drop, ΔP_{net}, measured for the three cases of effective confining pressure; 50 kPa, 200 kPa, and 600 kPa, ranged between 2 kPa and 5 kPa.).

Darcy's law:

The absolute permeability, (k_a), was estimated based on the following Darcy's law formula (Equation 2.7):

$$k_a = \frac{Q\mu L}{A\Delta P}, \quad (2.7)$$

where (k_a) is the absolute permeability of the sample, (μ) is the fluid viscosity, (A) is the cross section area of the sample, (ΔP) is the differential pressure, and (L) is the length of the sample.

The Darcy's law, expressed in previous equation, applies only for laminar flow. The flow rate used in our permeability measurement was qualified for validity based on Reynolds number, a parameter that is commonly used to delineate the laminar flow rate range from turbulent ones. The flow rate of 5 (cc/min) and 10 (cc/min) used in current experimental course yielded Reynolds numbers (Re) lower than "1". Thus, our flow rate range was in agreement with the laminar flow conditions commonly specified by geomechanics literature (i.e. to ensure a laminar flow regime in porous soil, Reynolds number should not exceed the critical value of "1" (Hassanizadeh et al., 1987)).

Another reason to limit the flow rate was to reduce the fines migration process. A higher range of flow rate, and reciprocally high flow velocity, would amplify

the fine migration into pore throats and so restrict flow through the soil. Such restrictions would yield a lower permeability values during permeability measurements tests and so affecting the accuracy of our experimental results.

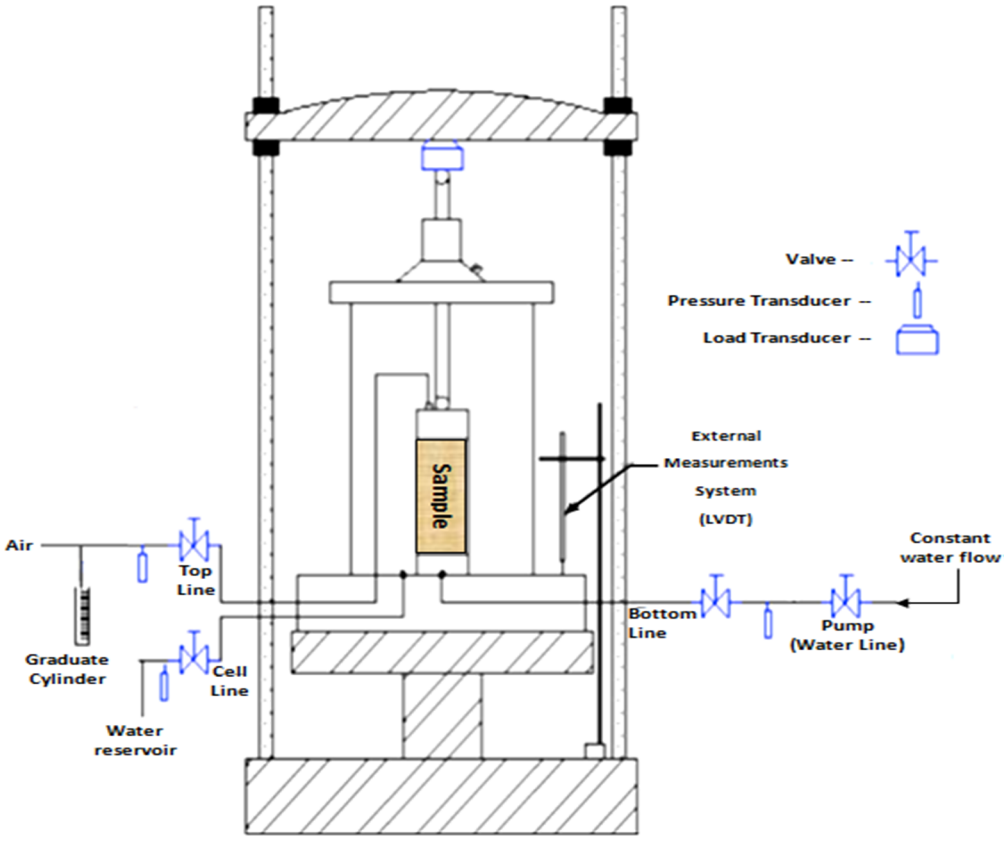

Figure 2.26 Schematic view of experimental setup

2.7.3 Porosity Calculation

Porosity is a term commonly used in soil mechanics to describe the structure of the pores volume and their extent within the sample fabrics. In geotechnical engineering the initial porosity of soil is usually expressed as a function of void ratio (e); degree of saturation (S_r); water content (W); water specific gravity (G_w); and sand specific gravity (G_s). This relationship is described in the following equation (Equation 2. 8):

$$\Phi = \frac{e}{1+e} = \frac{1}{\frac{S_r * G_W}{W * G_S}}, \quad \text{..... (2. 8)}$$

During shearing, porosity undergoes an important variation due to pore volume deformation. To cover such alteration, the new porosity values associated with each volumetric strain were calculated basing on the following equation (Equation 2.9):

$$\emptyset_n = \frac{(\varepsilon_v - \emptyset_i)}{(1-\varepsilon_v)}, \quad \text{..... (2. 9)}$$

where (ε_v) is volumetric strain, ($\emptyset_i$) is initial porosity of the sample, and ($\emptyset_n$) is new porosity corresponding to specific volumetric strain ε_v.

Equation 2.9 assumes uniform deformation of sample during shearing (i.e. regular porosity distribution along the sample). This assumption is generally violated during the triaxial compression test because of a non-uniform distribution of porosity within the specimen during shearing. Also, the porosity in Equation 2.9 represents the total porosity, (ϕ), of the sample and not the effective porosity (ϕ'). The porosity, (ϕ), value will not depict or incorporate any aspect of the inter-pores connectivity state within the sample during the shearing process.

2.7.4 Geometrical Properties of Sample, Variation and Calculation

During the shearing process, the axial strain (ε_x) was computed by dividing the specimen's change in height, ΔH, as recorded by the external transducer (LVDT), by its initial height, H_o:

$$\varepsilon_x = \frac{\Delta H}{H_o}, \quad \text{..... (2. 10)}$$

The cross-area of specimen experiences also an important variation during shearing. Thus, the new across-area of specimen should be systematically calculated at each axial strain level by the following equation (Equation 2.11):

$$A_{Corr} = \frac{V_o(1-\varepsilon_v)}{H_O(1-\varepsilon_x)}, \quad (2.\ 11)$$

where (A_{Corr}) is the new specimen cross-area induced from a given axial load, (V_o) is initial volume of the specimen, (H_o) is the initial height of the specimen, (ε_x) is the axial strain expressed in decimal, and (ε_v) is the volumetric strain expressed also in decimal.

Volumetric Strain Calculation

The volumetric strain is a crucial parameter usually used in geomechanics to describe the deformation nature (expansion or contraction) of the specimen during shearing. Assuming elastic deformation, volumetric strain is commonly expressed as the sum of the three principal normal strains ε_{xx}, ε_{yy}, and ε_{zz} respectively corresponding to normal strain in the x-direction, normal strain in the y-direction, and normal strain in the z-direction.

$$\varepsilon_v = \varepsilon_{xx} + \varepsilon_{yy} + \varepsilon_{zz}, \quad (2.\ 12)$$

From an experimental perspective, the volumetric strain variation is usually determined by quantifying the volume of water drained out or in from/to the specimen during shearing. In this study, such quantification was achieved by means of an external volume change device (Figure 2.6). Thus the volumetric strain was simply computed by dividing the specimen's change in volume, (ΔV), as recorded by the external volume change device, by its initial volume, (V_O):

$$\varepsilon_v = \frac{\Delta V}{V_o}, \quad (2.\ 13)$$

2.7.5 Isotropic Unloading Test

While the isotropic unloading test has similar initial steps to the triaxial compression test procedure, explained above, the main isotropic unloading test stage is conducted by decreasing the mean or isotropic effective stress in

contrast to the triaxial compression tests where axial loading of the sample results in an increase in the mean effective stress. The test was conducted by gradually reducing the cell pressure while keeping the pore pressure constant to establish the different effective confining pressures of 800 kPa, 600 kPa, 200 kPa, and 50 kPa (Figure 2.27).

The isotropic unloading test was mainly intended to simulate the pore pressure increase resulting from an eventual steam injection in the reservoir and subsequently evaluate its effects on the soil intrinsic properties. Thus, the permeability measurement tests were achieved at the different effective confining stresses applied (800 kPa, 600 kPa, 200 kPa, and 50 kPa) and subsequently the correlation between the induced permeability variation and effective confining stress change was developed.

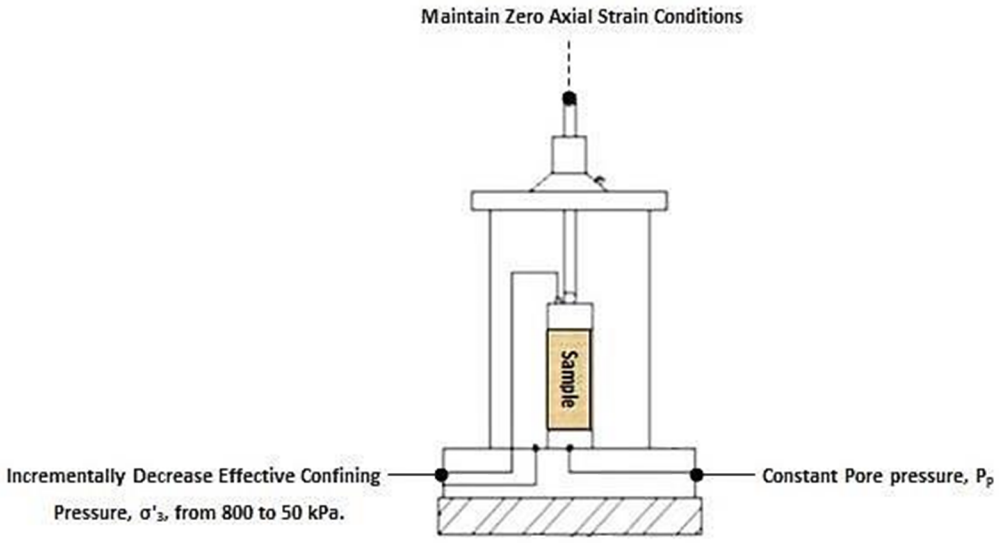

Figure 2.27 Graphical representation of sample during isotropic unloading test

3 Chapter 3 Results and Discussion

3.1 Sand Morphology

Soil classification is universal methodology intended to group soils of similar behavior and characteristics under same family based on precise rational ways and standards (e.g. Unified Soil Classification System (USCS), The Canadian System of *S*oil Classification (CSSC), etc.). Sieve analysis, which procedures were described in Chapter 2.3, is a common technique typically recommended by the Unified Soil Classification System (USCS) standards to assess particle size distribution of the soils. Table 3.1 shows the main results obtained from the sieve analysis experiments of the sand utilized in this experimental program.

Table 3.1 Sieves analysis results

Sieves N^{o}	Aperture Size (mm)	Tare Weight (grs)	Tare and Dry Soil Weight (grs)	Dry Mass (grs)	Retained (%)	Cumulative Retained (%)	Passing (%)
10	2.000	443.7	443.7	0.00	0.00	0.00	100.00
20	0.850	380.3	380.5	0.20	0.01	0.01	99.99
40	0.425	351.5	631.8	280.3	17.53	17.54	82.5
80	0.180	316.1	1624.5	1308.4	81.84	99.38	0.62
100	0.149	264.4	271.7	7.30	0.46	99.84	0.16
120	0.125	308.6	310.5	1.90	0.12	99.96	0.04
140	0.106	301.8	302.2	0.40	0.03	99.98	0.02
Pan		370.2	370.5	0.30	0.02	100.00	
			Total Mass of Soil	1599			

Figure 3.1 showed that the sand is homogenous with grains of similar size and shape, with an average grain size (D_{50}) of 390 µm. The uniformity coefficients, (C_u) and (C_C), were subsequently computed and were equal to 1.6 and 0.72, respectively, indicating that the sand would be classified as uniform poorly graded sand (USP) based on the (USCS) and (CSSC) standards. The density index, (D_r), was also determined to provide quantitative representation of the compaction degree of the reconstituted samples. The relative density index

analysis revealed that the sand test specimens could be described as very dense sand (Table 3.2) according to N. Sivakugan (2000) criteria (Dr>85) (Figure 2.8).

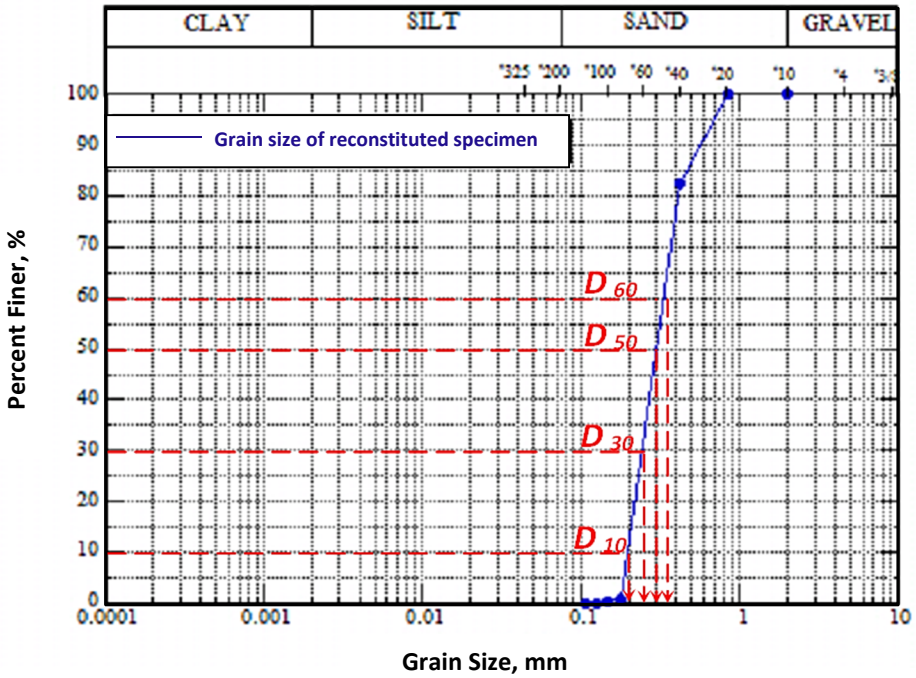

Figure 3.1 Sieves analysis curve

Particle shape is often of critical importance to the way the granular material responds during loading. The geomechanical behavior of soil may vary considerably based on changes in the geometrical form of its grain. Therefore, the particle shape of granular soils should be investigated even in soils of similar classification. Optical and scanning electron microscopy (SEM) was used to observe the inter-granular fabrics of our sand. The resulting images display a moderately interlocked texture characterized by a relatively high incidence of long and tangential grain contacts (Figures 3.3a and 3.3b). Generally, our sand is mainly composed of sub-rounded grains characterized by its medium sphericity (Figures 3.2 and 3.3) with mean grain size of 350 microns and standard deviation to mean grain size ratio of approximately of 0.428 (Table 3.3). The moderately interlocked granular texture and grains round shape are the most distinctive features of the beach sand used in this study.

Table 3.2 Pertinent void ratio and relative density obtained for our sample sand

Minimal Void Ratio (e_{min})	Maximum Void Ratio (e_{max})	Relative Density $(D_r)_{average}$ (%)
0.568	0.791	114

Table 3.3 Standard deviation and mean grain size of the sand in microns (based on Douglas (1952) equations)

STDV $(\frac{P84-P16}{2})$	MEAN $(\frac{P84+P16}{2})$	STDV/MEAN
150	350	0.428

The angularity of grains usually supports the interlocking aspect within the soil and thus improves its stiffness and dilatancy. As such, grains with high sphericity, as the case of the sand used in this research, will usually depict weaker behavior compared to angular-grain soils (Yaich 2008). The grains of the McMurray Formation represent a good instance of such type of sand with highly angular grains. Morphological comparison between the McMurray Formation sand and the sand used in the current study is depicted in Figures 3.4a and 3.4b. As can be seen, packing degree and interlocking aspect between grains is more important in McMurray sand.

As shown in the X-ray spectrum (Figure 3.5), the test sand grains are typically homogeneous and predominantly consisted of hard minerals mainly quartz and feldspar. The mineral component breakdown depicted on X-ray image shows that the test sand grains are mainly composed of Silica (SiO_2), Gold (Au) and a few traces of ductile components as feldspar clay (k). The mineral compositions (low content of clay (k)) as well as the granular texture (moderately interlocked structure) encourage more elastic than plastic mechanisms in the soil during shearing, which will likely mean the test samples will deform elastically during our triaxial compression tests. Such observation was confirmed by our

specimens' behavior in the experimental program. In general, the sample responses during shearing were consistent with soil morphological and mineralogical properties interpreted from CT-scan and X-ray graphs.

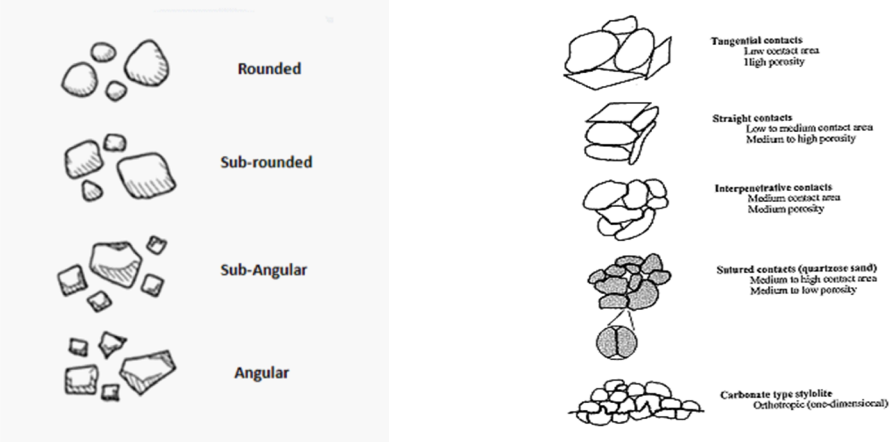

Figure 3.2 Sand classification based on grain shape and inter-granular contact types (Modified from Dusseault, 1977)

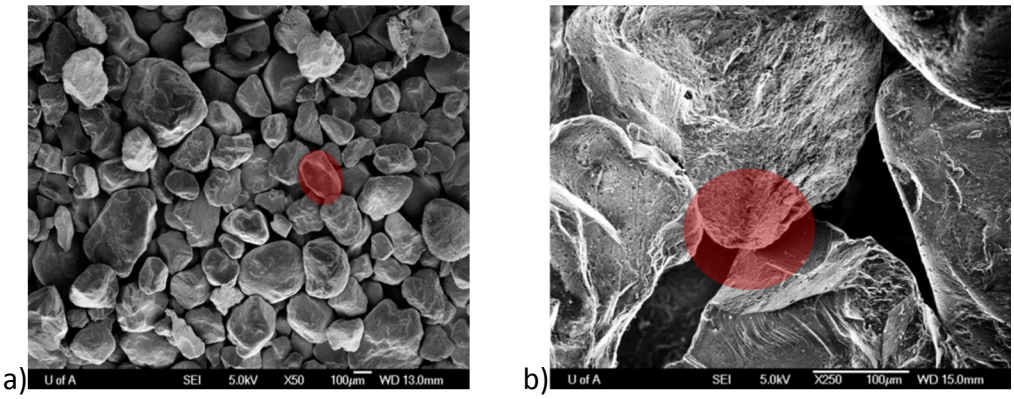

Figure 3.3 CT-Scans of sample sand showing: a) grain shape and b) grain-to-grain point contacts

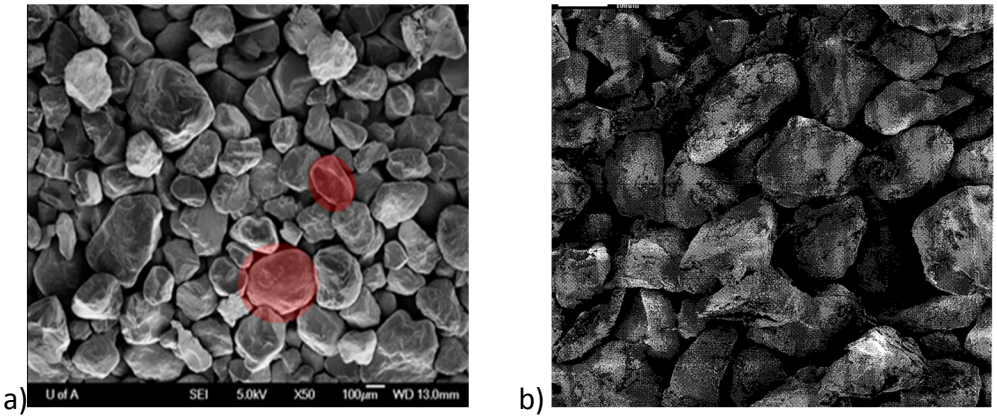

Figure 3.4 Morphological comparison between the beach sand used in this study and McMurray formation sand: a) scanning electron microscope of our sample sand, b) Scanning electron microscope of bitumen-free McMurray Formation oil sand (Touhidi Baghini 1998)

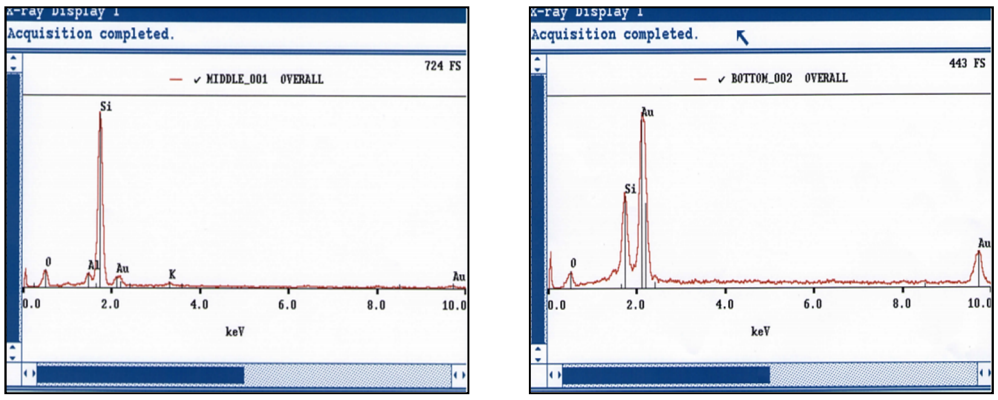

Figure 3.5 X-ray spectrums for the bottom and middle sections of our sample

3.2 Geotechnical Proprieties of the Reconstituted Specimens

The porosity of thirty-one (31) core samples and other geotechnical parameters such as void ratio (e), and water content (w_n) are summarized in the Table 3.4. The average porosity of all specimens ranged between 31-34 %.

Table 3.4 Geotechnical properties of reconstituted specimens

Samples	Bulk Volume V_b (cc)	Air Dry Sand Mass (grm)	Saturated Sand Mass (grm)	Specific Gravity (G_s)	Water Content (%)	Porosity ϕ (%)	Void ratio e
Sample 1	109.102	178.48	213.66	2.71	20%	32.25	0.475
Sample 2	107.330	178.48	214.46		20%	32.245	0.475
Sample 3	107.075	178.48	214.46		20%	33.522	0.504
Sample 4	110.224	178.48	213		19%	33.602	0.506
Sample 5	107.912	178.48	212.28		19%	31.317	0.455
Sample 6	107.673	178.48	213.3		20%	31.321	0.456
Sample 7	108.114	178.48	213.29		20%	32.338	0.477
Sample 8	114.886	178.48	212.59		19%	32.197	0.474
Sample 9	108.748	178.48	213.84		20%	29.690	0.422
Sample 10	108.221	178.48	213.67		20%	32.515	0.481
Sample 11	108.284	178.48	213.75		20%	32.516	0.481
Sample 12	109.448	178.48	214.08		20%	32.571	0.483
Sample 13	107.757	178.48	213.87		20%	32.526	0.482
Sample 14	108.698	178.48	214.47		20%	32.842	0.489
Sample 15	108.503	178.48	214.85		20%	33.109	0.494
Sample 16	108.313	178.48	212.91		19%	33.519	0.504
Sample 17	109.272	178.48	212.72		19%	31.787	0.466
Sample 18	108.235	178.48	214.1		20%	31.334	0.456
Sample 19	108.071	178.48	213		19%	32.9096	0.490
Sample 20	109.101	178.48	212.91		19%	31.941	0.469
Sample 21	108.314	178.48	212.95		19%	31.557	0.461
Sample 22	108.420	178.48	214.19		20%	31.8241	0.466
Sample 23	110.971	178.48	214.26		20%	32.936	0.491
Sample 24	109.212	178.48	213.89		20%	32.242	0.475
Sample 25	108.996	178.48	213.57		20%	32.422	0.479
Sample 26	108.015	178.48	214.38		20%	32.193	0.474
Sample 27	108.625	178.48	212.93		19%	33.235	0.497
Sample 28	107.999	178.48	213.96		20%	31.7143	0.464
Sample 29	108.740	178.48	215.39		21%	32.851	0.489
Sample 30	107.581	178.48	214.05		20%	33.943	0.513
Sample 31	108.480	178.48	215.5		21%	33.063	0.493

3.3 Initial Permeability of Samples

This section is intended to provide a qualitative and quantitative evaluation of the initial absolute permeability of the test samples and their dependence on the main intrinsic properties of the soil. A graphical presentation of experimental data revealed a strong correlation between the measured absolute permeability of samples and its corresponding porosity. As shown in Figure 3.6, higher permeability values were invariably associated to high value of initial porosities. Such observation is confirmed by the linear tendency of the trend line depicted in Figure 3.6.

Several mathematical correlations have been provided in the literature to estimate absolute permeability starting from petrophysical characteristics of samples, mainly its porosity and grain morphology. First attempt was achieved by Carman-Kozeny (1937) through the mathematical model explained in following equation (Equation 3.1):

$$k = CD^2 \frac{\emptyset^3}{(1-\emptyset)^2}, \quad (3.1)$$

where $(\emptyset)$ is the initial porosity, (D) is the grain mean diameter in microns, and (C) is a constant usually determined from experimental data.

Subsequently, a generalized form of Carman-Kozeny (1937) equation was presented by Rajani (1988). Rajani (1988) proposed a general model for describing the variation of permeability with porosity and mean grain size for unconsolidated sand in which permeability is typically given by the following equation:

$$k = CD^2 \frac{\emptyset^a}{(1-\emptyset)^b}, \quad (3.2)$$

where $(\emptyset)$ is the initial porosity, (D) is the mean diameter in microns, (a), (b), and (C) are constants determined from experimental data.

Similar to Kozeny-Carman (1937) model, the constant (C) was also proposed by Rajani (1988) to incorporate the influence of the soil morphology and the geometrical shape of porous media on the initial absolute permeability of the sand. It is noted that by respectively substituting (a) and (b) by 3 and 2, Rajani (1988) equation will integrally lead to the Kozeny-Carman equation. Using the prescribed constant of (C) equal to (1/180) suggested by Rajani (1998) for uniform spherical particles, the predicted values using Equation 3.2 were found to overestimate permeability as compared with the measured data. Therefore, a nonlinear least-square curve fitting was initiated to find the coefficients of

Carman-Kozeny and Rajani equations that fit better the laboratory data. As shown in Figure 3.6, the estimated initial permeabilities seem to correlate strongly to the measured permeability values with a reasonable degree of accuracy (± 0.20). The results illustrate in Figure 3.6 show that the Rajani (1988) equation could provide a reasonable qualitative estimation of absolute permeability of samples basing on initial porosity and grain mean diameter of the sand. Value of the empirical constant should be carefully calibrated to account for non-uniform angular particles.

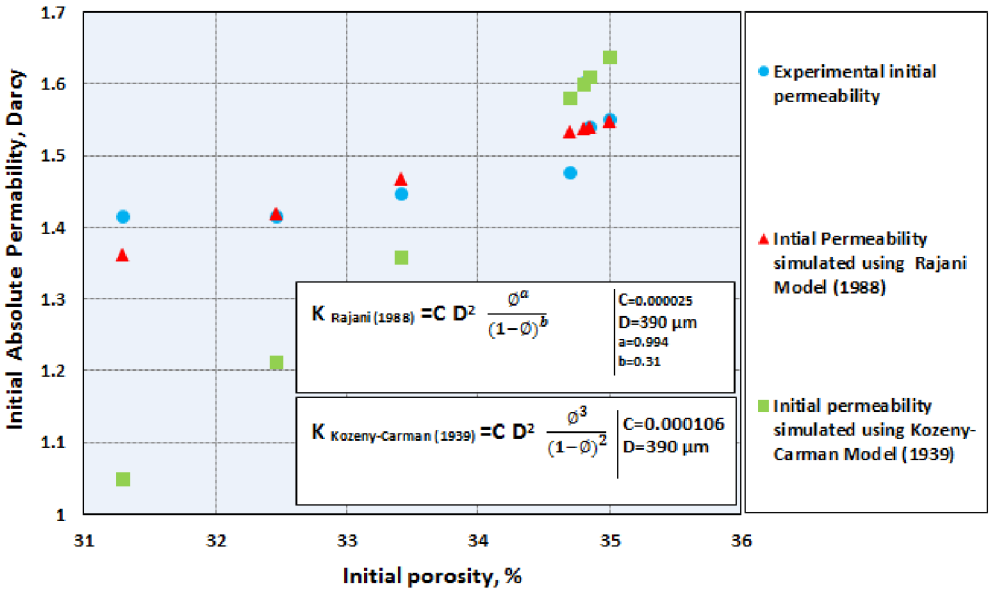

Figure 3.6 Estimation of absolute permeability from empirical correlations

3.4 Stress-Strain Behavior

Throughout this study, the assessment of soil stiffness was achieved by evaluating the corresponding behavior of specimens during compression tests performed under three ranges of confining stress: 50 kPa, 200 kPa, and 600 kPa, considered as representative of the stress states present within the shallow oil sand reservoirs (Figure 3.7).

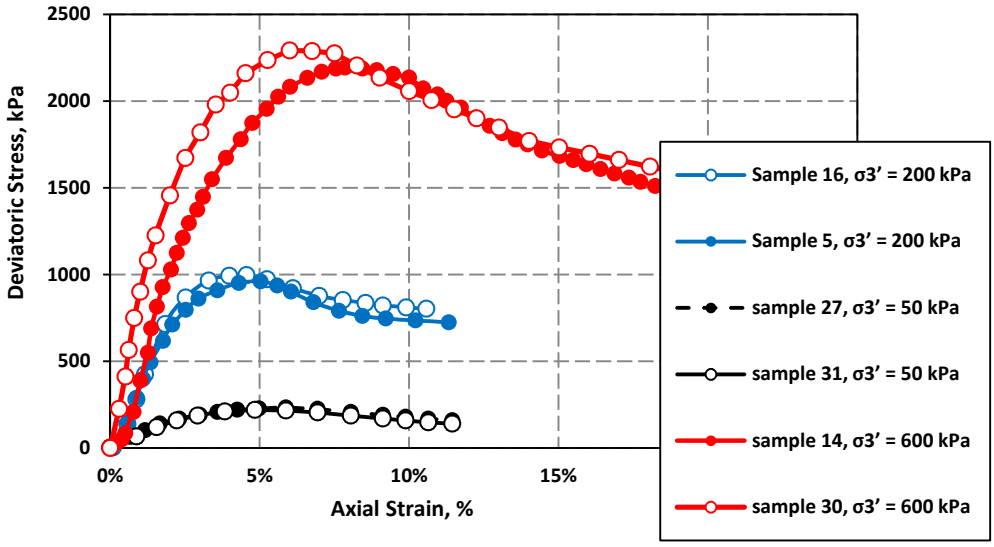

Figure 3.7 Stress-axial strain of specimens at different effective confining stresses of 50 kPa, 200 kPa and 600 kPa

The stress-deformation curves, shown in Figure 3.7, were obtained by a sustained increase of the axial load while maintaining the confining pressure constant and by simultaneously recording the differential stresses and resulting deformation in the axial direction of the sample. As can be seen, all the compression triaxial experiments yielded a similar shape of stress-strain curves, roughly depicting the typical stress-strain of sand stone behavior. Each of previous curves could be generically divided to four parts based on its shape trend, (Figure 3.8):

1. A semi-linear part which is due to seating adjustments between the end caps and the sample,
2. A linear part delineating the elastic deformation phase ($\varepsilon_{elastic}$) followed by,
3. A non-linear part preceding the failure peak that is representing the viscous deformation, a combination of elastic and plastic deformation ($\varepsilon_{elastic} + \varepsilon_{plastic}$); and finally
4. A typical shape strain-softening of post-failure deformation.

It is to note that the semi or imperfect linearity of the pre-elastic and pre-yield parts of the curve implies more the visco-elastic (compactive) than the purely elastic nature of the sand specimens.

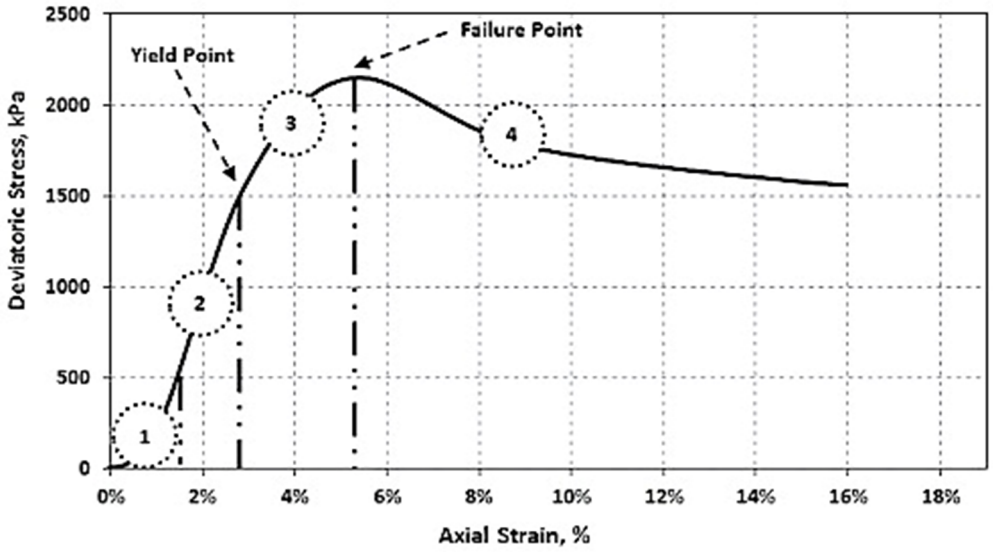

Figure 3.8 Typical stress-strain curve of sand stone: 1. pre-elastic non-linear phase; 2. linear-elastic-phase; 3. pre-failure phase (plastic tendency and 4. failure and post-failure phases

The shape of the stress-strain curves, shown in Figure 3.8, can provide some valuable clues regarding the key mechanisms involved in the shearing process of the sample. Geomechanics factors driving the soil deformation within each section of the stress-strain curve are discussed below.

- Pre-Elastic Non Linear Phase: During the early stage of loading, the sample behavior is mainly governed by the seating load issue. As such, there is always a period of "adjustment" before the axial load is completely and uniformly applied to the ends of the specimens. This period of adjustment was manifested in form of non-linear shape in the stress-strain curve of the sample.

- Linear-Elastic-Phase**:** When applied stress increases, the inter-granular space diminish resulting in less opportunity for grain to freely slip and rotate, making the inter-grain surface of contact greater. Therefore, most of the axial load becomes directly taken up by the hard component of sand (quartz grain). This latter process is usually known as the quartz-on-quartz Hertzian contact elasticity process (Peter Schutjens 2004), which is the direct contributor to triggering the apparent elastic deformation in the sample. Over the elastic domain, most deformation is recovered upon reloading along the same stress path, except strains induced from crack closure. The elastic deformation is usually demarcated in form of tilted line in the stress strain curve with a characteristic slope, commonly known as Modulus of Elasticity, (E), or Young's Modulus, a geomechanical parameter relating rock resistance to deformation. Young's Modulus value is geometrically obtained by drawing a secant line to the linear part of stress strain curve, and then evaluating the slope of the obtained secant. The computed slope value is known as elastic Modulus, (E). It has a unit of force per area (i.e. Pascal according to the SI system).
- Pre-Failure Phase (Plastic tendency): With excessive stress, sample starts loosing elasticity; the resulting strain arises due to a combination of elastic and inelastic deformation, with the relative contribution of inelastic deformation increasing with stress and becoming persistent and dominant over elastic deformation at and beyond the ("yield point"), see Figure 3.8. The yield point is often defined as the onset of nonlinear behavior in the stress-strain curve and interpreted as an increase in the activity of inelastic deformation mechanisms which could be either a time-dependent, often referred to as viscous, or time-independent known as plastic. The relative importance of elastic and inelastic deformation mechanisms during compaction depends on many factors, mainly including sample microstructure, grain shape, porosity, pore pressure, and temperature. Once

the yield point is passed some fraction of the deformation will be permanent and non-reversible. Note that inelastic (or plastic) mechanisms are usually associated with an apparent dilation and significant permeability changes in the sample.

- Failure Phase**:** With increasing axial stress, sample hardening continues to some maximum value of deviatoric stress, before yielding in shear at the failure point, Figure 3.8. Shear fractures are usually result from stress that tend to slide one part of the specimen past an adjacent part, and when the sample finally breaks, the two walls may slide past one another. The arrangement and form of the shear planes depend upon several factors including homogeneity, isotropy, and fabric of the rock. Within cohesionless soil, fractures are not usually apparent and typically manifested in form of discrete micro-crack and/or shear bands with high porosity zones. Ultimately, hardening ceases and the sample starts to soften as stress is increased further. This is demonstrated by obvious deviatoric stress drop after stress peaks. The decrease in stress then stabilizes and the curve starts to flatten after 18 % of axial strain. The total failure is generally associated to the full development of shear bands across the whole sample (Desrues and Vigianni 2004). In this regard, Desrues (2004) have concluded that sand failure is predominatly related to shear bands development all over and within the intergranular space of the sample. Shear banding is usually characterized by the appearance of localized zones of high porosities along the sample boundaries. With increasing axial load, shear-bands start to simultaneously expand and extend from the boundaries toward sample core, and such, induces a significant increase of inelastic mechanisms activity, mainly including micro-crack formation and grain sliding and rotation within the inter-granular space. CT images of failed sand packs (Wong 2004) are shown in Figure 3.9. These images illustrate the evolution of shear band during the deformation process. The present shear bands, usually known as

deformation bands, are mainly localized tabular zones with few millimeters of thickness that expands with increasing stress. Based on extensive stereophotogrammetry analysis, Desrues (2004) observed that the shear banding process usually initiates just before reaching the total collapse (i.e. the deviatoric stress peak) of the sample. In this context, it is difficult to delineate the beginning of the shearing bands development at any point on the stress-strain curve obtained in this study. However, the strong correlation between the changes in deformation trend, from elastic to viscous behavior, during the pre-yield phase seems to be an index of shear bands influence on the compaction/deformation process. It is more likely that shear-banding onset coincides with the elastic limit (yield stress) on the stress-strain curve. This observation is in line with previous results found by Li et al. (2003). As described in Figure 3.9, the shear bands onset perfectly coincides with the yield stress point, just before the start of pre-failure phase of the stress-strain curve.

- Post-Failure Phase**:** Post-failure deformations are usually manifested as micro to intermediate fractured–zone in which thickness varies in space and time along the fracture zone. These fractures are usually associated to an important volume gain (dilation) by the soil. The dilation onset of soil usually occurs before stress-peak, typically with the start of the inelastic mechanisms development at yield point, and gets more pronounced beyond failure and with increasing stress. Following failure, the average inter-granular stress continues to monotonically increase. Consequently, with an excessive stress, the sample undergoes an important pore collapse that is usually associated with grain size reduction (cataclasis) due to crushing and compaction. In this study, indications of grain crushing were noticed in samples that had experienced a high level of axial straining typically above 30%, see Figure 3.10.

The sandstone reservoirs are commonly divided in three categories depending on the nature of deformation taking place within the reservoir:

1. Reservoir at near elastic deformation in which inelastic deformation represent typically less than 20% of the total strain at a given stress,
2. Reservoir at inelastic deformation state in which inelastic deformation is dominant over elastic deformation. At this state, reservoirs usually manifest an important variation in permeability and pore volume with the increasing of the inelastic mechanisms activity,
3. Reservoir at or nearby failure state in which there is a high probability that reservoir fails by shear localization or/and pervasive pore collapse.

Any of previous reservoir state can be reached either by deploying an invasive artificial recovery technique such SAGD or naturally due constraints resulted from reservoir depletion. It is important to mention that the nature of deformation is highly dependent on the stress state within the reservoir.

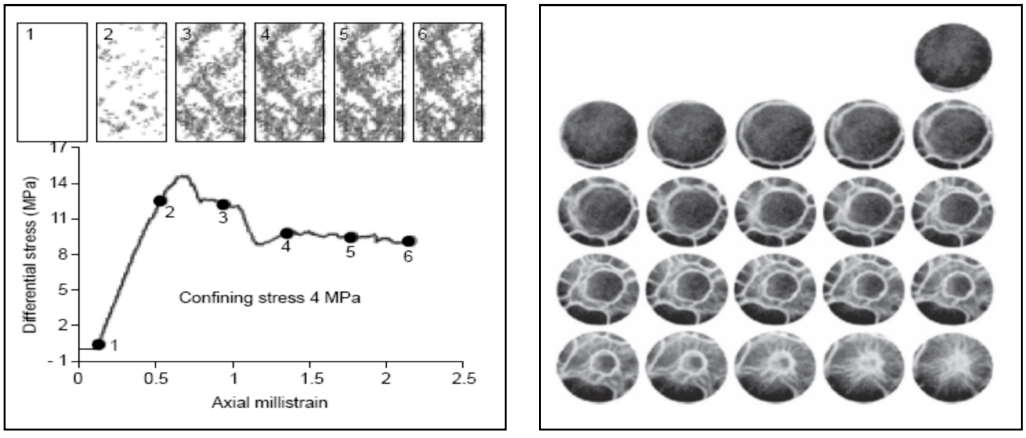

Figure 3.9 CT-images of failed sand packs obtained by Wong (2004)

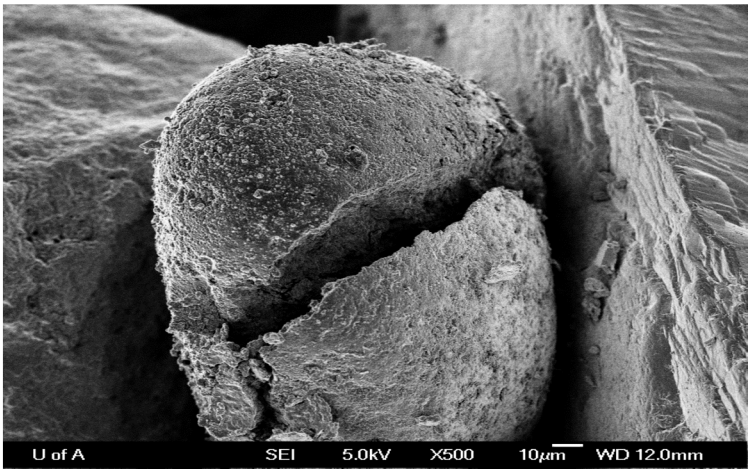

Figure 3.10 CT-scan photograph of a crushed grain (Sample 30, 600 kPa case)

3.4.1 Correction of Cross-Sectional Area of the Sample during Triaxial Compression Tests

During triaxial tests, the cross-sectional area of the sample experiences a visible expansion due to the volumetric strains achieved in our experiments. Differential stress values were adjusted by taking into consideration this area change.

Figure 3.11 depicts two curves of stress-strain; the first curve was generated by taking the corresponding area change into account and the second by assuming a constant cross-sectional area. The constant-section curve displays an apparent hardness after stress peak. This apparent strain-hardening behavior disappears in the second curve and the post-peak looks more perfectly plastic at a higher strain.

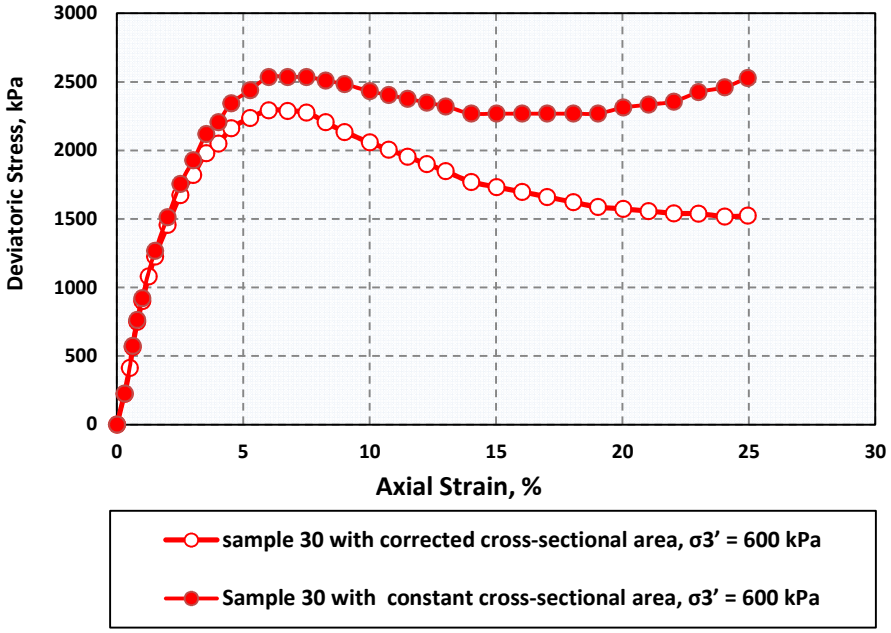

Figure 3.11 Impact of correcting the stress-strain curve for changes in the sample cross-sectional area in a triaxial compression with 600 kPa effective confining stress

3.4.2 Stiffness of Soil Sensitivity to Effective Confining Stress

Our sand samples have little to no cementation. As such, their strength is entirely derived from grain-to-grain contacts, which are essentially maintained by the effective confining stress applied on the soil. In general, the confining stress plays an opposing factor to grain rotation/slippage by tidily maintaining the granular matrix of the soil during shearing. Consequently, any increase in the effective confining stress will eventually result in a gain in strength by the soil (i.e. higher stress peaks, higher residual strength, and higher elastic modulus). This behavior was seen in the tests conducted for this study.

As shown in Figure 3.7, the maximum shear strength of the sample shows an increase of trend with an increase of effective confining pressure: the higher the effective confining pressure, the sample is subjected to, the higher the deviatoric

stress peak. This observation is also consistent with residual strength upon yield, which demonstrates a strength dependency on effective confining pressure.

Young's Modulus was obtained, for each stress-strain curve, by drawing a tangent line between 1% and 2% of axial strain, Figure 3.12. Likewise for peak stress, Young's Modulus, also known as elastic modulus (E), demonstrates an important dependency on confining pressure. As shown in Figure 3.13, higher values of Young's Modulus are associated with higher levels of confining stress.

A power function was suggested by Chalaturnyk (1996) to describe the variation in modulus of elasticity, (E), observed in his samples in response to an eventual change in effective confining stress, (σ'_3), (Equation 3.3):

$$E = 343\sigma_3'^{0.875}, \quad \text{..... (3. 3)}$$

Chalaturnyk (1996) equation was applied on Young Modulus data obtained in this study. Results are depicted in Figure 3.13.

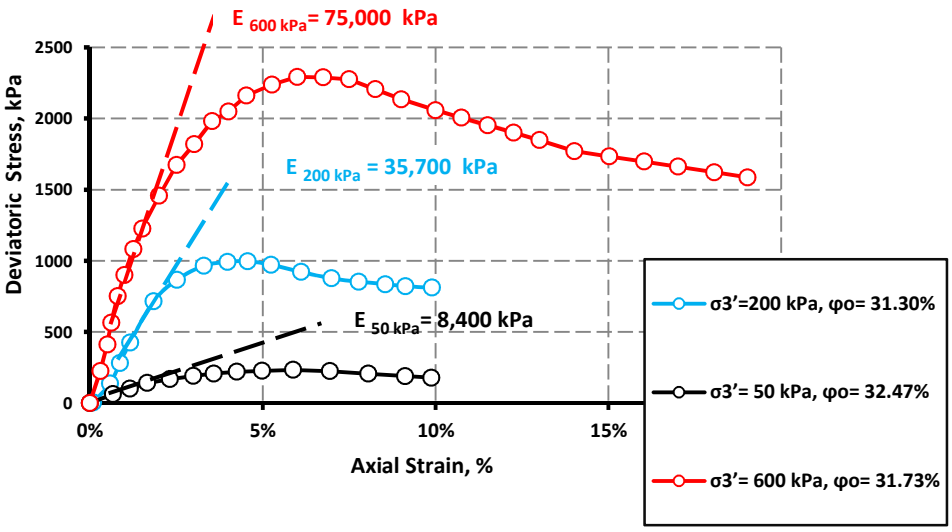

Figure 3.12 Young's Modulus (E) for different effective confining pressures: 50 kPa, 200 kPa, and 600 kPa

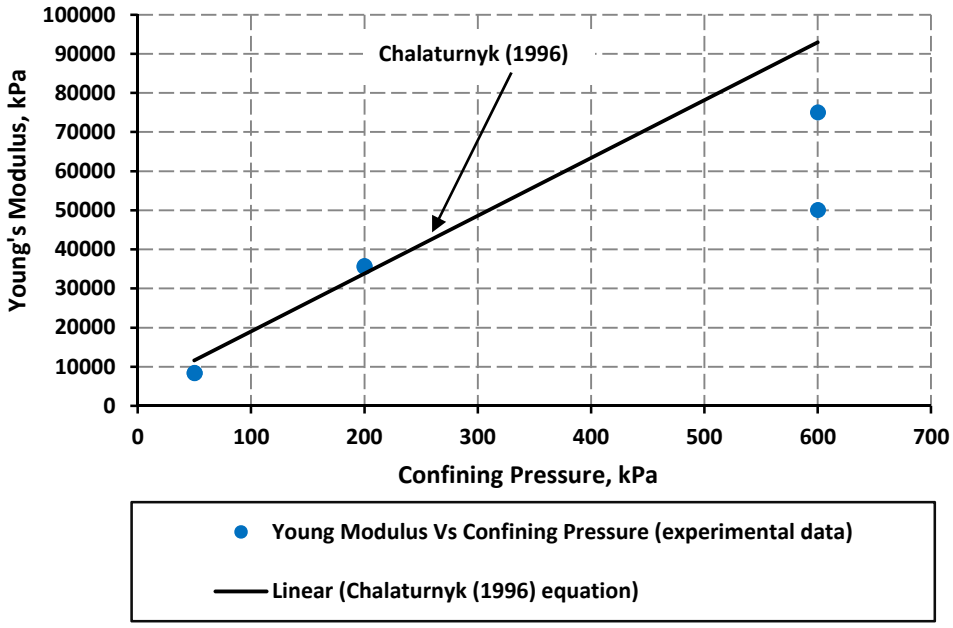

Figure 3.13 Correlation between Young Modulus (E) and effective confining stress

As can be seen in Figure 3.13, Chalaturnyk (1996) relation displays a good match for the range of confining pressure up to 200 kPa and overestimates elastic modulus after that. A difference of approximately 10,000 kPa from the experimental data was obtained in 600 kPa effective confining pressure case. This is probably due to the difference in experimental conditions and method used for calculating Young's Modulus in the triaxial test between the two studies. It is important to mention that modulus of elasticity, (E), calculated from Chalaturnyk equation is only applicable for a low range of effective confining pressure, typically less than 200 kPa. Chalaturnyk (1996) equation was not recommended by Touhidi (1998) to estimate Young's Modulus of sand soil for effective confining stresses over 250 kPa.

This inverse correlation between soil strength and effective confining pressure shown on our experimental data implies that rock response to loading, exhibited in form of elastic or plastic deformation, could strongly depend on their in situ

stress state. As such, a rock exhibiting very little plastic deformation near the ground surface could deform more plastically at depth.

3.4.3 Mohr-Coulomb Failure (Strength) Envelope

The stress path followed for each of the three effective confining pressures: 50 kPa, 200 kPa, and 600 kPa, is illustrated in Figure 3.14, where they are plotted in the **t-s'** stress field. The variables **t** and **s'** are the representative stress ratios of Mohr Circle, as defined by Equations 3.4 and 3.5:

$$\boldsymbol{s}' = \frac{(\sigma'_{1+}\sigma'_3)}{2}, \text{ and} \quad \text{..... (3.4)}$$

$$\boldsymbol{t} = \frac{(\sigma'_{1-}\sigma'_3)}{2}, \quad \text{..... (3.5)}$$

where (σ'_1) and (σ'_3) are respectively the effective axial stress and effective confining stress applied on the sample.

Shear strength is a term commonly used in soil mechanics to describe the amount of the shear stress that a soil can sustain under loading conditions. Soils derive their shear strength from two main sources: interlocking and frictional resistance between particles. In terms of effective stresses, the shear resistance is often approximated by:

$$\tau = \sigma' \tan(\varphi') + c', \quad \text{..... (3. 6)}$$

where (σ') is defined as the effective total stress applied normal to the shear plane and (φ') is the effective stress friction angle or also known as the angle of internal friction.

The friction angle is an essential parameter to evaluate the amount of interlocking among particles and consequently, the shear strength of the soils. A higher friction angle is usually an indication of a higher resistance of the soil to shearing stresses. For cohesionless soil such as the dense sand specimens used in

this research, cohesion, c', is usually assumed to be zero (c'=0). Thus, the friction (*φ'*) can be obtained by computing the slope of line connecting the peak of each stress path, designated as α, and subsequently using the geometrical relationship tanα= sin *(φ')* to determine numerical value of the friction angle (Figure 3.14).

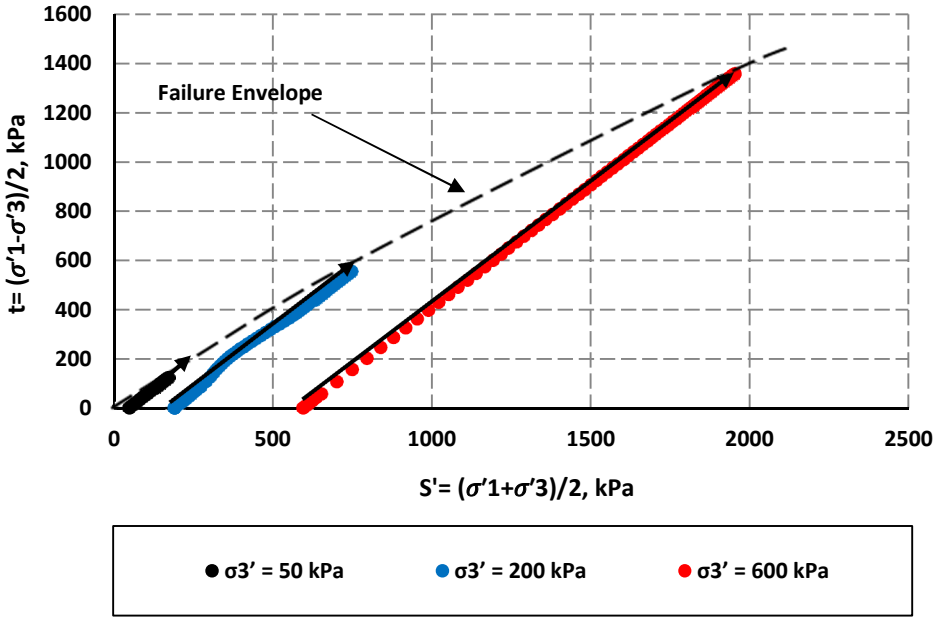

Figure 3.14 t-s' plot of three effective stress (50 kPa, 200 kPa and 600 kPa) tests

The nonlinearity of the failure envelope, plotted in Figure 3.14 suggests that shearing resistances of the sand is function of the applied confining stress. As shown, the friction angle (*φ'*) interpreted from the slope of the failure envelope is not a constant but seems to decrease with increasing confining stress (i.e. friction angle value declined from 37° to 34° for an eventual increase in confining stress from 50 kPa to 600 kPa, Figure 3.15). Previous observation is confirmed by the following logarithmic equation, usually adopted in geotechnical works (e.g. Touhidi 1998) to describe the inverse relationship between friction angle and magnitude of effective confining stress increase:

$$\varphi' = \varphi'_0 - \Delta\varphi'_0 \log\left(\frac{\sigma'_3}{p_a}\right), \quad \text{(3. 7)}$$

where (φ'_0) is the value of the friction angle at a confining pressure of 1 atmosphere and ($\Delta\ \varphi'_0$) is induced reduction in friction angle from a ten-fold increase in confining stress.

A summary of shear strength tests is depicted in Figure 3.15, where points representing the state stress at maximum effective stress ratios are plotted on the **(t-s')** stress field. Data show that the angle of shear resistance at failure of our specimen sand is varying between 37° to 34° depending on the confining pressure applied. This range of friction angles is slightly lower than shear resistance angle of 42° and 43°, respectively recorded by Oldakowski (1994) and Touhidi (1998) for their reconstituted sand samples. The slight dissimilarity between our friction angle and values found by Touhidi (1998) is mainly derived from the difference in morphology between the two sands. Touhidi employed cleaned McMurray Formation oil sand, whereas commercially available sand grains were utilized in this study. McMurray Formation sand grains are angular whereas the sand grains used in this study were well rounded.

The maximum deviatoric stresses obtained for the three effective confining pressure investigated in this study (50 kPa, 200 kPa, and 600 kPa) along with other geomechanical parameters such as (E) and axial deformation upon fail, (ε_{axial}), are summarized in Table 3.5.

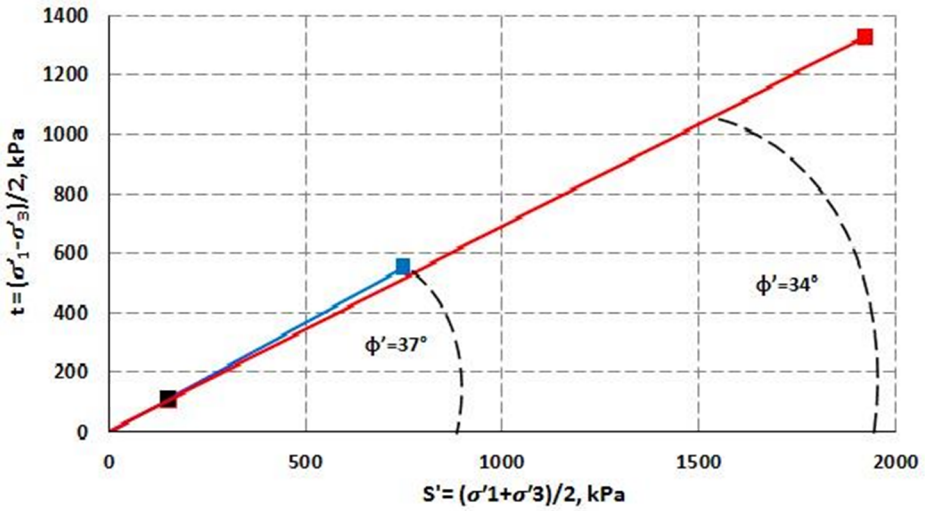

Figure 3.15 Effective friction angle (ϕ') values for three effective stresses, 50 kPa, 200 kPa and 600 kPa of Synthetic sand

Touhidi (1998) obtained a slightly higher peak stress of 1000 kPa during his 200 kPa effective confining pressure experiment. It is speculated that this difference is attributed to the dissimilarity in the initial porosity and grain morphology between the two sands (i.e. sub-rounded grain of our sand versus angular grain of Touhidi (1998) sand. This argument is in accordance with Yaich (2008) findings regarding sensitivity of soil stiffness to morphology of grains. Yaich (2008) reported that grain angularity would prompt the interlocking aspect in the granular soil and accordingly improve its resistance to shear. From this perspective, sand with rounded grain, such the case of our sand samples, would demonstrate weaker resistance and thus lower peak stress at failure. However, for his triaxial compression test conducted at 345 kPa effective confining stress, Yaich(2008) samples, made from lower fine Ottawa sand, reached a peak stress of approximatelty 1690 kPa before failing. This higher value is evidently due to the the greater effective confining stress used in his experiments.

Table 3.5 Stiffness parameters reported for each samples under the three effective confining pressures: 50 kPa, 200 kPa, and 600 kPa

Sample	(σ'_3) kPa	Porosity %	$(\sigma_1'-\sigma'_3)_{\text{upon fail}}$ kPa	$(\varepsilon_{axial})_{\text{Upon fail}}$ %	Young's Modulus kPa
Sample 14	600	33.4	2193	8	50,000
Sample 30	600	31.7	2292	6	75,000
Sample 16	200	31.3	997	5	35,750
Sample 5	200	31.7	9610	5	35,500
Sample 27	50	32.5	227	5	8,400
Sample 31	50	32.9	219	5	8,350

3.5 Volumetric Strain

Volumetric strain curves obtained from the drained triaxial compression tests are shown in Figure 3.16. The results show classic expected volumetric behavior for dense, un-cemented sands: an initial limited reduction of volume at the beginning of loading stage followed by a substantial dilation with increasing deviatoric stress. The compaction behavior that occurs at the beginning of loading is attributed to pores volume reduction (i.e. compaction) and closure of micro-cracks as a result of the compressive constraint applied. Subsequently with a sustained increase of the deviatoric stress, the induced shear distortion of the sample triggers the dilation process (development of shear bands) and an expansion of sample volume occurs.

It is important to note that volumetric strain, as used in this thesis, refers to the percent volume change of the total sample volume. From petroleum perspectives, it is more common to use pore volume strain to express volume change alteration instead of total volume strain used in this study. To convert volume strain to pore volume strain, the following relationship should be applied (Equation 3.8):

$$\left(\frac{\Delta vol}{PorVol_i}\right) = \frac{\frac{\Delta vol}{Vol_i}}{\emptyset_i}, \quad \text{..... (3. 8)}$$

where ($\frac{\Delta vol}{porVol_i}$) represents the pore volume changes; ($\frac{\Delta vol}{Vol_i}$) is the induced volumetric strain; and ($PorVol_i$), ($\emptyset_i$), (Vol_i) are respectively the initial pore volume, the initial porosity, and initial total volume of the sample.

As mentioned previously; the stress-strain curves for all three effective confining pressures used in the triaxial experiment had almost the same shape. However, a more compactive behavior and lower dilation trend was associated with higher levels of confining pressure. In general, samples under lower confining stress showed higher susceptibility to dilation as compared to higher confining pressure. As noted in Figure 3.16, the volumetric strain for the confining stress of 50 kPa achieved a maximum compaction value of (-0.29%) at the end of contraction phase before reaching a positive or dilatant volume change of 5.61% at 10% axial strain. For effective confining stresses of 200 kPa and 600 kPa, the initial contractant volumetric strain reached (-0.58)% and (-0.89)%, respectively, and at an axial strain of 10%, a positive or dilatant volume change of 3.89% and 2.34%, respectively. However, it was observed that an increase in the effective confining stress from 50 kPa to 200 kPa then 600 kPa delayed the onset of dilatancy onset from 1% at 50 kPa to almost 2% and 3% respectively for 200 kPa and 600 kPa effective confining pressure cases.

In general, our experimental results compare reasonably well with previous researches (Touhidi 1998, Yaich 2008, Khan 2009, and Hamoud 2012). For a triaxial compression test with 200 kPa effective confining pressure, Touhidi (1998) had also reported a similar geometrical shape of volumetric strain curve: an initial soil compaction of soil to record an overall volume reduction of approximately -0.5 % at 1% axial strain followed by a substantial dilation of sample to reach volume gain of 6% at 10% axial strain. Touhidi (1998) compression triaxial test was conducted on reconstituted samples of Athabasca sand with 32% initial porosity. At approximately equivalent effective confining

stresses, Figure 3.17 provides a comparison of the volumetric behavior of sand specimens.

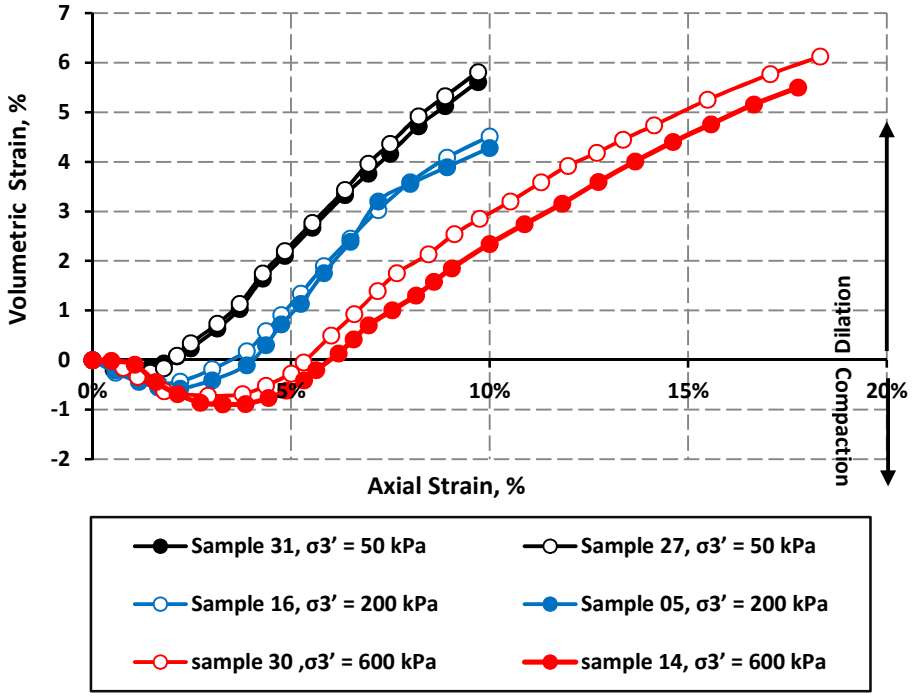

Figure 3.16 Volumetric strain curves for the three effective confining pressures: 50 kPa, 200 kPa, and 600 kPa

Similar to axial strain behavior (refer to Table 3.5), volumetric strain behavior is also sensitive to initial porosity of the samples (Figures 3.18 and 3.19). A slight difference in initial porosity may yield an important difference in volumetric behavior between samples during shearing under the same loading conditions. As shown in Figure 3.18, samples with higher initial porosity show more and longer compactive behavior while sample with lower initial porosity show more dilatancy.

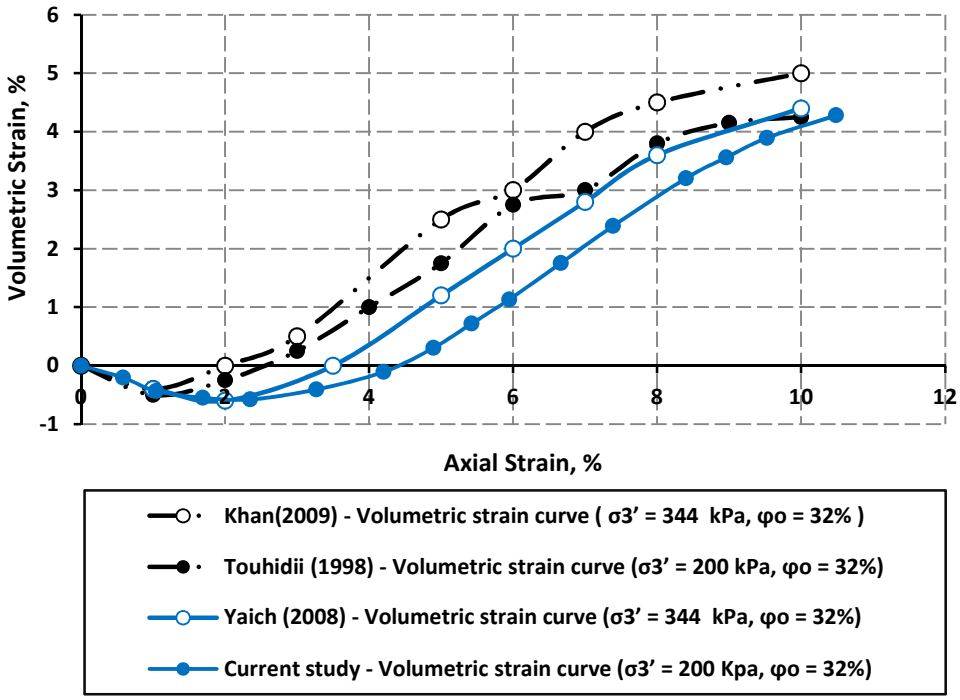

Figure 3.17 Experimental finding of previous researchers (Touhidi 1998, Yaich 2008, and Khan 2009)

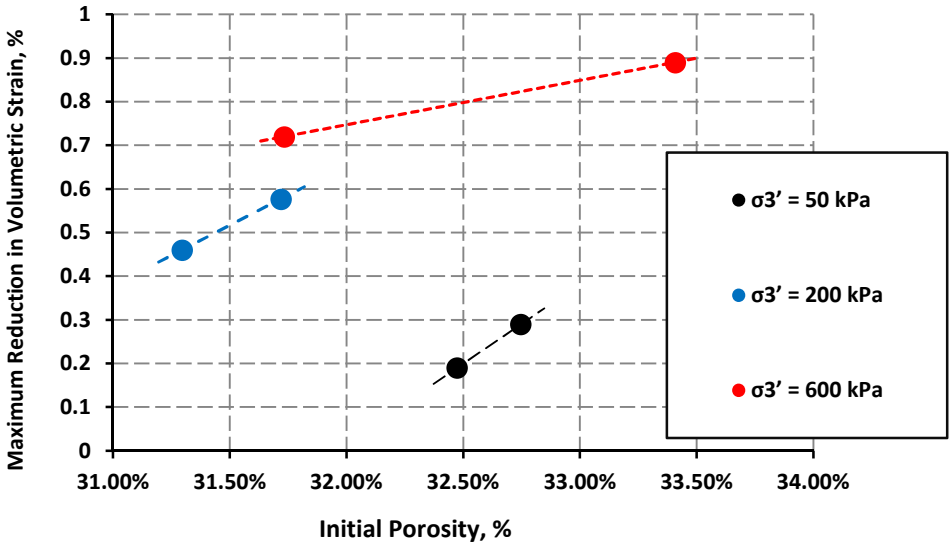

Figure 3.18 Maximum volumetric strain reductions reported for the three effective confining pressures: 50 kPa, 200 kPa, and 600 kPa

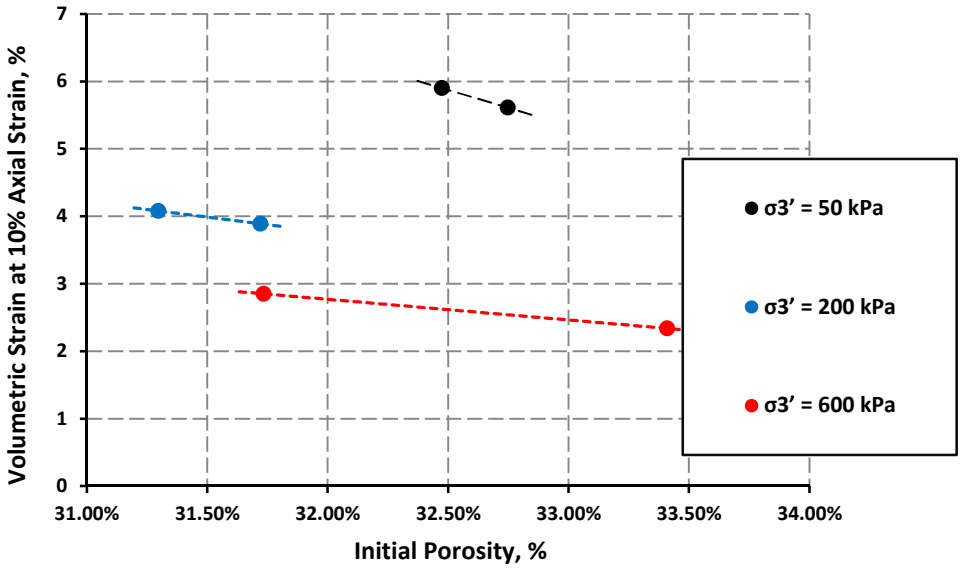

Figure 3.19 Maximum dilations reported for the three effective confining pressures: 50 kPa, 200 kPa, and 600 kPa.

3.5.1 Volumetric Strain Sensitivity to Effective Confining Pressure

Confining stress is recognized as the main opposing factor to the free slippage and sliding of grains within the sample grains matrix. Higher range of confining stress will significantly inhibit sample dilation due to the more important restrictions applied on grain motion in lateral direction. This observation was confirmed by the experimental data presented in Table 3.6. Actually, the volumetric strain, (ε_v), of our sample depicted an important sensitivity to applied confining pressure. In general, samples loaded under higher confining stress showed more important compaction behavior and lower dilatancy trend in comparison to sample loaded under lower range of confining stresses.

To understand volume response in geomechanics perspectives, it would be more convenient to make reference to the stress state present in the sample during shearing. During the triaxial test, it is commonly recognized that the volume response of the sample is primarily controlled by two main stress components: principal mean effective stress (Equation 1.1), responsible for the

compaction or contraction of the sample, and diffirential (deviatoric) stress (Equation 1.2) which is the main controlling factor of soil distortion. Indeed, the increments of the axial stress during shearing will induce a simultaneous increase in both components of the shear stress with a relative influence that continously changes with the increase of axial constraint. Over the early stage of axial loading, the mean effective stress is the dominant component in the stress state present within the sample. Thus, a porous volume reduction occurs and a total contraction of the sample is induced. With an increase of axial stress, the sample starts showing some dilation and the stress state becomes more a combination of both mean principal effective stress and effective devioatoric stress, with the relative contribution of devioatoric stress increasing with the incremental rise of axial stress to become persistent and dominant over mean principal effective stress at and beyond dilation onset. With the rising of axial load, dilation due to sample distortion starts exceeding the contraction process and hence soil begins displaying a net increase in volume. The dilation caused by deviatoric stress becomes especially pronounced when stress conditions are approaching their state of failure. Near failure, dilatancy rate become notably higher and the volumetric strain curve demonstrated a higher rate of change compared to the beginning of dilation process. These observations are illustrated in Figures 3.20, 3.21, 3.22, and 3.23.

Table 3.6 Experimental data reported for the three effective confining pressures: 50 kPa, 200 kPa, and 600 kPa

(σ'_3) kPa	$(\sigma_1'-\sigma'_3)_{Upon\ fail}$ kPa	Young's modulus (E) kPa	Compaction Peak %	$(\varepsilon_v)_{10\%\ Axial\ Strain}$ %
600	2193	75,000	0.890	6
200	998	35,700	0.460	4
50	227	8,400	0.190	2

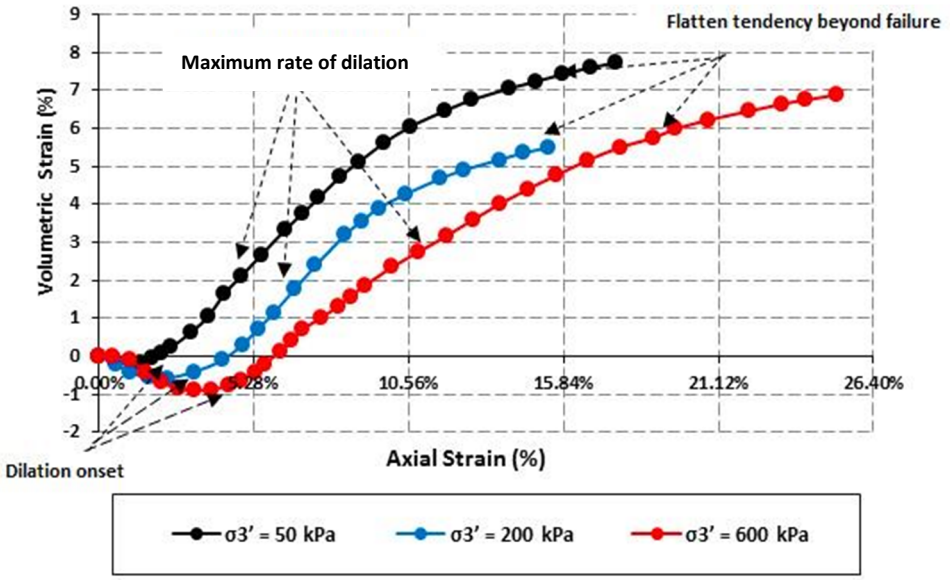

Figure 3.20 Volumetric strain curves for the three effective confining pressures: 50 kPa, 200 kPa, and 600 kPa

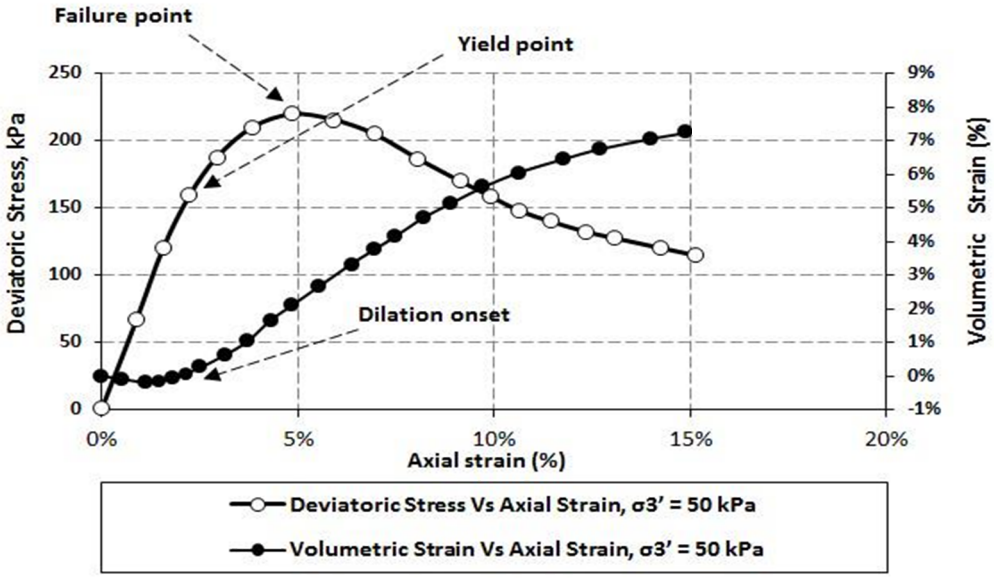

Figure 3.21 Volumetric strain/axial strain curves, 50 kPa effective confining pressure case

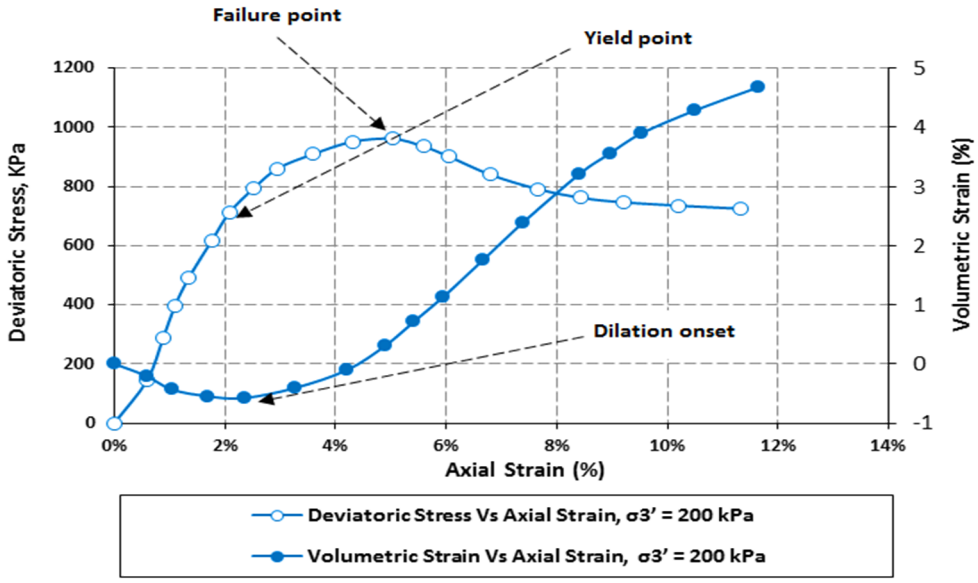

Figure 3.22 Volumetric strain/axial strain curves, 200 kPa effective confining pressure case

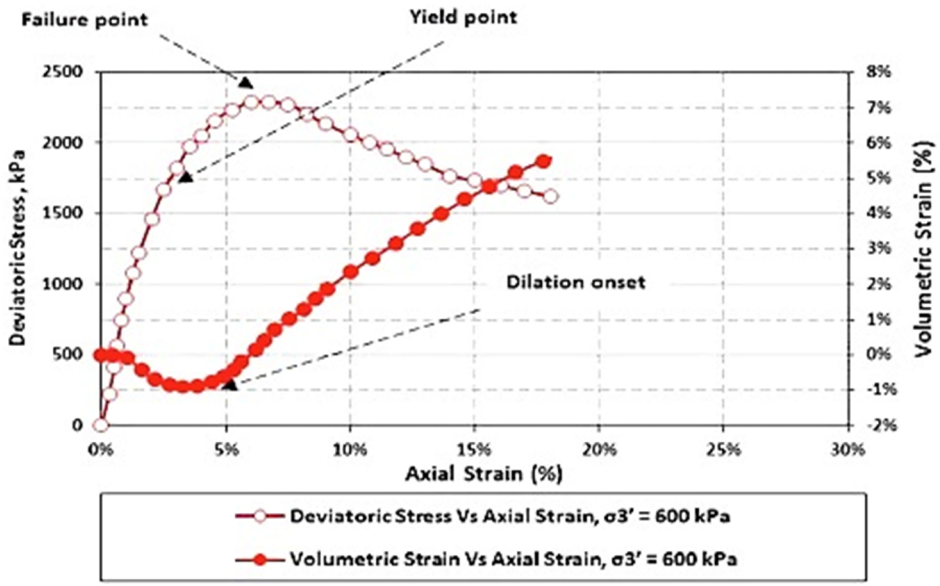

Figure 3.23 Volumetric strain/axial strain curves, 600 kPa effective confining pressure case

As noted in Figures 3.21, 3.22, and 3.23, the onset of sample dilatancy always occurs before or at the yield stress point of deviatoric stress curve. This provides

an important indication of shear bands interference with dilatancy process as volume gain will not take place before reaching the yield stress, which is representing the onset of shear band development according to Wong (2004) study. It is important to mention that both the nature and magnitude of sample deformation are essentially a function of the confining stress and the density of sand. For instance, for loose sand (i.e. density index, (D_r), lower than 0.35) or for very high level of effective confining pressure (i.e. $\sigma_3^{'}$ higher than 1 MPa) both stresses components, (p')and (q), will provoke the same effect: soil contraction at any stage of shearing course (Figure 3.24).

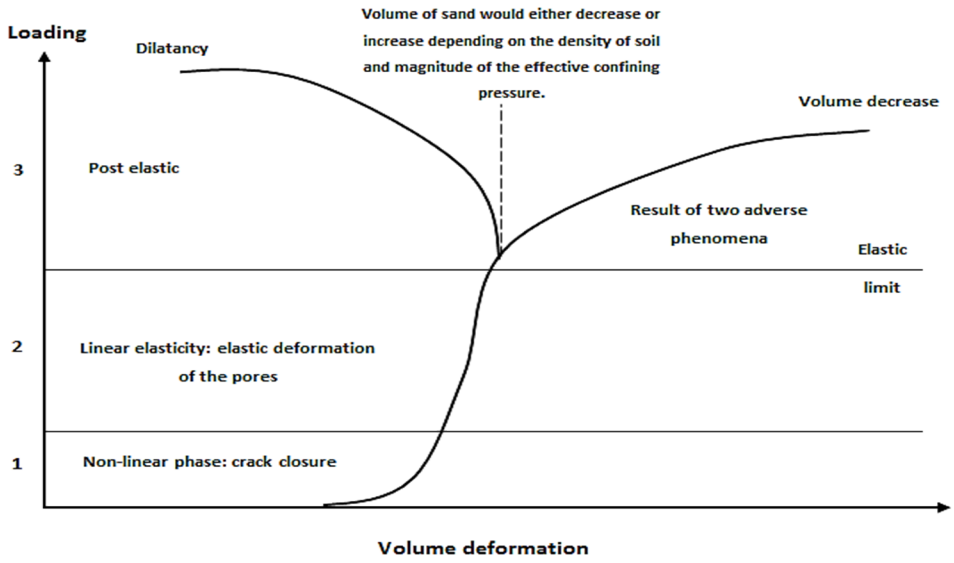

Figure 3.24 Different behavior of sand depending on soil density and effective confining pressure applied during shearing (Ferfera et al., 1997)

3.5.2 Volumetric Strain Alteration and Its Influence on Intrinsic Properties of the Soil

Several mechanisms would explain the volume variation of the sample during the deformation process of the sample: compression mechanism such as vertical grain sliding, grain crushing, pore collapse would usually lead to a major decrease of the porous volume of the sample (i.e. contraction) whereas the

propagation of the shearing bands and distortion of porous media would lead to a volume gain by the soil (i.e. dilatancy). It was noticed through previous studies that a significant permeability enhancement was usually associated to volume increase and shear band development during dilation phase while compaction mechanisms, crack closure and pore collapse, will significantly hinder pore network connectivity and thus an important decrease of permeability would occur. During the shearing course, the relative contribution of previous adverse mechanisms (compaction and dilative shearing) would control the evolution of the geomechanical proprieties of the sample, for instance its absolute permeability.

By the end of shearing, corresponding to the last part of volumetric strain curve, the soil would reach its state of balance between compression and dilation mechanisms. Such state of equilibrium is usually seen as a flattening tendency in the volumetric strain curve, Figure 3.20. With minimal change in volume, permeability variation becomes imperceptible and the influence of mechanical mechanisms (e.g. porous volume variation, etc.) on the absolute permeability of soil turns to be marginal comparing to non-mechanicals (i.e. fines migration). Fines migration is typically resulted from fine grains dislocation into pores throat due to mechanical flow forces. The scope of fines movement and thus the associated permeability reduction is usually a function of the sand morphology and magnitude of the flow rate used during permeability tests. For the test specimens reconstituted for this study, no fines were present in the specimens.

3.6 Porosity Measurement

During the shearing process (compression triaxial test), the porosity of sample does not remain constant but changes at each level of axial strain. Measurement of porosity is usually performed simultaneously with absolute permeability in order to evaluate its mutual impact on permeability during shearing. The triaxial setup used in this testing program did not allow porosimetry measurements to

be made during the triaxial compression tests. Consequently, porosity data was not acquired directly during each triaxial test and the following theoretical equation, Equation 3.9, was used to convert volumetric strain change to porosity at each level of axial strain:

$$\phi_n = \frac{\varepsilon_v + \emptyset_i}{1+\varepsilon_v}, \quad \text{..... (3. 9)}$$

where (ε_v) is volumetric strain, (ϕ_i) is initial porosity before shearing, and (ϕ_n) is corrected porosity at shearing stress.

Subsequently, porosities versus axial strain were generated and plotted for the three effective confing pressures of 50 kPa, 200 kPa, and 600 kPa.

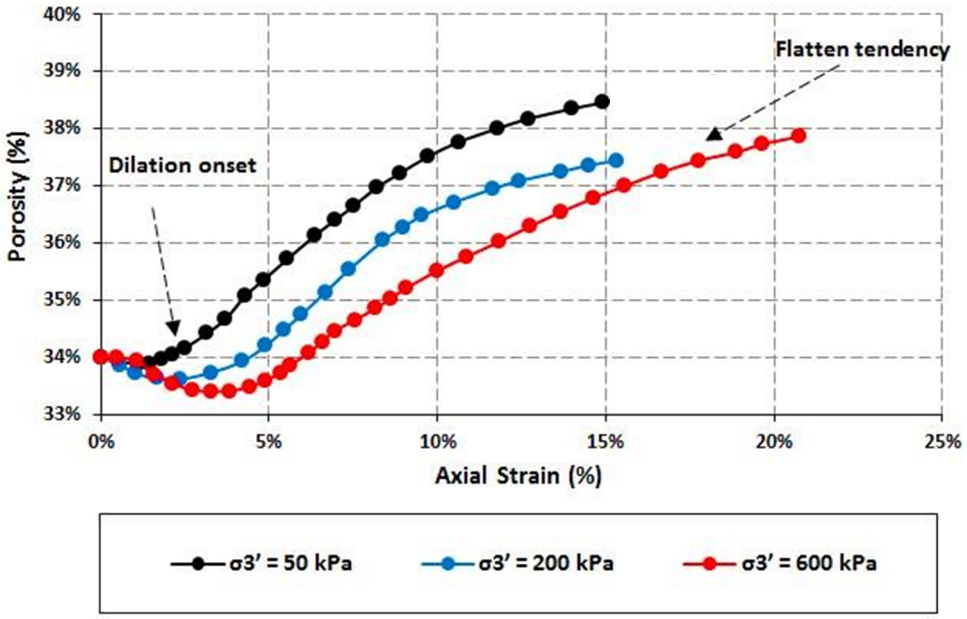

Figure 3.25 Porosity versus axial strain curves for the three effective confining pressures: 50 kPa, 200 kPa, and 600 kPa

A similar shape of the volumetric strain curve was yielded from Equation 3.9: An initial slight decrease of porosity that is followed by a substantial increasing trend before reaching the flatten tendency stage (Figure 3.25). As previously

explained, the equilibrium state between dilation and compaction mechanisms is the principal reason of the flatten tendency shown in porosity curves plotted above. The noticeable porosity's slight variation during the last stage is basically induced from the insignificant variability of porous volume at a higher axial strain range. During this stage, intrinsic properties such as porosity and permeability become more dependent on non-mechanical (fines migration) rather than conventional mechanical factors (porous volume alteration).

It is evident from previous curves that porosity, which is inherently linked to pore volume and interpores connectivity, does not follow an even trend but alter with the continuous change of stress state present within the soil during the triaxial test experiment. Eventually, porosity variation with the increase of applied axial load will impart a subststantial influence on the absolute permeability of the soil, and reciprocally oil drainage from the reservoir. Permeability evolution and its dependency on confining stress and axial load will be studied infurther through next chapters.

3.7 B-Tests Results

A complete saturation of the specimen is considered an imperative prerequisite before starting any triaxial experiment. The presence of air bubble within the porous media of the sample can significantly affect the accuracy of acquired data, especially permeability evaluation during shearing process. By reducing the pore volume present in the sample, air could represent an important impending factor to the water flow through the sample fabric. Indeed, during the preliminary tests, the accumulation of gas bubbles in sample pores and in particular at the sample outlet, had resulted in non-representative measurements of differential pressure between the outlet and inlet of the sample, which resulted in apparent lower values of the absolute permeability of samples. In order to ensure that a B value exceeding 80% was achieved, specimens were first flushed with consecutive upward and backward flows of

warm water before leaving the sample to saturate under a minimum back pressure of almost 400 kPa for at least two days, Figure 3.26. It is believed this process effectively enhanced saturation conditions of the samples.

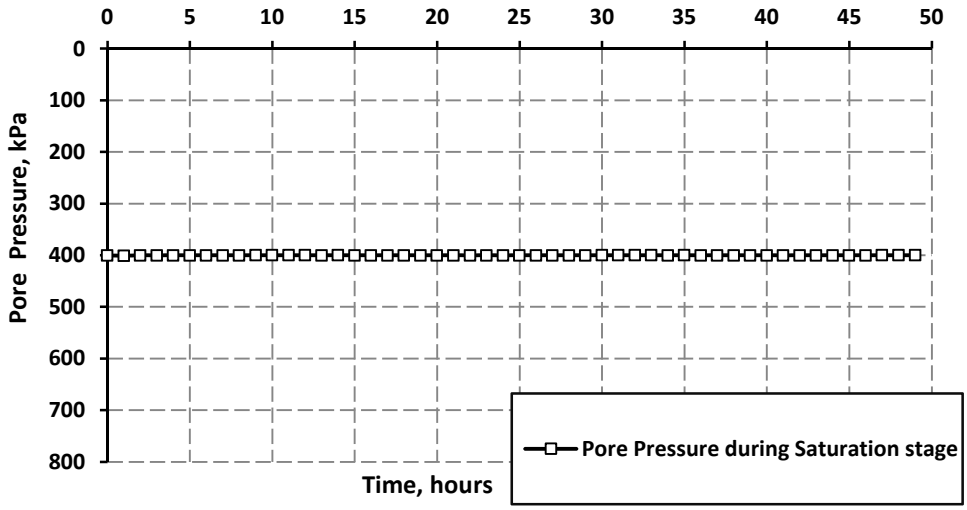

Figure 3.26 Saturation of sample under a minimum back pressure of 400 kPa

The saturation level of samples was evaluated by calculating the pore pressure parameter (B) defined as the ratio of the pore pressure change to an increment of confining stress. For each sample, a successive increase of confining stress was conducted while keeping the back pressure lines closed. The response of pore pressure was measured and the values of the parameter (B) were generated from the following equation (Equation 3.10):

$$B = (\frac{\Delta u}{\Delta \sigma_3}), \quad \text{(3.10)}$$

where (Δu) is pore pressure change and $(\Delta \sigma_3)$ is cell pressure increment.

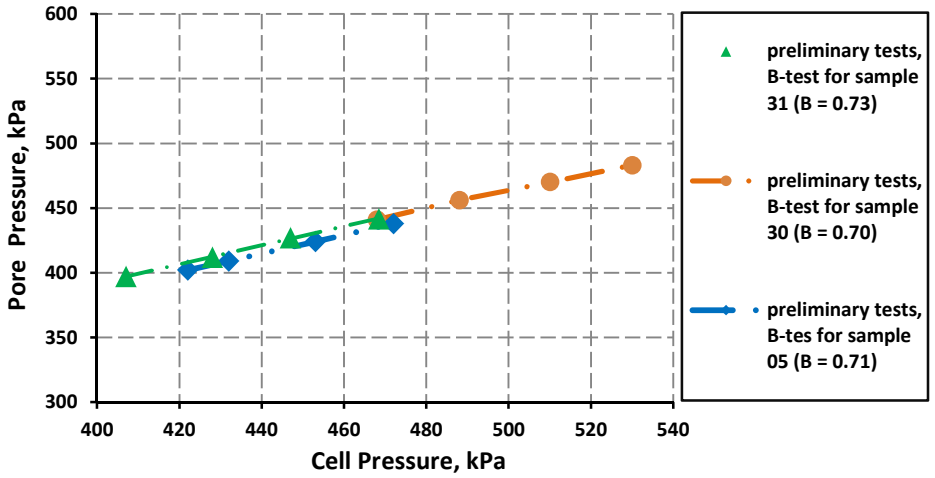

Figure 3.27 B-tests values of preliminary experiments

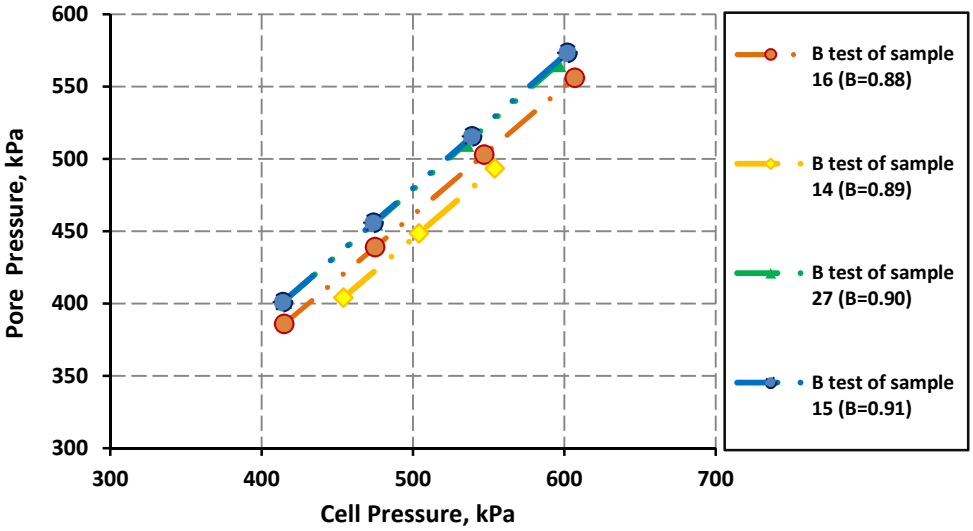

Figure 3.28 B-tests values of different specimens measured prior to shearing process

Results of B-test for different samples used in the triaxial tests are depicted in Figure 3.28. The measured B values, ranging from 0.88 to 0.91, are lower than unity but for these very dense specimens, the saturation levels indicative of B ~ 0.9 was considered acceptable. Agar (1984), in his experimental work on oil sands, considered the use of the common criterion, (B)-value approaching unity,

as unique diagnostic of full saturation as inappropriate or even invalid statement for soils with low compressibility.

Chaney et al. (1997) described an alternative method to evaluate sample saturation state for compressible soil. Throughout his study, Chaney (1997) carried out a series of B-test on various specimens made from dense sand. Based on his experimental results, he concluded that the criterion of full saturation is stratified when the plot of (B) parameter versus back pressure values, induced from successive back pressure increases, depicts a flat line. In others terms, the specimen is considered adequately or fully saturated when the calculated (B) parameters resulted from successive increase of confining pressure become fairly constant and independent of back pressure change. Experimental data computed with accordance to Chaney et al. (1997) criterion of full saturation was plotted in Figure 3.29.

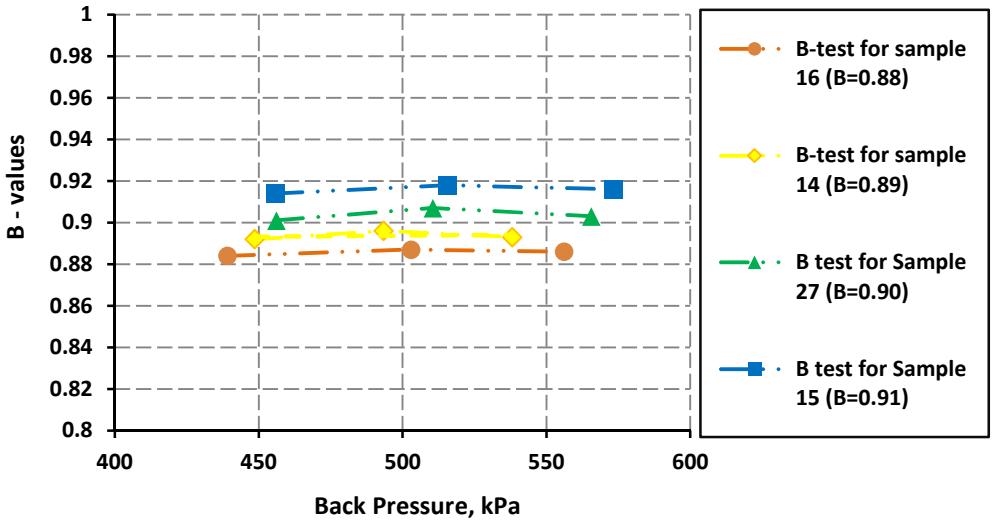

Figure 3.29 Specimen's degree of saturation based on Chaney et al. (1997) criterion

3.8 Absolute Permeability

3.8.1 Absolute Permeability Variation during Isotropic Unloading Test

It is well recognized that the injection of steam in porous media can induce a significant decrease in the effective confining stresses due to the pore pressure rise. Since the initial stress states within a reservoir are rarely isotropic (i.e. all three principal stresses are equal), this alteration of effective stress state within the reservoir will usually result in a slight distortion of the soil by reason of unloading (Yaich 2008). Typically, the induced deformation would impart a substantial variation in most of the intrinsic properties of the reservoir and of particular, its absolute permeability (k).

From a geotechnical perspective, the decrease in the effective stress is usually represented by an isotropic unloading on the p'-q diagram (Figure 1.8) which could be experimentally achieved whether by an increase of the pore pressure while holding the total stress constant or by a decrease of the total stress while keeping the pore pressure constant. During our experimental program, the isotropic unloading tests were conducted by gradually decreasing cell pressure from 800 kPa to 50 kPa while holding pore pressure constant. Figure 3.30 shows absolute permeability and volumetric strain experimental results where values are plotted versus the effective confining pressure. Porosity values were also computed using Equation 3.9 and plotted in Figure 3.31. The volumetric strain measured for the isotropic unloading test showed limited dilation behavior of the samples with only a total volume increase of 0.21% at 50 kPa (Figure 3.30). An associated increase of 8% in absolute permeability was also observed and is correlated to the dilatant volume change. It is important to note that most of the permeability improvement took place under the lower confining stress range (600 kPa-50 kPa). As shown in Figure 3.30, an increase in absolute permeability of 7%, which is corresponding to 90% percent of total permeability enhancement

achieved at the end of the test, was accomplished during the 600 kPa to 50 kPa pressure interval.

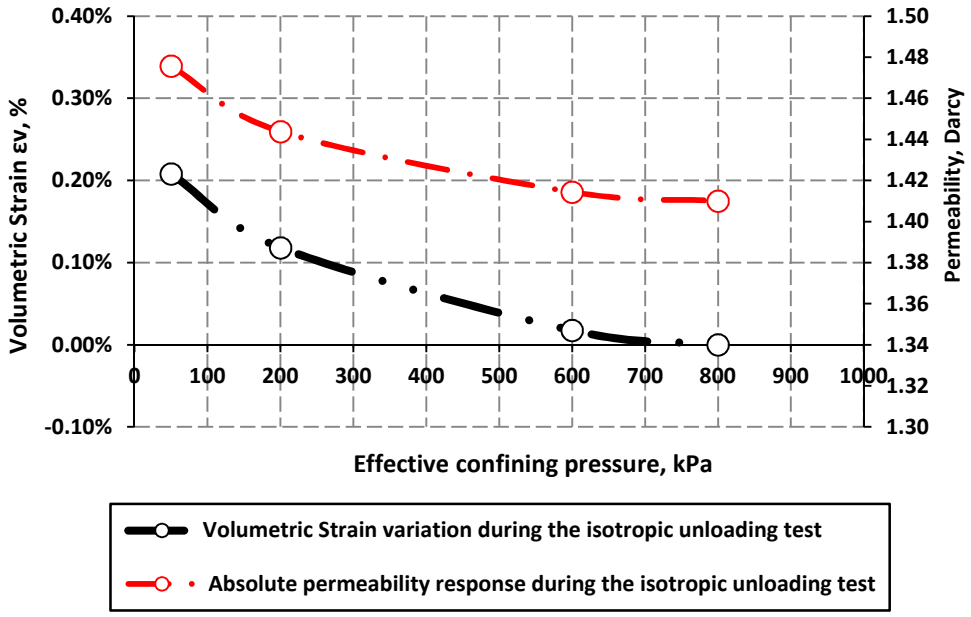

Figure 3.30 Absolute permeability behavior during the isotropic unloading test

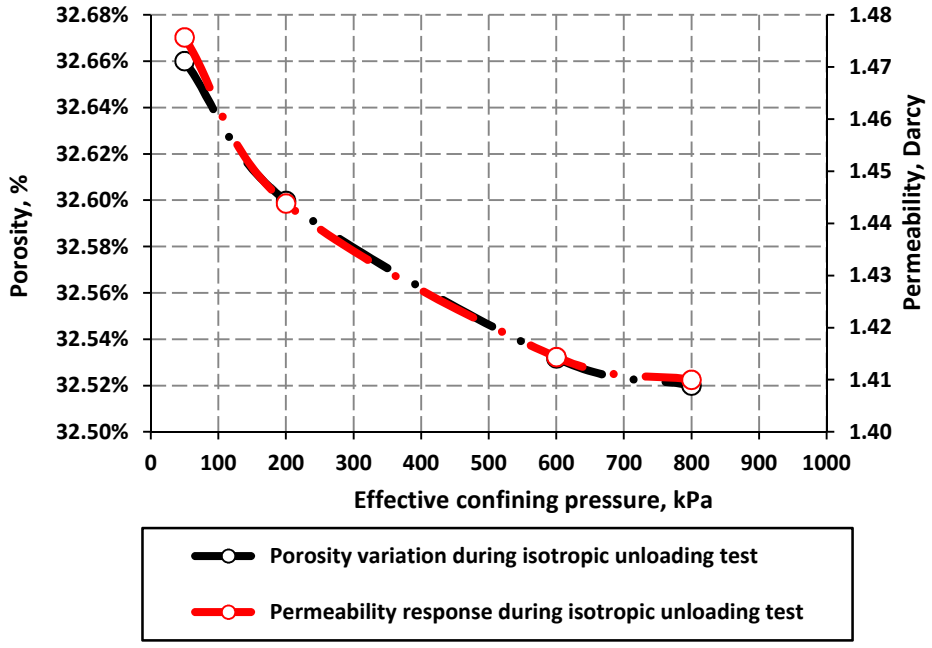

Figure 3.31 Absolute permeability and porosity correlation during the isotropic unloading test

In general, variations in permeability were consistent with volumetric strain change. Figures 3.30 and 3.31 clearly show that absolute permeability, volumetric deformations and porosity of the samples follow similar trends. The strong correlation between permeability development and sample dilation suggest that permeability enhancement is basically attributed to the increase in porous volume achieved through the isotropic unloading test.

3.8.1.1 Empirical Correlation for the Absolute Permeability during the Isotropic Unloading Test

Soil morphology and its effects on permeability were first emphasized by Kozeny (1937) through his permeability prediction model known as Kozeny-Carman (1937) equation. The Kozeny equation is one of the most important and popular equation in geomechanics literature and it is usually presented as permeability versus porosity, grain size, and tortuosity of the soil. According to classical soil mechanics textbook (Taylor 1948, Lambe and Whitman 1969), Kozeny model has been found particularly applicable for cohesionless sandy soils in which the absolute permeability could be predicted through the following equation (Equation 3.11):

$$K = \frac{C\Phi^3 D_S^2}{(1-\Phi)^2}, \quad \text{..... (3. 11)}$$

where the parameter (C) is a function of the shape characteristics of grain and porous volume, (D_s) is the median grain size in microns, (Φ) is the soil porosity in fraction, and (K) is the absolute permeability in (*mD*).

When the Kozeny-Carman equation is used to estimate permeability evolution during the loading process, some of its arguments, mainly grain size and tortuosity, are held constant while porosity parameter is substituted by the corresponding experimental measurements.

Figure 3.32 illustrates the results for the application of the Kozeny-Carman (1937) model to the prediction of permeability evolution during the isotropic unloading test. As shown in Figure 3.32, the resulting correlation with C= 1/180, suggested by Carman for uniform spherical particles, overestimates the measured permeability values of tests specimens. By adjusting the constant (C) while keeping parameters (a) and (b) equal to values suggested by Kozeny and Carman (a=3 and b=2), a better fitting curve to experimental data was yielded when parameter C was considered to be (1/815).

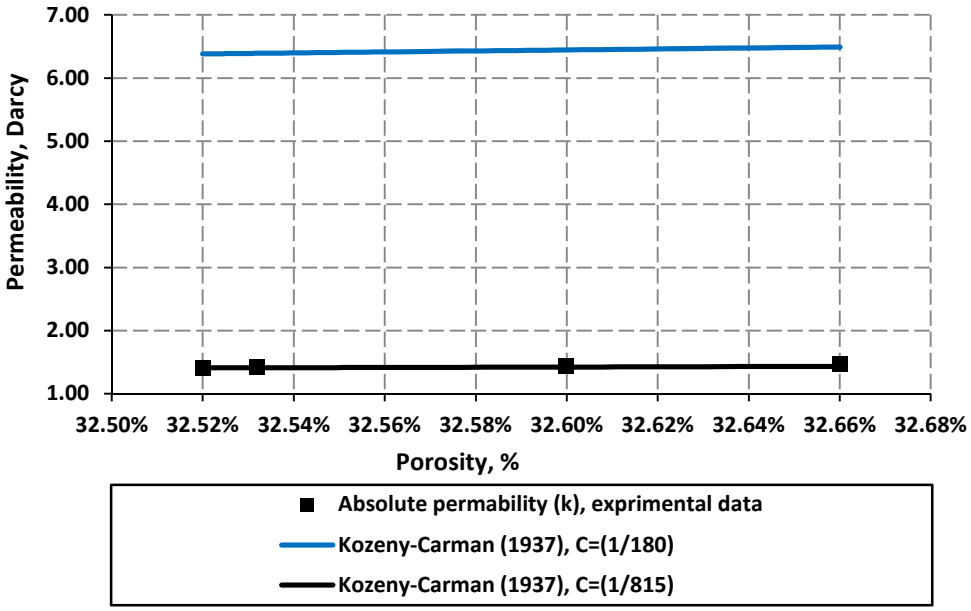

Figure 3.32 Comparison of measured absolute permeability to predictions using the Kozeny-Carman model

The Kozeny-Carman model is generally applied to estimate the initial permeability of the soil rather than predicting its evolution when the material is going through changes in the stresses state. To overcome this major limitation, a linear semi-logarithmic correlation relating permeability to volumetric strain level was derived by Touhidi (1998) through an extensive analytical study on his results of permeability tests conducted on McMurray sand. One valuable feature of Touhidi (1998) equation is that the volumetric strain instead of the porosity is

used to directly calculate the changes in permeability as a result of volumetric strains.

The Touhidi (1998) relationship between absolute permeability and volumetric strain is described in Equation 3.12:

$$Ln\left(\frac{K_2}{K_1}\right) = C_{\Phi}\varepsilon_v, \quad \text{(3. 12)}$$

where the term (C_Φ) is a function of initial porosity (Φ_i) as defined by Equation 3.13:

$$C_{\Phi} = \frac{B}{\Phi_i}, \quad \text{(3. 13)}$$

By substituting (C_Φ) by its expression into Equation 3.13, the following correlation was yielded:

$$Ln\left(\frac{K_2}{K_1}\right) = \frac{B}{\Phi_i}\varepsilon_v, \quad \text{(3. 14)}$$

where (K_1) is the initial absolute permeability, (K_2) is the new permeability value associated to the volumetric strain level (ε_v). The parameter (B) was suggested by Touhidi as an indication of the rate of change of absolute permeability (K) with the change of volumetric strain level (ε_v).

The least square regression method was used to estimate the parameter (B) in the Touhidi model. The parameter value determined for the test specimens under isotropic unloading conditions was found to be 7. This value is of the same order of (B) values reported by Touhidi (1998) for his vertical McMurray sand specimens.

Previous correlations (Kozeny-Carman (1937), Touhidi (1998)) are plotted for comparison in Figure 3.33. The Touhidi (1998) model appears to better describe the relationship between volumetric strain and permeability during the isotropic

unloading path than Kozeny-Carman equation. A lower absolute deviation of +/- 0.003 Darcy to experimental data was achieved for the Touhidi (1998) equation compared to +/- 0.047 computed for the Kozeny-Carman model.

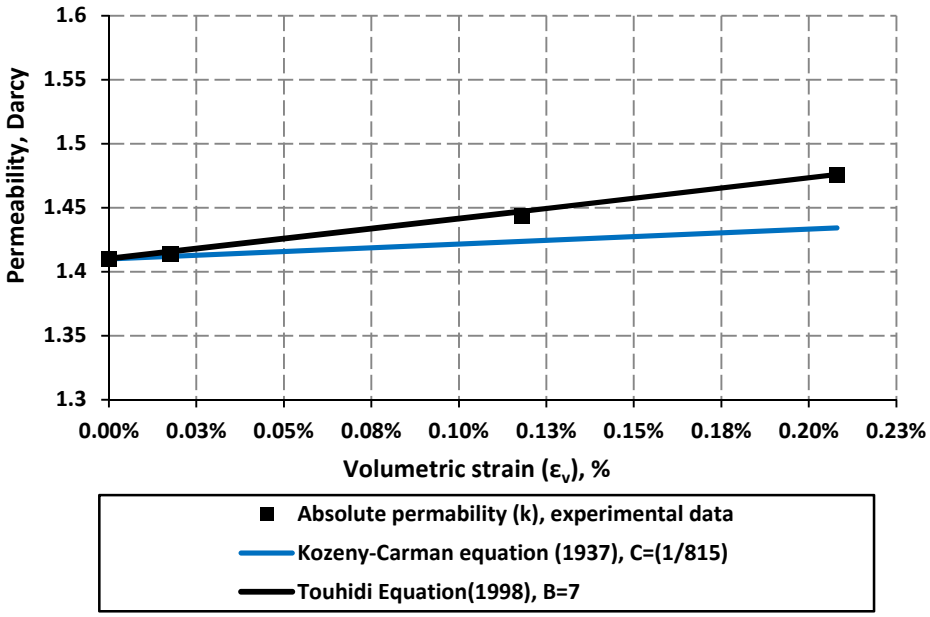

Figure 3.33 Variation of absolute permeability simulation (graphical comparison between Kozeny-Carman (1937) and Touhidi (1998) models)

Direct and simple correlation relating permeability to porosity alteration was suggested by Oldakowski (1994) to appraise the absolute permeability response during isotropic unloading test (Equation 3.15):

$\Delta K = \beta\ \Delta\emptyset$, ... (3. 15)

where (ΔK), in Darcy, denotes permeability increase resulted from porosity increment ($\Delta\Phi$) (in fraction), and (β) represents material constant (β= 32 for McMurray Formation sand).

Subsequently, least square regression method was initiated to estimate parameters in the Oldakowski (1994) model. Results are described in Equation 3.16:

$$\Delta K = \beta\, \Delta\emptyset$$
$$= 42\Delta\emptyset, \quad \text{..... (3. 16)}$$

The slope of curve, (β), obtained from the experimental data in this study differs substantially from the one reported by Oldakowski (1994) for the McMurray sandstone specimens (i.e. higher material constant (β) of 42 was obtained for the specimens in this study). The previous observation implies that the absolute permeability of samples used in the current study exhibited a higher sensitivity to confining stress alteration in comparison to samples used by Oldakowski (1994) during his experimental course. The greater sensitivity of the sand specimens reconstituted for this study may be the result from the difference in initial porosity and/or level of consolidation between the two set of samples.

A simple development of previous Oldakowski (1994) equation yielded the following correlation where the new permeability, K_2, can be calculated from initial permeability value, K_1, and the measured rate of porosity variation, ΔΦ, ($\Delta\Phi=\Phi_2-\Phi_1$):

$$K_2=K_1+\beta\ (\emptyset_2 - \emptyset_1), \quad \text{..... (3. 17)}$$

It is notable that Equation 3.17 doesn't take into consideration the effect of confining pressure level on the sensitivity degree of the soil permeability. In his simulation model, Oldakowski (1994) assumed that a certain variation in porosity, ($\Delta\Phi$), will induce exactly the same order of permeability change whether unloading test was conducted under low or high stress level (i.e. in this section, an effective confining stress level is considered high if it is greater than 200 kPa). This observation by Oldakowski (1994) is not supported by the results of this study. Figures 3.30 and 3.31 clearly demonstrate the confining pressure

level as an important influence factor on soil permeability and its sensitivity to porosity alteration. Actually, for the same increment of porosity ($\Delta\Phi$), a higher permeability increase would typically occur when the isotropic unloading course is achieved under a low level of effective confining, less than 200 kPa. Previous statement was confirmed by the obvious increase in deviation between the linear curve of Oldakowski (1994) equation and our experimental data as loading conditions of the sample approach the confining stress limit of 200 kPa (Figure 3.34).

The notion of effective porosity *(Φ')* is essential to explain the sensitivity of permeability to effective confining stress level. Effective porosity *(Φ')* is commonly used by petroleum studies to refer to the volume of porous media actually available for the fluid to flow through, and it is usually quantified by deducting the volume of non-interconnected pores from the total porous volume. Effective porosity is usually lower than total porosity as it encompasses the interconnectivity state of the pores. It seems that permeability response within the higher range is mainly dependent on the effective porosity, *(Φ')*, of the soil rather than its general porosity, (Φ). This interpretation is also consistent with the stiffness gain showed in the soil under high confining pressure stated in previous chapters. The gain of stiffness basically results from the substantial increase in the contact surface between grains which is consequently inducing an important pore throat constriction and so significantly hindering the effective porosity (Φ') of the soil (i.e. important change in the interconnectivity conditions of the porous volume). Sensitivity of effective porosity value to the effective confining pressure implies the need of considering confining pressure level as a crucial parameter during reservoir simulation.

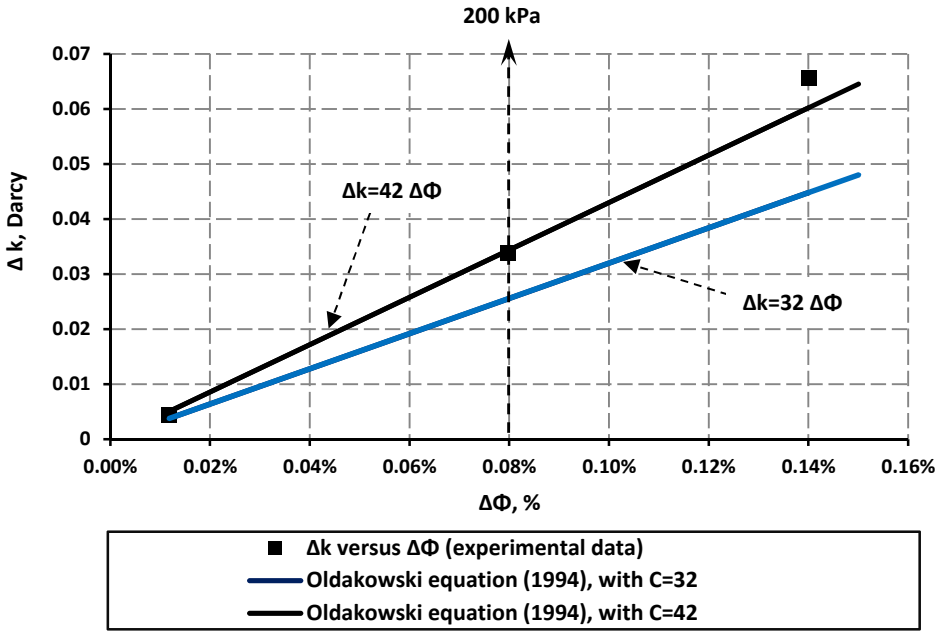

Figure 3.34 Absolute permeability and porosity correlation during the isotropic unloading test basing on Oldakowski (1994) equation

Finding a correlation between effective confining pressure and permeability variation is not only important in the assessment of how injection processes soil properties, but aids in the extrapolation of laboratory measurements conducted within certain confining pressure range to real in-situ reservoir conditions. These extrapolations are particularly important for cohesionnless soil. The lack of cohesion (i.e. cohesionless) in granular soils makes the recovery of undisturbed core from such formations extremely difficult. As such, most core results yielded from laboratory experiments are usually considered invalid, given the high core-disturbance results in test specimens. Thus, the need of an appropriate model to extrapolate the laboratory results to the real reservoir pressure becomes vital for a reliable reservoir simulation. By drawing the tendency curve through the experimental data plotted in Figure 3.35, the following exponential correlation relating absolute permeability (k) to confining pressure (σ_3') was generated:

$$K = K_o e^{(-a\sigma_3')}$$

$$= 1.471e^{(-6x10^{-5}\,\sigma_3')}, \quad \text{..... (3. 18)}$$

Where (K) is the absolute permeability at certain effective confining pressure (σ'_3), (K_O) is the initial absolute permeability at 0 kPa (in Darcy), and (a) is a material constant found to be equal to (6×10^{-5}) kPa^{-1} for our reconstituted sand samples.

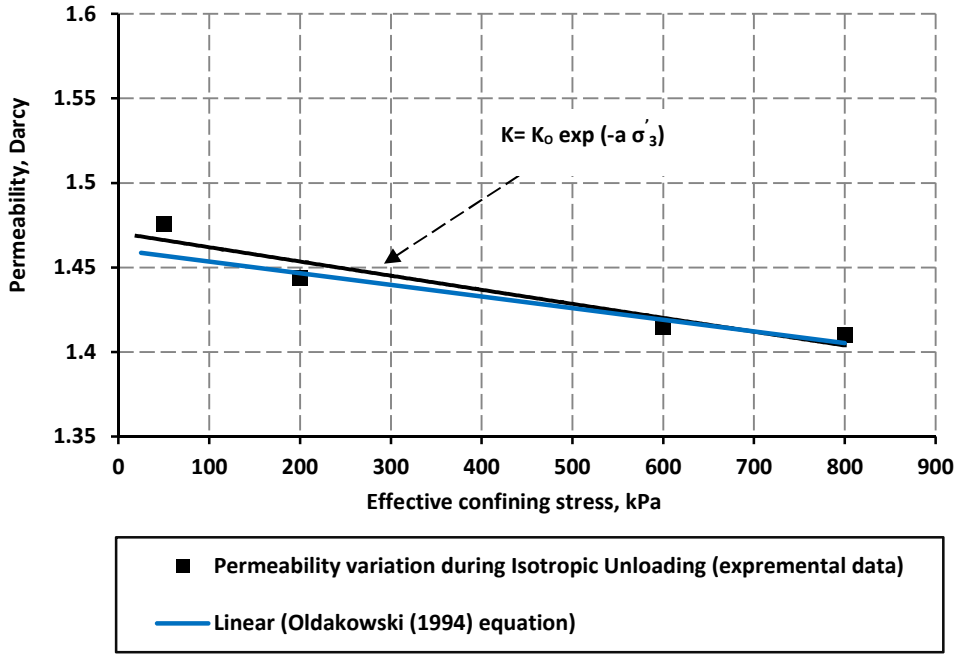

Figure 3.35 Absolute permeability and porosity correlation during the isotropic unloading test (comparison between exponential model (Equation 3. 18) and Oldakowski (1994) Equation (Equation 3. 17))

As shown in Figure 3.35, the extrapolation of absolute permeability from Equation 3.18 yielded a better estimation with less deviation to experimental data in comparison to Oldakowski (1994) model. However, it is worth mentioning that a good accuracy of the simulation model described in Equation

3.18 is restricted to soils that share similar morphologic and petrophysical properties of the sand utilized in this study.

3.8.2 Absolute Permeability Variation during Triaxial Compression Tests

It is well recognized that fluid injection into oil-bearing formations induces a significant alteration of the reservoir stress state. Such stress alteration is typically associated with an important combination of elastic and plastic deformation resulting from the mechanical and thermal effect of injected fluids (e.g. steam, combusted gas, etc.).

Soil expansion, which is considered as the most evident result of the SAGD thermal effect on the soil, could significantly enhance the entire intrinsic properties of the reservoir and principally its absolute permeability (k). From an experimental perspective, such soil deformation could be easily simulated by deploying a compression triaxial system in which the deviatoric stress is substantially increased while the confining stress is maintained constant. Previous experimental procedure is believed to adequately represent the stress path followed by reservoir during thermal expansion of the soil (Touhidi 1998).

During our experimental course, triaxial compression experiments were performed under three levels of effective confining stresses: 50 kPa, 200 kPa and 600 kPa. Subsequently, successive measurements of absolute permeability were achieved at different values of axial strain. Results of different triaxial compression tests are shown in Figure 3.36.

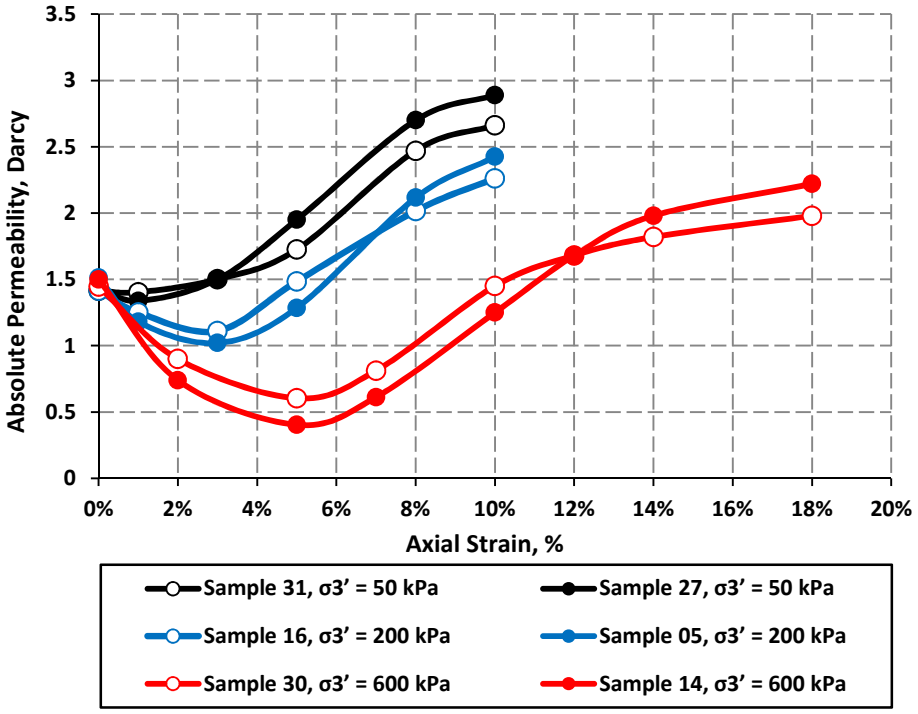

Figure 3.36 Absolute permeability for the three effective confining pressures: 50 kPa, 200 kPa, and 600 kPa

Permeability curves at the three effective confining pressures (50 kPa, 200 kPa, and 600 KPa) followed very similar behavior: an initial decrease of permeability followed by a substantial rise with increasing deviatoric stress, but with a larger initial reduction and smaller subsequent gain of absolute permeability associated to higher range of effective confining pressures. In general a decrease in absolute permeability was recorded in the beginning of shearing process to reach a maximum reduction of 45% below its initial value at an axial strain of 5% in the 600 kPa effective confining pressure case, and approximately 22% reduction at 3% axial strain in the 200 kPa case. Almost no permeability reduction is reported for 50 kPa effective confining pressure experiment. Nevertheless during dilation phase; the maximum permeability rise was attained in the 50 kPa effective confining pressure case with an average gain percentage of 88% at 10 % of axial strain (i.e. 88% is the average of absolute permeabilities

measured for both samples 27 and 31), followed by an average value of 60% and 35% respectively reported for 200 kPa at 10% axial strain and 600 kPa at 18% axial strain (end of the test).

As evidence of the correlation between volumetric strain and permeability evolution of the sample during shearing, stress strain and volumetric strain curves as well permeability results were all plotted at the same scale in Figure 3.37. As shown in Figure 3.37, permeability enhancement was invariably associated to dilation onset of the sample. A significant enhancement in permeability would not occur before reaching a certain level of dilation by the sample and this true for every effective confining pressure of our study: 50 kPa, 200 kPa, and 600 kPa. However, it is noted that effective confining stress has an adverse effect on the absolute permeability enhancement. For instance, by raising the effective confining stress to 200 kPa the absolute permeability gain of 80% achieved at 10% axial strain for the 50 kPa case was partially suppressed to report a lower total enhancement of 60%. In general, shearing at higher confining pressure levels (600 kPa or higher) would inhibit permeability increase for the triaxial compression test, even though the volumetric strain is still dilatant. For instance, in the 600 kPa triaxial compression test, an evident enhancement in the absolut*e* permeability of core sample was not observed before reaching 15% axial strain. Prior to this axial strain threshold, data showed a general tendency toward permeability decrease with an increase of differential stress (Figure 3.36). Desrues (2004) explained such permeability behavior by referring to the shear band development and the dissimilarities of their spatial configuration when samples were confined under different level of confining pressure. Desrues (2004) observed that narrower shear bands would be resulted when shearing at a high range of effective confining stress. This narrow aspect is mainly resulted from the more important restrains applied on the material fabrics under the higher pressure. Higher constraints would firmly hold the shear bands expansion and so would inhibit a further improvement of permeability

despite the high volumetric strain (ε_v) achieved. In the same context, Touhidi (1998) believed that, at higher levels of effective confining pressure, the shear bands have more effect on enlarging the flow path rather than improving the interconnectivity state of the pores. Thus, at the same volumetric strain (ε_v), specimens under high confining stress would report lower permeability values than those sheared under low confining stress level (Figure 3.38).

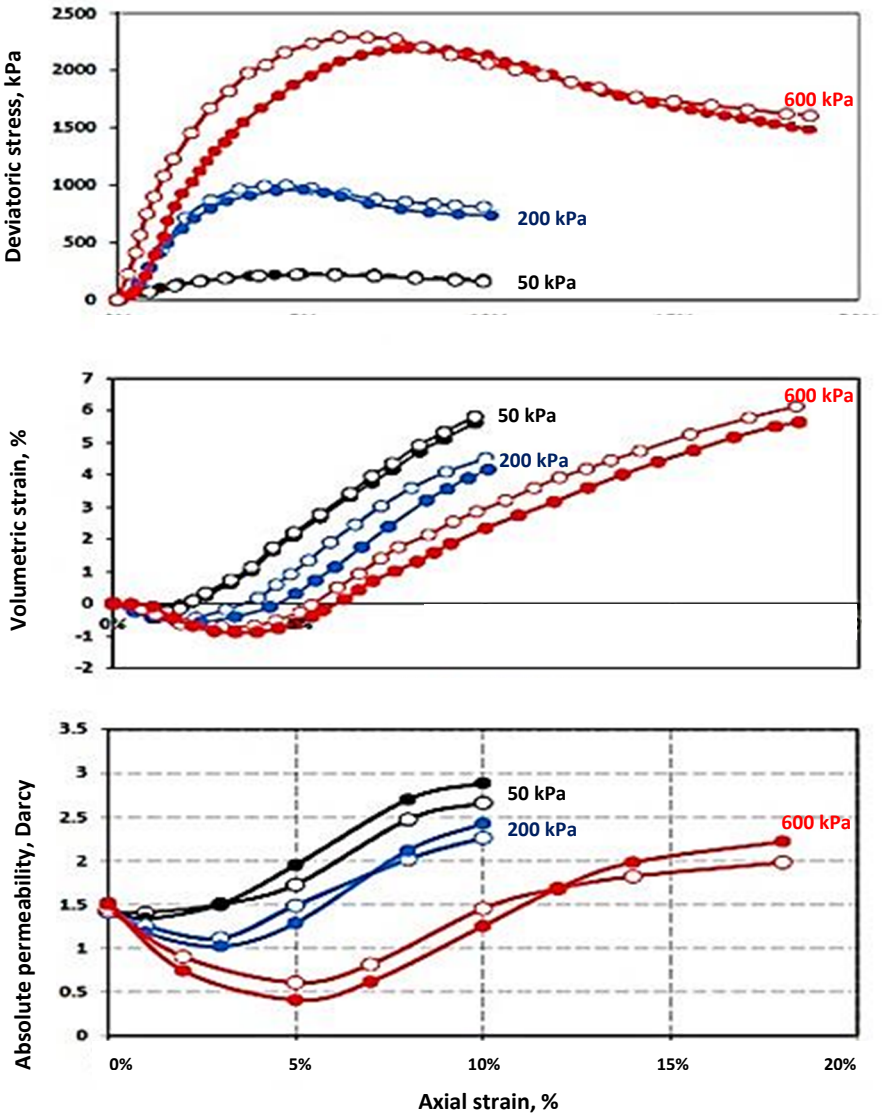

Figure 3.37 Summary of experimental results: stress strain, volumetric strain, and permeability curves (O and ● denote results for repeated tests at the same effective confining stress).

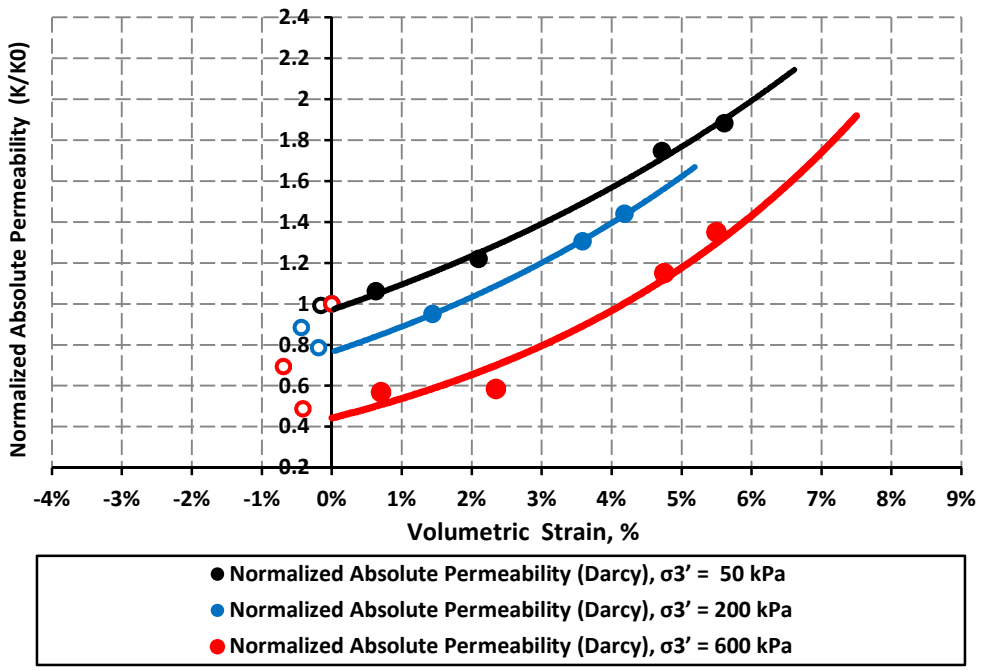

Figure 3.38 Normalized absolute permeability versus volumetric strain for the three effective confining pressures: 50 kPa, 200 kPa, and 600 kPa

Experimental data proved a strong consistency between volumetric strain and absolute permeability response of the soil: the more the sample dilates, and the more absolute permeability improvement is observed. This relationship was evidenced in Figure 3.39 where normalized absolute permeability and normalized porosity were plotted against the axial strain. The similarity in both curves is striking. Both curves showed an initial decline followed by a substantial increase where the transition between these two responses corresponds to the onset of dilation. The most critical, however, is the delay between the beginning of permeability enhancement and dilatancy onset, which seems to be proportional to the level of effective confine stress applied. As can be seen, when the permeability response to dilation onset was practically instantaneous for 50 kPa, the lag between dilation onset and permeability enhancement was noticeably significant in 600 kPa case (Figure 3.37). This delay observed in the high effective confining pressure case is likely due to changes in flow path

tortuosity or distortion in pore networks of the sand. During the compaction stage that occurs at initial stages of the shearing process, a severe distortion of porous network is recognized to occur as a result of grain dislocation and alteration of the stress state of the sample. Such alterations in pore network in the sand would severely hinder the pore inter-connectivity and would result in a decline in the absolute permeability. This lack of connectivity between pores will be partially but not completely compensated by the development of shear bands during the dilation phase. Shear bands would increase the pores throat size and so relatively enhances the permeability of sample. Nevertheless, under high levels of effective confining stress, the damage in the inter-connectivity occurring during compaction stage is more obvious and thus a larger dilation in the pores volume is usually required to compensate the adverse impact of such damage on the absolute permeability of the soil.

It was also notable from Figures 3.38 and 3.39 that the absolute permeability value at the beginning of net dilation (i.e. the net dilation onset corresponding to 0% volumetric strain in Figure 3.38), is lower than its initial value before the start of shearing process. This behavior provides an additional indication that flow tortuosity, in addition to volumetric strain, plays an important role in controlling the absolute permeability evolution of the sample.

Several driving mechanisms are involved in the compaction process of the sample. Most of them are typically mechanical and their impact could be summarized as elastic/plastic deformations in the porous media of the sand. At the end of this spectrum, pore inter-connectivity appears to be the most important non-mechanical factor that controls permeability evolution during the shearing process. The remarkable dissimilarities between the initial permeability, before the start of shearing, and permeability value reported at the onset of sample dilation could be explained by the damage of inter-connectivity state that is postulated to occur during the contraction phase at the start of shearing.

The dislocation of grains during compaction usually induces an irreversible change in the connectivity state of the porous volume that is not totally recovered during the subsequent dilation phase. Thus, the initial permeability will never be restored even if the sample recovers its original volume (i.e. volumetric strain equal to 0% or normalized porosity equal to 1). It is important to mention that degree of disturbance of the porous network during compaction is proportionally related to the applied confining pressure. At higher ranges of effective stress, the compaction of a sample is more important and thus pores inter-connectivity alteration is generally more severe. An important limitation within the current study was that the scope of the experimental investigation was restricted to the evaluation of pore volume alteration (i.e. volumetric strain) on the permeability response of dense, reconstituted sand specimens. The effect of other factors such pores connectivity, shear band geometric configuration were not studied and the magnitude of their impacts is not entirely clear.

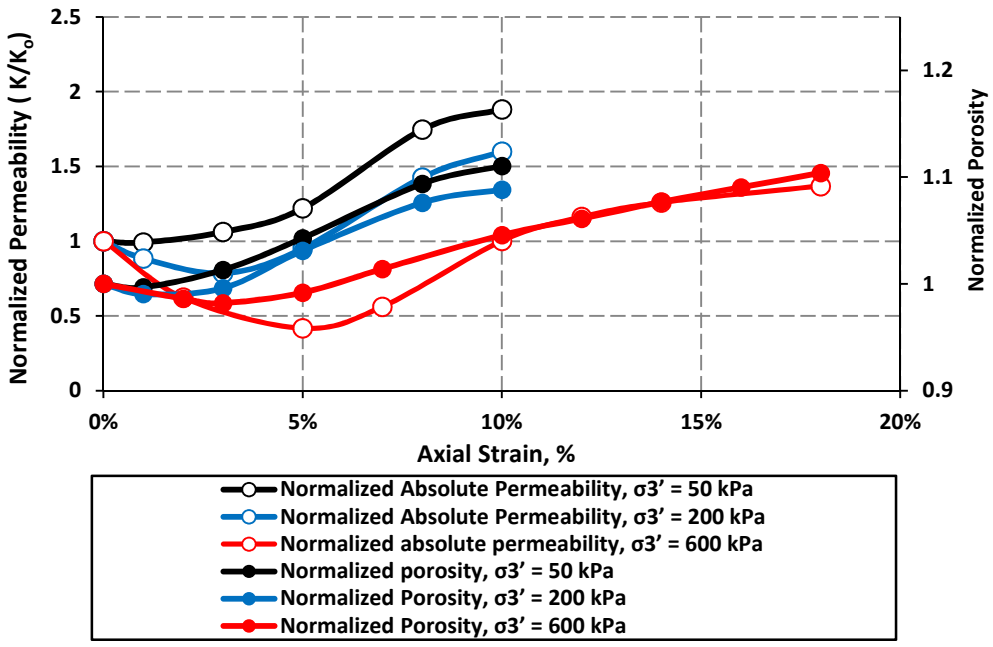

Figure 3.39 Normalized absolute permeability versus axial strain for the three effective confining pressures: 50 kPa, 200 kPa, and 600 kPa

Although the number of measurements included in this study is limited to allow for an accurate quantitative assessment of permeability behavior, the experimental results show a consistent relationship between the applied confining stress and permeability behavior. Regardless of the magnitude of permeability decrease and measurements consistency recorded in this study, the general tendency of permeability enhancement is to decline with the increase of confining stress. This inverse correlation between permeability enhancement and effective confining stress, suggests there exists an effective confining stress level above which shear dilation will not enhance permeability any more. From a field perspective, higher effective confining stress is an indication of higher overburden pressure, which implies that at certain reservoir depth the thermal expansion of the reservoir will not induce the desired permeability rise. Thus, a careful selection of SAGD wells location become vital to ensure a production efficiency of thermal recovery technique. However, it should be taken into consideration that only the axial permeability was assessed through our experimental course. Other sand permeabilities such as lateral and radial permeability should be accounted in for more accurate appraisal of permeability evolution during oil thermal recovery.

3.8.2.1 Sensitivity of Absolute Permeability to Boundary Conditions

As noted before, our samples exhibited a lower permeability values when a higher range of effective confining stress was applied. Such permeability behavior is commonly explained by the higher dilatancy usually observed when samples were sheared at low effective confining pressure. However, the significant difference in permeability values between the 200 kPa and 600 kPa effective confining pressure cases seems more pronounced than the dissimilarities in porosity evolution between the two pressures would justify. The difference in intrinsic properties between samples such as initial porosity could be an important factor in controlling the permeability response (Desrues 2004).

Yaich (2008) reported that samples with lower porosity and higher density have invariably yielded a superior permeability enhancement for his both radial extension and triaxial compression tests. The slight difference in initial porosity between our samples compounded with the impact of the higher confining pressure applied during the 600 kPa tests could considerably exacerbate the sensitivity of the test specimen absolute permeability to volumetric strain alteration, resulting in the unexpected low absolute permeability value obtained at the end of the 600 kPa effective confining pressure test.

Boundary conditions could also be an important influence on permeability performance. It is evident from SEM analysis that the axial distribution of porosity within the sample is not uniform after shearing (Figure 3.40). The arrangement of the grain at the upper and the bottom parts of the specimen are more compacted compared to the middle parts. At higher axial strain, the effect of such lower porosity zone could dominate the formation of shear bands and their spatial configuration through the specimen. Major shear bands that cross the sample from the bottom to the top of the sample could represent important shortcut for the water flow and so prompt the increase of absolute permeability during shearing. However, presence of discontinuities in the shear bands can hinder the water flow through the sample and thus compromise the overall permeability of the soil. Such breaks in shear bands seem to take place within the over-compacted zones of the test specimens. The significant compaction observed at the sample extremities could provide a plausible reason for the pronounced permeability decrease observed in the 600 kPa confining pressure experiment.

It is commonly recognized that the boundary restraint resulting from the use of rigid loading platens will influence a specimen's strength and the sensitive relationship between volume changes and permeability evolution. The influence of rigid platens usually results in an irregularity of porosity distribution between

the area adjacent to platens and rest of the sample (Figure 3.40). The non-uniform deformation of the sample during the shearing course can generate erroneous results that usually lead to incorrect or inconsistent conclusions. The use of stiff lubricated platens with silicon grease as an alternative to conventional porous platens was commonly recommended by previous researchers (Touhidi 1998, Oldakowski 1994). Using lubricated platens will significantly reduce friction between platen and sample fabrics, which is imposing a uniform distribution of stresses over the sample and thus more regular deformations during the dilative stage of the shearing course.

3.8.2.2 Empirical Correlation between Volumetric Strain and Induced-Permeability Variation

Several studies have examined the relationship between soil permeability and volumetric strain/porosity during the shearing process. These studies were based on laboratory tests conducted under controlled loading circumstances generally structured to stimulate a specific stress path. However, most estimation models reported in prior researches investigated only the permeability evolution associated to dilation part of soil behavior where the effect of effective confining stress level on permeability behavior was intentionally neglected either for simplicity's sake or because the analysis of experimental data has justified such assumption.

This section attempts to improve the prediction of empirical correlations reported by previous researches (Oldakowski 1994, Touhidi 1998) by incorporating the effect of effective confining stress as crucial parameter in the estimation model. This has been mainly done by performing regression analysis procedures on the absolute permeability results reported in the triaxial experiments.

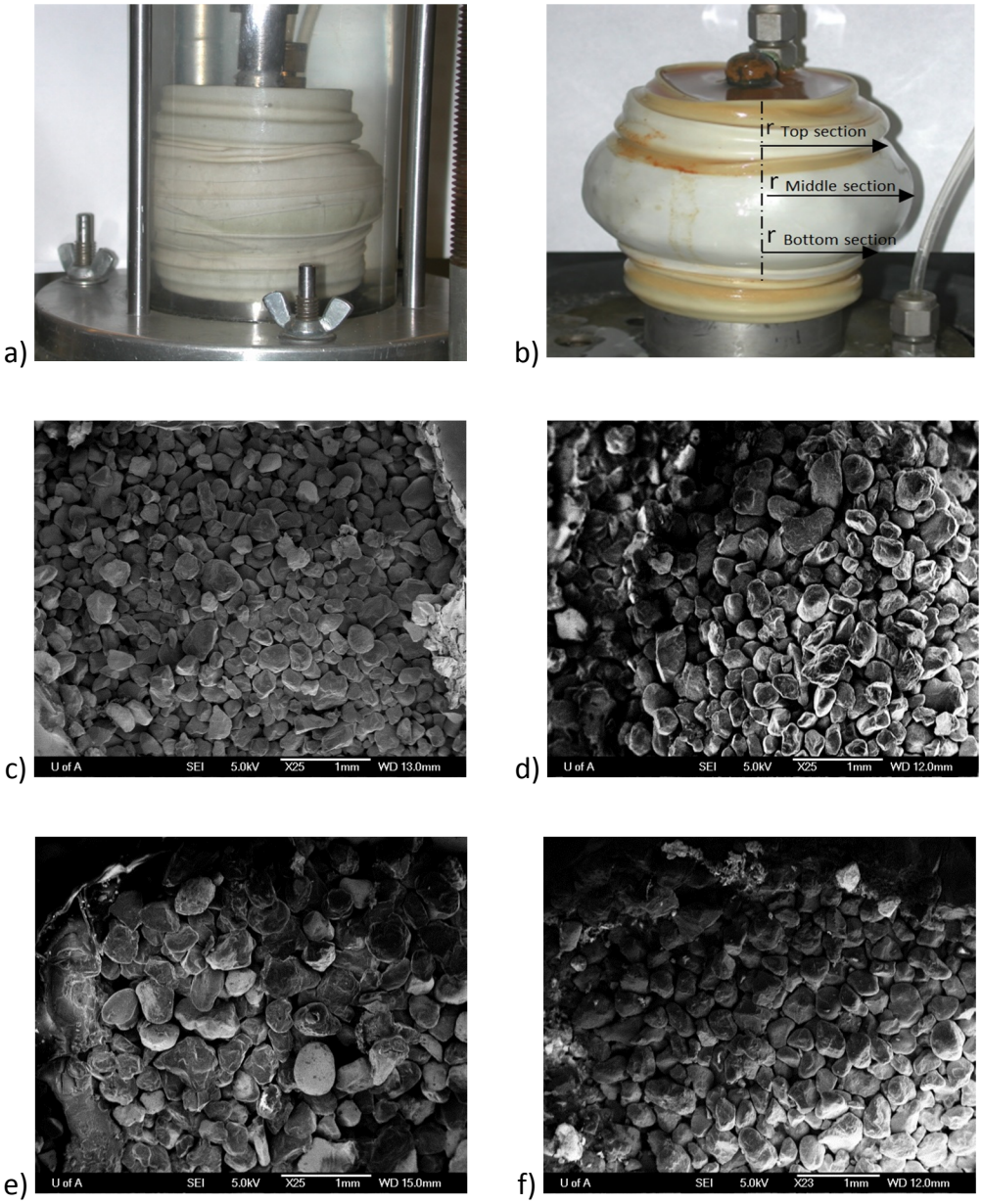

Figure 3.40 Sample deformations after shearing, 600 kPa effective confining pressure case: a) Sample during shearing process, b) Uneven deformation of the sample, c) Grains arrangement before shearing, d) Bottom of the sample after shearing, e) Middle of the sample after shearing, and f) Top of the sample after shearing

Figure 3.41 represents the normalized absolute permeability versus the volumetric strain of each case of effective confining pressures: 50 kPa, 200 kPa, 600 kPa. Subsequently, a regression analysis was initiated to generate trend line curve through permeabilities data. It is clear that the curve fit using the exponential equations shown in Figure 3.41 fits well the dilation part where the shear induced volume change is present.

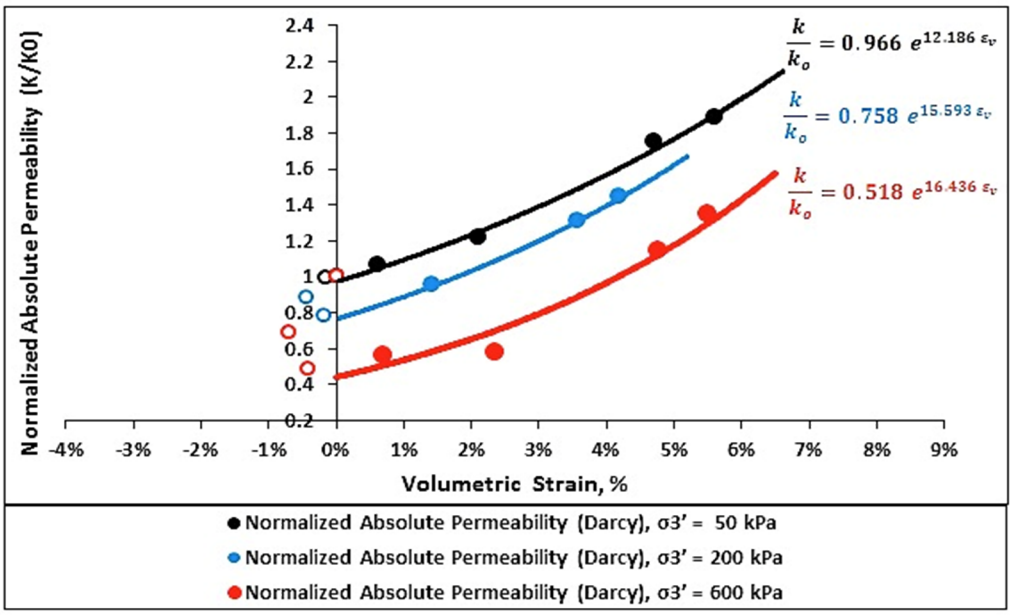

Figure 3.41 Normalized absolute permeability versus volumetric strain for the three effective confining pressures: 50 kPa, 200 kPa, and 600 kPa

The following generalized form of the exponential correlation between normalized absolute permeability and volumetric strain was developed and so adopted for our experimental results:

$$\left(\frac{k}{k_i}\right) = \alpha e^{(\beta \varepsilon_v)}, \quad \text{..... (3. 19)}$$

where (α) denotes the normalized permeability at the beginning of dilation,(β) is an indicative to the rate of absolute permeability change with the change of

volumetric strain,(ε_v) is the volumetric strain in fraction, (k) is the new absolute permeability, and (k_i) is initial absolute permeability of sample before shearing.

To demonstrate the sensitivity of absolute permeability to the effective confining pressure, two correlations expressing both arguments (α) and (β) as function of effective confining pressure were derived and consequently tested for their consistency with experimental data.

A power law model (Equation 3.18) was reported in previous chapter as appropriate to describe the correlation between absolute permeability and effective confining stress during the isotropic unloading path. For simplicity sake, the same power model described in the Equation 3.18 was used to predict the variable (α) of Equation 3.19:

$$\alpha = e^{(-a\sigma_3')} \quad \text{..... (3. 20)}$$

Hamoud (2012) suggested the following equation for the variable (β) based on simple development of Kozeny-Carman equation.

$$\beta = \frac{a(1-\emptyset_0)+b\emptyset_0}{\emptyset_0} \quad \text{..... (3. 21)}$$

where (a) and (b) are fitting parameters and reported to be respectively equal to "2.8" and "1.9" for the experimental results generated in this study. The match between the previous values computed for (a) and (b) based on the permeability data and those suggested by Kozeny-Carman equation (i.e. (a) =3 and (b) =2) is very good. In the same fashion as above, the following equation (Equation 3.22) was proposed by Touhidi (1998) as simple alternative form to describe the argument (β):

$$\beta = \left(\frac{B}{\emptyset_i}\right) \quad \text{..... (3. 22)}$$

where (B) was computed to be "2.5" based on the permeability results from the testing described above. Numerical values determined for Hamoud (2012) and Touhidi (1998) equations are presented in Table 3.7. Both Hamoud (2012) and Touhidi (1998) presume that the rate change of permeability as response to volumetric strain remains constant and independent of the applied confining stresses. The latter assumption is revoked by our experimental findings. As can be seen from Figure 3.41, the argument (β) depicted an obvious increase with the increase of effective confining stress.

Table 3.7 Parameters of Hamoud (2012) and Touhidi (1998) equations

$\boldsymbol{\beta}$		
Hamoud (2012) Equation Constants		Touhidi (1998) Equation Constants
a	b	B
2.8	1.9	2.5

A regression analysis conducted on the experimental data resulted in the following power equation as an appropriate candidate to represent the relationship between (β) and the applied confining pressure (Equation 3.23):

$$\beta = \left(\frac{C}{\emptyset_i}\right) {\sigma_3'}^{a}, \quad \text{(3. 23)}$$

where the fitting parameters (a) and (c) are to be determined from the experimental data. A simple substituting of (β) and (α) by their corresponding expressions into the previous exponential model (Equation 3.19) leads to following equation:

$$\left(\frac{k}{k_o}\right) = e^{\left(-a\sigma_3' + \left(\frac{c}{\emptyset_i}\right){\sigma_3'}^{b}\varepsilon_v\right)}, \quad \text{(3. 24)}$$

where the numerical values of constants, (a), (b), and (c) are presented in Table 3.8.

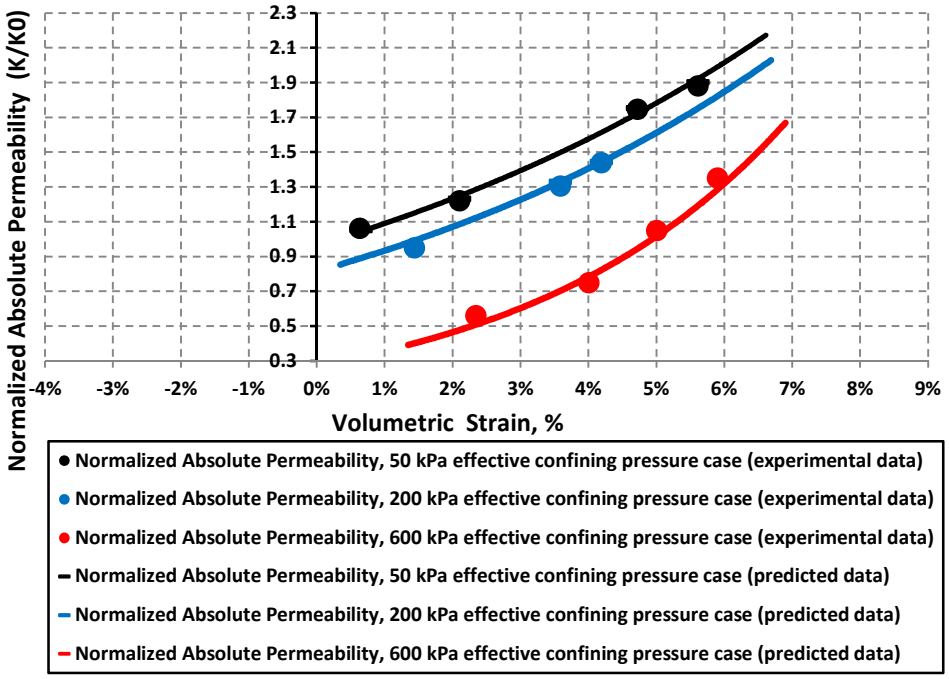

Figure 3.42 Normalized absolute permeability versus volumetric strain for the three effective confining pressures: 50 kPa, 200 kPa, and 600 kPa

It is clear from Figure 3.42 that the prediction model (Equation 3.24) provided a good match with experimental data for the dilation part. However, the consistency of model remains poor within the compaction stage. Expectedly, the exponential model was not capable to cover the compaction portion of the sample deformation, which clearly infers the need of a more complex model that is able to predict the full range of the volumetric strain including the contraction part. It may be possible to achieve this through an advanced mathematical concept such as parametric equations.

Table 3.8 Values of predictive model constants: (a), (b), and (c)

Absolute permeability prediction model (Equation 3.24) constants		
a	b	c
0.0011	1.1181	2.492

3.8.2.3 Summary of Triaxial Compression Tests Results

The developed function (Equation 3.24) provides a consistent method to estimate the permeability evolution of a dense sand specimen during the dilation phase. Based on this model, new values of absolute permeability can be generated from the initial absolute permeability, the measured rate of volumetric strain, the initial porosity, and the magnitude of applied effective confining pressure. Thus, an accurate measurement of volumetric strain, adequate calculation of equation parameters, and closely controlled experimental procedures are keys to assure high quality prediction of the model. Compared to other theoretical studies, the current permeability modeling does contain an obvious dependence on the effective confining stress (σ_3') by explicitly incorporating it as key parameter in the theoretical equation. Another interesting feature of this model is that clearly shows the rate of change in the absolute permeability is inversely proportional to both effective confining pressure and the initial porosity ($\emptyset_i$) of the soil. This inverse relationship between permeability enhancement and the initial porosities of soil was commonly observed by previous experimental researches (Oldakowski 1994 and Touhidi 1998).

Based on the experimental results and discussion reported in previous sections, a graphical presentation of absolute permeability evolution with respect to volumetric strain and effective confining stress is summarized in Figure 3.43.

3.8.2.1 Comparaison with Previous Exprimental Studies

As discussed previously, a good match was obtained between the results of this study and previous research studies. Most of the researchers described the same permeability behavior generated in the present experimental study: initial decline of absolute permeability during the contraction phase followed by an important rise believed to be linked to dilation onset. A strong correlation

between permeability enhancements and effective confining stress level was generally observed in previous studies as well.

Yaich (2008) conducted an experimental examination of the grain morphology effect on absolute permeability behavior of the sand during shearing (triaxial compression tests). For his samples made using the wet vibration technique, the triaxial tests conducted at 345 kPa generated an initial permeability decline of 5% during the contraction phase of the soil followed by a maximum increase of 12% at 10 % axial strain. Khan (2009) experimental investigations also reported comparable results. Khan samples (initial porosity average of 32%) showed a maximum permeability rise of 15% at 10% axial strain following a permeability decrease during the compaction phase of the sample in which permeability recorded a maximum decline of (-25%) below the initial permeability of the sample. By increasing confining stress to 1379 kPa, the absolute permeability gain generated in 345 kPa effective confining stress test was completely suppressed and showed a general decrease of (-30%) at the end of test (at 10% axial strain). These results align with the observations from this study regarding the adverse relationship between effective confining stress and absolute permeability gain.

Nevertheless, a higher rate of the absolute permeability change was exhibited by Touhidi (1998) oil sand reconstituted samples. A maximum permeability enhancement of 200% was achieved at 4% volumetric strain for his 240 kPa effective confining stress test. This is much higher than results reported in the current study for the 200 kPa effective confining pressure case, which shows a maximum increase of 40% in absolute permeability at volumetric strain of 4%. It is speculated that this dissimilarity in results is attributed to the difference in testing programs and the intrinsic proprieties of samples used in the two studies. Boundary conditions could be also an important influence on the permeability performance of Touhidi (1998) oil sand. Touhidi (1998) used lubricated platens

instead of conventional porous stones deployed in the current study, which assured a uniform distribution of porosity within his samples during the shearing process. A homogenous distribution of porosity would result in apparent superior permeability gain than would occur if sample were sheared under regular platens and thus deformed in a non-uniform manner. Similar to current study, permeability reduction due to compaction was not taken into account by Touhidi (1998) prediction model. This reported neglect is mainly due to the particular aspect of his experimental results. Actually, most of Touhidi (1998) sample depicted insignificant permeability decrease during the initial stage of shearing (the compaction stage). Therefore, his relationship describing the absolute permeability changes during shearing did not cover the permeability reduction associated to sample compaction observed at the beginning of loading course. Touhidi (1998) argued that the absence of permeability reduction in the beginning of loading was mainly attributed to the important dilation rate exhibited in his sample at the point when the initial volume reduction was almost instantaneously compensated by the rapid development and expansion of flow channel within his specimens.

For the purpose of validating the prediction model described in Equation 3.24, a graphical presentation of Yaich (2008) and Khan (2009) experimental findings along with predicted values of the absolute permeabilities is shown in Figure 3.44. Values of empirical constants, a, b and c, were carefully calibrated to account for the difference in initial porosity and experimental conditions between the three studies.

Reassuringly, Figure 3.44 provides a good fit between measured and calculated data. All the estimated values fell within ± 2 % of the measured data reported by Yaich (2008) and Khan (2009) for their 345 kPa effective confining pressure cases. However, it is important to note that a good accuracy of the simulation model described in Equation 3.24 is restricted to soils sharing same morphologic

and petrophysical properties of the sand. Based on the analyses conducted in this study, it is also recommended that Equation 3.24 not be used to estimate permeability of dense sand specimens sheared under effective confining pressure higher than 1 MPa.

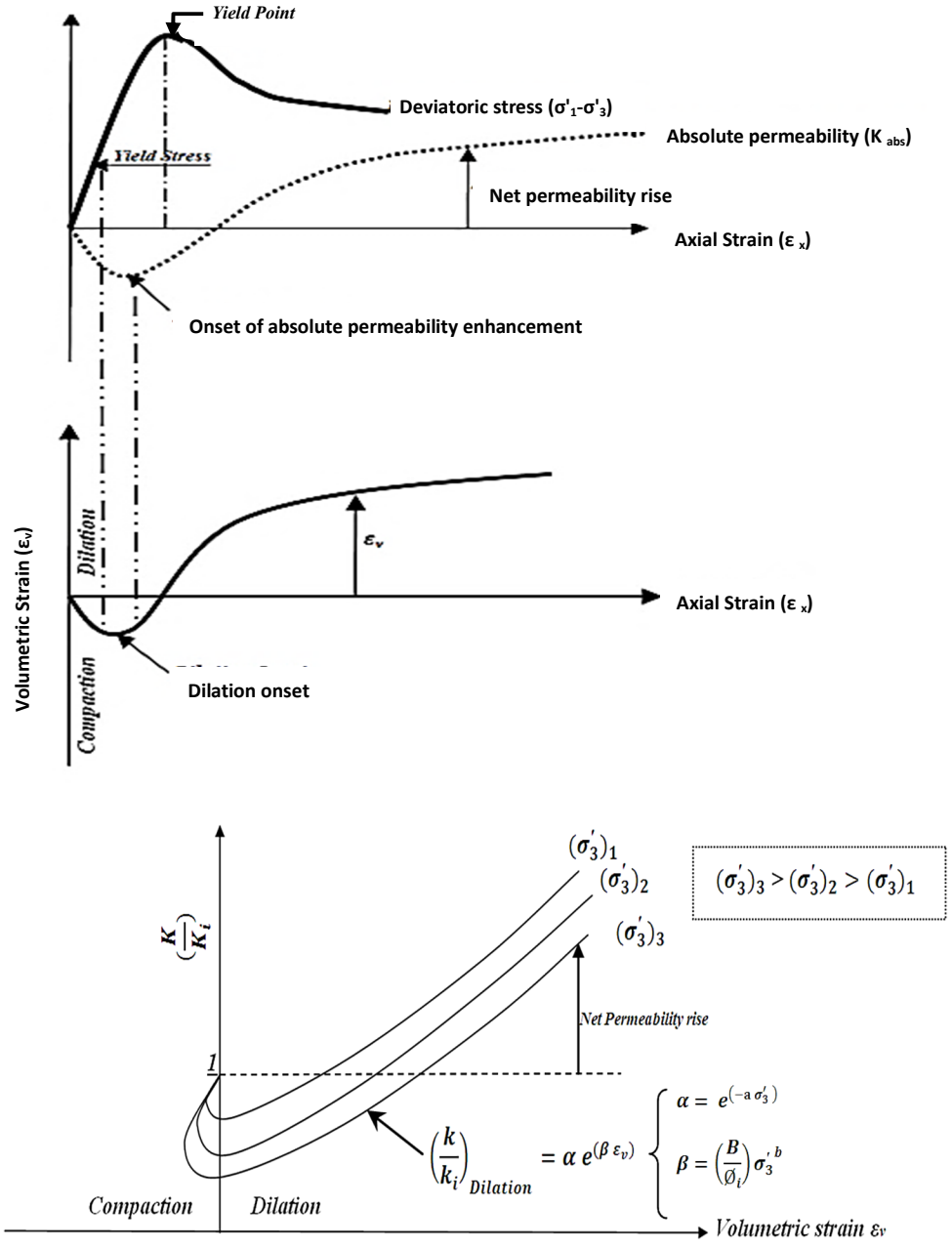

Figure 3.43 Graphical presentation of absolute permeability evolution with respect to volumetric strain and effective confining stress

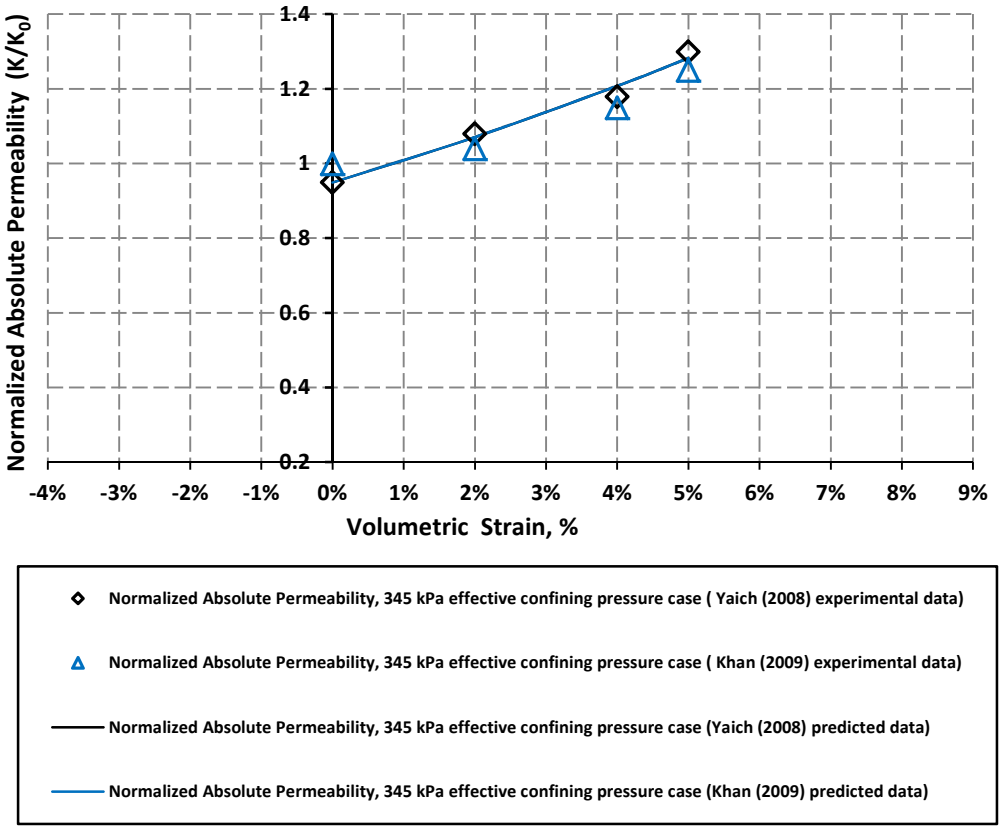

Figure 3.44 Graphical presentation of Yaich (2008) and Khan (2009) experimental findings along with predicted values of the absolute permeabilities determined using Equation 3.24 (Model validation)

4 Chapter 4 Conclusions and Recommendations

The following are conclusions drawn from this research and recommendations for future research regarding the stated objective of the thesis.

4.1 Conclusions

- The shearing experiments show a proportional relationship between the level of effective confining pressure and the shear strength of the sand. In general, samples depicted a higher shear resistance (i.e. higher modulus of elasticity and higher deviatoric stress upon failure) when being confined under high level of effective confining pressure;
- The results generated in this work support the belief that rock properties such as porosity and permeability change significantly in unconsolidated and shallow reservoirs during stress change;
- For both stress paths suggested in the current study, i.e. isotropic unloading and increasing mean stress, permeability-porosity exhibits a good correlation;
- Permeability measurement results show an important sensitivity of absolute permeability to the stress path followed during the experiment. In general, a higher permeability gain was recorded for the triaxial compression tests in comparison to the isotropic unloading experiment (only 8% of permeability enhancement was observed at the end of the isotropic unloading test). This higher enhancement in absolute permeability is attributed to the higher volume gain achieved during the triaxial compression test. Such increase in volume is mainly resulted from the development of shear bands within the sample during process of shearing. Shear bands provide high porosity channels that improve water flow and lead to permeability enhancement;

- In the triaxial compression tests, the absolute permeability depicted same behavior for the three level of effective confining pressure (50 kPa, 200 kPa, and 600 kPa): an initial decease associated to the compaction phase followed by a substantial rise linked to dilation onset of the sample;
- All samples show some permeability increase varying from 20% to 60% depending on the effective confining pressure applied during the triaxial compression experiment. Typically, the permeability variations of the sample depict a strong correlation with volumetric strain: the higher the dilation achieved, the higher the permeability enhancement is observed;
- It is important to note that the absolute permeability of sand increased considerably during the dilative shear especially for low effective confining pressure cases (50 kPa and 200 kPa). For instance, for a dilative volumetric strain of 4%, a total gain of 60% in absolute permeability was observed for the 50 kPa effective confining pressure test. This permeability gain could impart a substantial improvement in the SAGD in situ recovery of the oil and thus it must be taken into account for the oil sand reservoir simulation;
- Although the number of measurements included in this study is limited to allow for an accurate quantitative assessment of permeability behavior, the experimental results show a consistent relationship between the effective confining stress and permeability behavior. The general tendency of permeability enhancement is to decline with the increase of confining stress. In field perspective, higher effective confining stress is an indicative of higher overburden pressure. This implies that at certain reservoir depth the thermal expansion of soil will not induce the desired permeability rise. Thus, a

wise selection of SAGD wells location is important to the optimize production efficiency of SAGD; and

- Most empirical correlations provided in literatures (Kozeny-Carman (1937), Oldakowski (1994), and Touhidi (1998)) overestimated the absolute permeability gain during shearing. This is more likely due to the important concomitant limitations of these prediction models. Actually, previous empirical correlations presume that permeability behavior of the soil is only a function of change in soil porosity and thus it is independent of the stress path followed and the effective confining stress applied. Latest assumption was revoked by the current study findings. Therefore a more accurate correlation that incorporates the effective confining pressure as main argument was developed for dilation part of the volumetric strain curve (Equation 3.24).

4.2 Recommendations

- It is well recognized that porosity variation affects permeability strongly. Nevertheless, the accurate nature of this effect remains unclear primarily because of the associated concerns related to strong potential for fines migration during the permeability data acquisition. To circumvent the false permeability reduction caused by fines migration, recent studies suggest conducting permeability tests with oil instead of water. Such techniques have been found to significantly reduce fine migration and thus yielding a more accurate measurement of absolute permeability;
- Testing results suggest that factors other than pore-volume variation, which was studied extensively in the current study, would also cause a variation of absolute permeability during shearing. Thus, the examination of other plastic mechanisms such as shear bands details

(spatial configuration) is essential to properly evaluate permeability behavior of the soil. Such investigations could be achieved through advanced computerized imaging techniques such as CT-scan and X-ray;

- Inappropriate boundary conditions result in an underestimation of the permeability enhancement during shearing test. The use of lubricated platens instead of regular ones is advised for future experimental works;
- A more sophisticated prediction model that covers permeability variation during both parts of volumetric strain curve (dilation and contraction phases) is required. Such objective can be achieved through an advanced mathematical concept such parametric equations;
- During the current study, the thermal recovery impact on the unconsolidated sand was examined. In the future, these experimental studies should be to cover other kind of reservoir materials (e.g. poorly cemented sands);
- For future studies absolute permeability tests should be conducted at true reservoir pore pressure and on real oil sands cores;
- The validity of this study results should be investigated in full field model reservoir simulation; and
- This study only investigated the absolute permeability changes during SAGD process. However, from a reservoir engineering perspective, looking at relative permeability is more valuable for reservoir simulation. An extensive investigation of relative permeability variation during shearing is strongly recommended for future works.

5 Chapter 5 References

Agar J.R., 1984. Geotechnical Behavior of Sands at Elevated Temperatures and Pressure. Ph.D. Dissertation, Department of Civil Engineering, University of Alberta, Edmonton, Alberta, 906 p.

Ahmed T., 2000. Reservoir Engineering Handbook, United States: Gulf Professional Publishing, 1472 p.

Albahlani A.M., and T. Babadagli, 2008. A Critical Review of the Status of SAGD: Where Are We and What Is Next?; Paper SPE 113283 presented at the SPE West, Reg. AAPG Pacific Section Join Meeting, Bakersfield, California, USA, 31 March-2 April, 22 p.

Blanton T.L. and J.E. Olson, 1999. Stress Magnitudes from Logs: Effects of Tectonics Strains and Temperatures. Journal of the Society of Petroleum Engineering (SPE): Reservoir Evaluation and Engineering (2), pp. 62-68.

Butler R. M., 1991. Thermal Recovery of Oil and Bitumen, Prentice Hall Edition, 1991, p. 285.

Chalaturnyk R. J. and J.D. Scott, 1995. Geomechanics Issues of Steam Assisted Gravity Drainage. Paper SPE. 30280 presented at the SPE International Heavy Oil Symposium, Calgary, Alberta, 19-21 June, pp. 319-333.

Chalaturnyk R. j., 1996. Geomechanics of the Steam Assisted Gravity Drainage Process in Heavy Oil Reservoirs. Ph.D. Dissertation, University of Alberta, Edmonton, Alberta, 576 p.

Collins P.M., M.R. Carlson and A. Settari, 2002. Geomechanical and Thermal Reservoir Simulation Demonstrates SAGD Enhancements Due to Shear Dilation. Paper SPE/ISRM 78237, presented at the SPE/ISRM Rock Mechanics Conference, Irving, Texas, 20-23 October, 7 p.

David A. Redford, Winter 2011. Lectures notes of "Albertan Oil Sands" course, University of Alberta, Edmonton, Alberta.

Desrues J. and G. Viggiani, 2004. Strain Localization in Sand: an Overview of The Experimental Results Obtained in Grenoble Using Stereo-photogrammetry. Int. J. Numerical Analysis Method Geomechanics (28), pp. 279–321.

Dusseault M.B. and N.R. Morgenstem, 1979. Locked Sands; Quarterly Journal of Engineering Geology and Hydrogeology, pp. 216-218.

Dusseault M.B., 1977. The Geotechnical Characteristics of the Athabasca Oil Sands. Ph.D. Dissertation, University of Alberta, Edmonton, Alberta, 472 p.

Federal Highway Administration, 2007. Test Method for Resilient Modulus of Unbound Granular Base/Subbase Materials and Subgrade Soils (UG07, SS07), Protocol P 46, Publication Number: FHWA-HRT-07-052. Retrieved on August 14, 2013 from http://www.fhwa.dot.gov/publications/research/infrastructure/pavements/ltpp/07052/pro46/004.cfm.

Ferfera F.M.R., J.P. Sarda, M. Boutéca, O. Vinckeé, 1997. International Journal of Rock Mechanics and Mining Sciences and Geomechanics Abstracts, Vol. 34, issue 3-4 April, p. 413.

Geotechnical Group, Department of Civil and Environmental Engineering, University of Alberta, 2001. Manual of Artificial Oil Sand Sample Preparation, 48 p.

Government of Alberta, March 2008. Alberta's Oil Sands: Opportunity, Balance, 20 p. ISBN 978-0-7785-7348-7, retrieved on August 13, 2013 from http://www.environment.alberta.ca/documents/Oil_Sands_Opportunity_balance.pdf.

Hassanizadeh S. M. and W. Gray, 1987. High Velocity Flow in Porous Media, Transport Porous Media 2, pp. 521–531.

Khan H.A., 2009. Shear Induced Relative Permeability Change in Uncemented Sands. MSc. Thesis, University of Texas at Austin, USA, 121 p.

Krishna R., 2002. Engineering Properties of Soils Based on Laboratory Testing Manual: Relative Density Determination, University of Illinois at Chicago, 178 p.

Kumar J. and B.N. Madhusudhan, 2010. Effect of Relative Density and Confining Pressure on Poisson Ratio from Bender and Extender Elements Tests Geotechnique, UK, 60(7), pp. 561-567.

Li L. and R.M. Holt, 2002. Particle Scale Reservoir Mechanisms. Oil and Gas Science Technology-Rev. IFP, Vol. 57 (2002), No. 5, pp. 525-538.

Mathieu R., S. Laurent and M. Mitskopoulos, 2011. All-metal Pump Weathers Thermal, Chemical Oil Sands Operations, pp. 155-156. Retrieved on August 14, 2013 from http://www.worldoil.com/April-2011-Technology-from-Europe-All-metal-pump-weathers-thermal-chemical-oil-sands-operations.html

MEG Energy Corp., 2010. "Christina Lake Regional Project Performance Presentation", issued by MEG Energy Corp, June 2010, 90 p.

Mohamed Hamoud, 2012. Influence of Geomechanical Processes on Relative Permeability. MSc. Thesis, University of Alberta, Edmonton, Alberta, 116 p.

Net Resources International, SPG Media Limited, Canada, 2012. Retrieved on April 01, 2013 from http://www.mining-technology.com /projects /athabasca sands/).

Oldakowski K., 1994. Stress Induced Permeability Changes of Athabasca Oil Sands. MSc. Thesis, University of Alberta, Edmonton, Alberta, 246 p.

Ostermeier R.M., 2001. Compaction Effects on Porosity and Permeability: Deep-water Gulf of Mexico Turbidites, Journal of Petroleum Technology, Volume 53, Number 2, pp. 68-74.

Qing Chen, 2009. Assessing and Improving Steam-Assisted Gravity Drainage: Reservoir Heterogeneities, Hydraulic Fractures, and Mobility Control

Foams. Ph.D. Thesis, Department of Energy Resources Engineering, Stanford University, 217 p.

Rajani B.B., 1988. A simple Model for Describing Variation of Permeability with Porosity for Unconsolidated Sands. In-Situ, Vol. 12, No. 3, pp. 209-226.

Richard F.M. and D.W. Wallace, 1990. Definition and World Resources of Natural Bitumen; published in 1990 as U.S. Geological Survey Bulletin No. 1944, 14 p.

Robert P. C. and M. Aubertin, 2003. Predicting the Coefficient of Permeability of Soils Using the Kozeny-Carman Equations. Report EPM–RT–2003-03, January 2003, 35 p. Retrieved on May 05, 2012 from http://www.polymtl.ca/ biblio/epmrt/rapports/rt2003-03.pdf

Schutjens P.M.T.M., T.H. Hanssen, M.H.H. Hettema, J. Merour, P. de Bree, J.W.A. Coremans and G. Helliesen, June 2004. Compaction-Induced Porosity/Permeability Reduction in Sandstone Reservoirs: Data and Model for Elasticity-Dominated Deformation, Journal of the Society of Petroleum Engineering (SPE): Reservoir Evaluation and Engineering, Volume 7, Number 3, pp. 202-216.

Scott J.D., D. Adhikary and S.A. Proskin, 1994. Volume and Permeability Changes Associated with Steam Stimulation in Oil Sands Reservoirs. Paper No. CIM and AOSTRA 91-63; presented at the Petroleum Society of CIM and AOSTRA Technical Conference, Banff, Alberta, April 21-24, 14 p.

Terzaghi K., 1943. Theoretical Soil Mechanics; John Wiley and Sons Inc., New York Edition, 510 p.

The Canadian Association of Petroleum Producers (CAPP), 2012. "Long-Term Outlook for Canadian Crude Oil Production Report", published by The Canadian Association of Petroleum Producers, June 2012. Retrieved on April 01, 2013 from http://www.capp.ca/getdoc.aspx?DocId =209546&DT=NTV.

Touhidi B. A., 1998. Absolute permeability of McMurray Formation Oil Sands at Low Confining Stresses. Ph.D. Thesis, university of Alberta, Edmonton, Alberta, 318 p.

United States Geological Survey, 2012. Earthquake Glossary-Subduction. Retrieved on August 14, 2013 from http://earthquake.usgs.gov/learn/glossary/?term=subduction%20zone

Wadell H., 1935. Volume, Shape and Roundness of Quartz Particles, Journal of Geology 43 (3), pp. 250–280.

Wong R.C.K, 2004. Effect of Sample Disturbance Induced by Gas Exsolution on Geotechnical and Hydraulic Properties Measurements in Oil Sands. Paper 2004-071 presented at the Canadian Intl. Petroleum Conference, Calgary, 8-10 June, 13 p.

Yaich E., 2008. The effect of Stress Paths and Shear Failure on the Permeability of Unconsolidated Sands. MSc. Thesis, University of Texas at Austin, Texas, 108 p.

APPENDIX A Test Procedures for Specific Gravity Tests

The density ratios ($\rho_s, \rho_b,$ and ρ_s) were determined through the following detailed procedures conducted in accordance with ASTM D-854:

i. Fill a volumetric flask to the 500 ml mark with de-ionized water.
ii. Using the scale; determine the mass of the flask and water, (W_1).
iii. Insert a thermometer into the flask to determine the temperature of the water, (T_1).
iv. Pour a 100 g of dry sand into a clean volumetric flask and then add distilled water until the flask is approximately two-thirds (2/3) full.
v. Place the flask onto a hot plate and boil sand and water for 15 to 20 minutes while agitating (i.e. it helps removing air).
vi. After boiling is completed, allow flask to cool-down to room ambient temperature (same (T_1) temperature recorded previously for water).
vii. Refill the flask with de-ionized water until the 500 ml mark is reached.
viii. Determine the combined mass of the flask plus soil-water mixture (flask +sand +water), (W_2)
ix. Take a pan and clean it with dry cloth.
x. Take the pan weight measurements.
xi. Pour water and sand mixture.
xii. Pour the soil-water mixture into the pan, rinsing out the flask to ensure all soil particles are properly removed.
xiii. Place the pan in the oven at 120 ^{o}C and leave it to dry for 24 hours.
xiv. Measure the weight of the pan with dry sand. This is will be the mass of dry soil, ($W_{dry\text{-}sand}$).
xv. Calculate the specific gravity of the sand, (G_s) using the following formula:

$$G_s = \frac{W_{dry\ sand}}{(W_1 + W_{dry\ sand}) - W_2}, \quad \text{..... (Appendix A. 1)}$$

where ($W_{drysand}$) is the weight of oven-dry sand:

$W_{drysand}$ = $W_{(pan+drysand)}$ - W_{pan} , $W_1$is the mass of flask and water (flask +water), and (W_2) is the combined mass of the flask plus soil-water mixture (flask+ sand+ water).

APPENDIX B Test Procedures for Grain Size Analysis

Test procedure for Grain Size Analysis:

i. Make sure that all sieves are clean properly.

ii. Take weight measurements of each sieve as well as the bottom pan, ($W_{\text{Sieve. \#}}$).

iii. Assemble sieves in ascending order, starting by sieve number #200 at the bottom and ending by sieve number # 4 at the top (Figure Appendix B. 2a)).

iv. Place the pan below the sieves set.

v. Take 500 g of the sand specimen, ($W_{\text{Sand specimen}}$).

vi. Pour the sand carefully into the top sieve then place the cap over it (Figure Appendix B. 2b)).

vii. Set the timing device at 10 minutes.

viii. Place the sieves set in the shaker and shake it for 10 minutes (Figure Appendix B. 2c)).

ix. Take the sieve set from the shaker and carefully record each sieve's weight. This weight includes the sieve weight and retained sand particles, ($W_{\text{Sieve. \#+retained sand particles}}$).

x. Record the weight of the bottom pan with its retained fine soil (Figure Appendix B. 2d).

xi. Determine the mass of soil retained on each sieve by deducting the empty sieve mass from the combined mass of the sieve and retained soil:

$$W_{retained\ sand\ particles} = W_{Sieve.\#+retained\ sand\ particles} - W_{Sieve.\#}$$

xii. Obtain the percentage retained on each sieve by simply dividing the weight retained on each sieve by the original sand sample: $Percentage - retained(\%) = \frac{W_{retained-sand-particles}}{W_{sand-specimen}}$.

xiii. Calculate the percent passing (%) for each sieve by starting with 100 % and systematically deducting the percentage retained on each sieve as cumulative procedure. For example, we obtain first the percent passing for the sieve No. 4 by deducting the percentage retained on the sieve from the 100%. The percent passing for the successive sieve would be systematically determined by subtracting the percentage retained on it plus the cumulative retained percentage of all previous sieves and so forth. For this instance, the cumulative retained percentage would be the percentage retained by the sieve No. 4.

xiv. Generate the logarithmic plot of the grain size (µm) versus the percent passing (%) (Figure Appendix B. 1).

xv. Determine The shape of the grain size distribution curve by computing coefficient of uniformity (C_u) and coefficient of curvature (C_C), defined as:

$$C_u = \frac{D_{60}}{D_{10}}, \text{ and} \quad \text{(Appendix B. 1)}$$

$$C_c = \frac{D_{30}}{D_{60} D_{10}}, \quad \text{(Appendix B. 2)}$$

where D_{10}, D_{30}, and D_{60} are respectively the grain diameters corresponding to 10%, 30% and 60% percent passing obtained from the semi-logarithmic curve (Figure Appendix B. 1).

A sand is considered as well graded if (C_u) is higher than 6 and (C_c) is ranging between 1 and 3. When (C_u) and (C_c) are below previous range, soil is defined as poorly graded. Poorly graded soils are commonly identified by either a uniformity in the grain size (Uniform soils) or absence of intermediate grain size range (gap-graded soils). Typical grain size distribution curves of well graded (soil A), gap graded (soil B) and uniform (soil C) soils are shown in Figure Appendix B. 1.

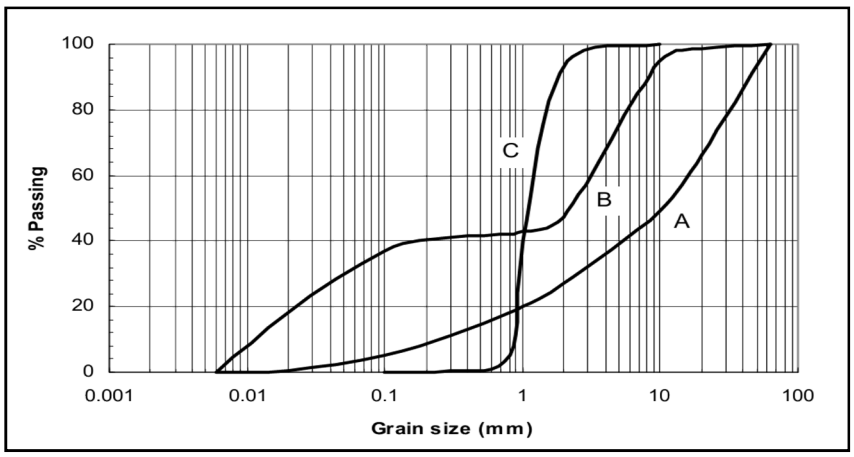

Figure Appendix B. 1 Typical grain size distribution curves resulted from sieve analysis tests (Reddy, 2002)

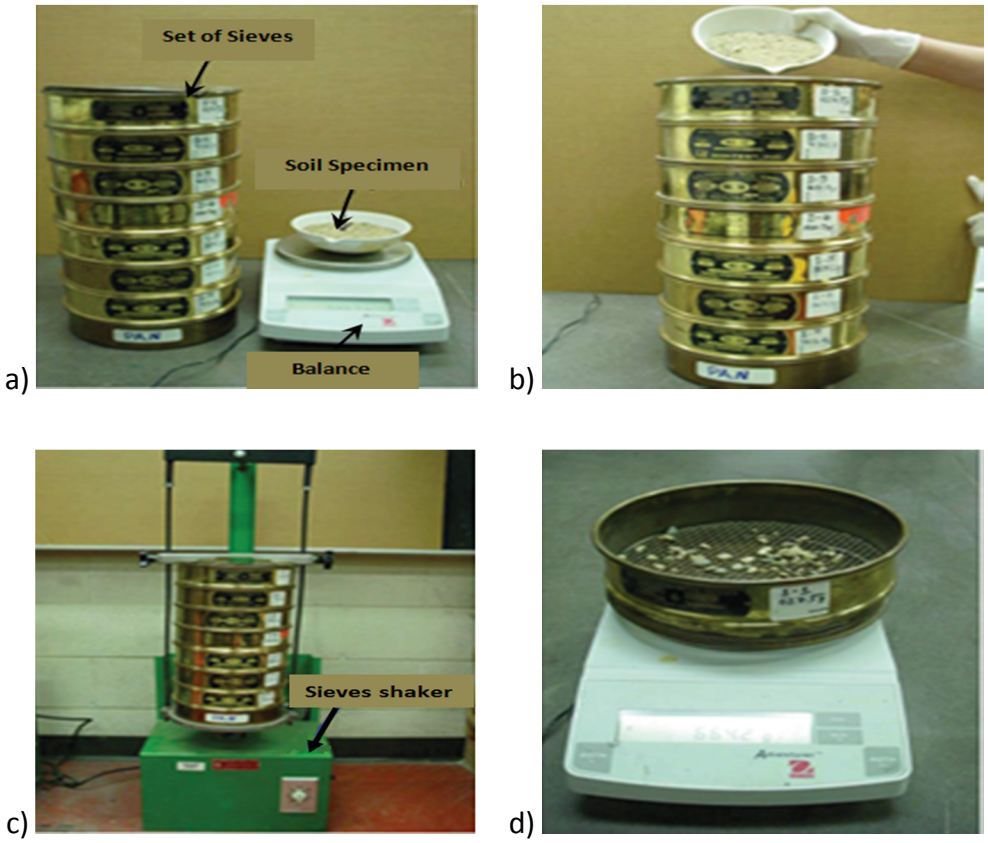

Figure Appendix B. 2 Experimental procedure for sieve analysis test (Reddy, 2002)

APPENDIX C Procedures for Relative Density Test

Figure Appendix C. 1 summarizes the relative density test procedure described below:

i. Pour sand into the mold as loosely as possible by using a funnel and through a spiraling motion. Mold should be filled until approximately 0.5 to 1 inch above the top.
ii. Trim off the sand surface in excess with a straightedge.
iii. Determine the mass of the mold and the sand (M_{s1}), (Figure Appendix C. 1. b)).
iv. Empty the mold.
v. Fill the mold again with different sand, by following the same demarche used in step 1. During filling step, deploy a rubber hummer to level the sand surface so easily placing the surcharge base-plate into vertical position and thus avoiding air surge from the mold during vibration.
vi. Place the surcharge base-plate on the surface of the soil, then twist the surcharge to assure a firm and uniform contact with the surface of the soil.
vii. Remove the surcharge base-plate handle.
viii. Properly attach the mold to the vibrating table.
ix. Determine and record the initial reading by inserting the dial indicator gauge holder in each of the guide brackets while the dial gauge stem in contact with the rim of the mold on the both sides of each guide bracket.
x. Record three reading on each side of the each guide bracket, which is making twelve reading in total, subsequently obtain the initial reading (R_i) by averaging the twelve readings (Figure Appendix C. 1c).
xi. Attach the guide sleeve to the mold and lower the surcharge weight onto the surcharge base-plate (Figure Appendix C. 1d)
xii. Start vibrating the mold assembly and sand specimen for 8 minutes.

xiii. Determine the dial indicator gage reading as in step 9. The average of theses reading will designate the final dial gage reading, (R_f).

xiv. Remove the surcharge base-plate from the mold and detach the mold from the vibrating table.

xv. Empty the mold and record the weight of the mold.

xvi. Measure the dimension of the mold, interior diameter and height, as well record the thickness of the surcharge base-plate, (T_P).

xvii. Calculate the calibrate volume of the mold, V_C.

xviii. Determine the minimum index density (ρ_{min}):

$$\rho_{min} = \frac{M_{s1}}{V_C}, \quad \text{(Appendix C. 1)}$$

where (M_{s1}) is the mass of the loose sand specimen, which equals to mass of the mold with the sand placed loose minus the mass of the mold, and (V_C) is the calibrated volume of the soil.

xix. Calculate the maximum index density(ρ_{min}) as following:

$$\rho_{max} = \frac{M_{s2}}{V}, \quad \text{(Appendix C. 2)}$$

where (M_{s2}) is mass of compacted sand specimen, which equals to mass of mold with sand after vibration minus mass of the mold, and (V) is the volume of the compacted sand, which is computed as $V = V_C - (A_c x H)$. (A_c) is the calibrated cross sectional area of the mold and (H) is obtained from the following equation: $H = (R_f - R_i) + T_p$.

xx. Compute the maximum and minimum index void ratio, (e_{max}) and (e_{min}) , using equations below:

$$e_{min} = \frac{\rho_w G_s}{\rho_{max}} - 1, \text{ and} \quad \text{(Appendix C. 3)}$$

$$e_{max} = \frac{\rho_w G_s}{\rho_{min}} - 1, \quad \text{(Appendix C. 4)}$$

where (G_s) is the specific gravity of the soil and (ρ_w) is water density considered to be 1 g/cm^3.

xxi. Determine the relative density of the sand, (D_r) :

$$D_r = \left(\frac{e_{max}-e}{e_{max}-e_{min}}\right), \quad \text{..... (Appendix C. 5)}$$

where (e) is the void ratio of the samples described by the following equation:

$$e = \frac{\emptyset}{(1-\emptyset)}, \quad \text{..... (Appendix C. 6)}$$

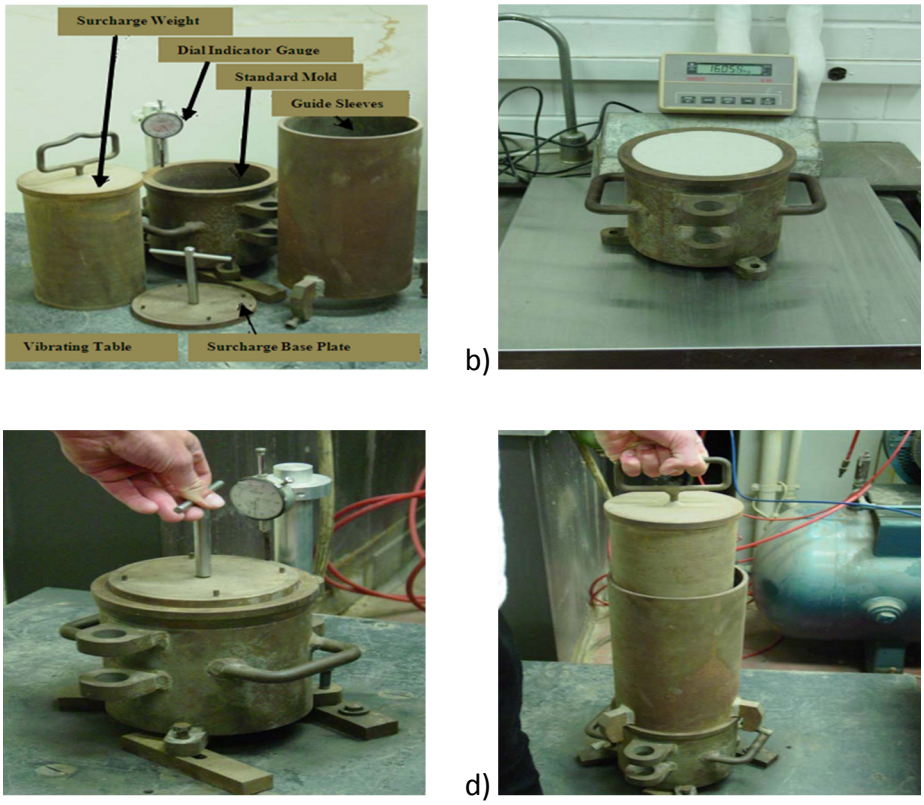

a) b) c) d)

Figure Appendix C. 1 Relative density experimental procedure (Reddy, 2002)